Correlated background and impact on the measurement of theta_13 with the Double Chooz detector

Alberto Remoto

To cite this version:

Alberto Remoto. Correlated background and impact on the measurement of theta_13 with the Double Chooz detector. High Energy Physics - Experiment [hep-ex]. Université de Nantes, 2012. English. NNT : . tel-00821629

HAL Id: tel-00821629
https://theses.hal.science/tel-00821629

Submitted on 11 May 2013

UNIVERSITÉ DE NANTES

FACULTÉ DES SCIENCES ET DES TECHNIQUES

ÉCOLE DOCTORALE 3MPL

Année 2012

Correlated background and impact on the measurement of θ_{13} with the Double Chooz detector

THÈSE DE DOCTORAT

Discipline: Constituants élémentaires et physique théorique
Spécialité: Physique des particules

Présentée
et soutenue publiquement par

ALBERTO REMOTO

Le 5 Octobre 2012, devant le jury ci-dessous

Rapporteurs	Dario AUTIERO	Directeur de Recherche, IPN (Lyon)
	Achim STAHL	Professeur, RWTH (Aachen)
Examinateurs	Thierry GOUSSET	Professeur, Subatech (Nantes)
	Dominique DUCHESNEAU,	Directeur de Recherche, LAPP (Annecy)
	Hervé DE KERRET,	Directeur de Recherche, APC (Paris)
Directeur de thèse	Jacques MARTINO,	Directeur de l'IN2P3, Subatech (Nantes)
Encadrant de thèse	Anatael CABRERA,	Chargé de Recherche, APC (Paris)
Co-encadrant de thèse	Frédéric YERMIA,	Maître de Conférences, Subatech (Nantes)

The chances of finding out what's really
going on in the universe are so remote,
the only thing to do is hang the sense of it
and keep yourself occupied...

The Hitchhiker's Guide to the Galaxy,
Douglas Adams

Abstract

The Double Chooz experiment uses antineutrinos emitted from the Chooz nuclear power plant (France) to measure the oscillation mixing parameter θ_{13}. A rate and shape analysis are performed to search for distortion in the measured energy spectrum due to $\bar{\nu}_e$ disappearance. The best fit value for the neutrino mixing parameter $\sin^2(2\theta_{13})$ is $0.109 \pm 0.030(\text{stat.}) \pm 0.025(\text{syst.})$. The precision and accuracy of the measurement relies on precise knowledge of the rates and spectral shapes of the backgrounds contaminating the $\bar{\nu}_e$ selection over the neutrino oscillation expected region.
This thesis studies the correlated background induced by muons interacting in the detector or in its surroundings. The optimisation of the signal selection allow to reduce the correlated background < 0.2 % by tagging muons crossing the detector with efficiency > 99.999 % and applying a veto time of 1 ms upon a tagged muon. The remaining correlated background, arising from muons which either missed the detector or deposit an energy low enough to escape the muon tagging, has been estimated. For the first time, a pure sample of correlated background is studied in the energy region dominated by $\bar{\nu}_e$, defining dedicated tagging strategies based the direct detection of background events by the outer-most detectors of Double Chooz: the "inner-veto" and the "outer-veto" detectors.
The correlated background measurement presented in this thesis concludes that the spectral shape is consistent with a linear correlated background spectral shape and a total rate of 0.60 ± 0.20 day^{-1}. This represents the official Double Chooz results on correlated background, published in [20].

Résumé

L'expérience Double Chooz détecte les antineutrinos électroniques émis par la centrale nucléaire de Chooz (France) pour mesurer le paramètre de mélange d'oscillation θ_{13}. Une analyse de forme et de taux de comptage est effectuée pour rechercher des distorsions dans le spectre d'énergie mesuré du fait de la disparition d'antineutrinos entre la source (le réacteur) et le détecteur. La meilleure valeur d'ajustement pour le paramètre de mélange $\sin^2(2\theta_{13})$ est 0.109 ± 0.030(stat.)± 0.025(syst.). La précision et l'exactitude de la mesure repose sur une connaissance précise des taux et des formes spectrales des bruit de fond contaminant la sélection d'$\bar{\nu}_e$ dans la région en énergie attendue d'oscillation du neutrino.

Cette thèse traite du bruit de fond corrélé induit par les muons interagissant dans le détecteur ou dans ses environs. L'optimisation de la sélection du signal permet de réduire le bruit de fond corrélé < 0.2 % , d'une part en repérant les muons traversant le détecteur avec une efficacité > 99.999 % et d'autre part en appliquant un temps de latence après une détection muon de 1 ms . Le bruit de fond corrélé restant dans notre échantillon de candidats neutrinos, découlant de muons qui n'ont pas traversé le détecteur ou d'un dépôt d' énergie des muons dans le détecteur en dessous du seuil d'identification, a été estimé. Pour la première fois, un échantillon pur de bruit de fond corrélé est étudié dans la région en énergie dominée par les $\bar{\nu}_e$, en définissant des stratégies de marquage dédiées basées sur la détection directe du bruit de fond par les détecteurs externes de Double Chooz: l' "inner-veto" et l' "outer-veto".

La mesure du bruit de fond corrélé présentée dans cette thèse conclut que la forme spectrale est compatible avec une forme linaire pour le bruit de fond corrélé et un taux de comptage global de 0.60 ± 0.20 day^{-1}. Ce chiffre représente dorénavant le résultat officiel de Double Chooz en matière de bruit de fond corrélée, publié dans [20].

Acknowledgments

Since so many people contributed to this work over the last three years, it is not an easy job to thank them all as they deserve, but it's worth a try.

In a first place I would like to thank my supervisors, Dr. Anatael Cabrera and Dr. Frederic Yermia. This work would have been simply impossible without their guidance. There are no words to express all my gratitude.

Even if, strictly speaking, we have never worked together, I would like to thank Prof. Hervé de Kerret and Prof. Jacques Martino to have supervised my work from the top of their knowledge of high energy experimental physics.

I would also like to thank Prof. Achim Stahl, Prof. Dario Autiero, Prof. Dominique Duchesneau and Prof. Thierry Gousset for the important feedback they provided by reading this manuscript in a critical way and being part to the jury.

I'm grateful to the whole ERDRE group at Subatech (Nantes) and to the whole Neutrino group at APC (Paris) where I had the honor to work with so many pleasant and talented physicists. In particular, I would like to explicitly thank some of them. Dr. Muriel Fallot who at the beginning welcomed me in to the ERDRE group and for the fruitful discussions regarding the simulation of the expected $\bar{\nu}_e$ spectra. Dr. Arnaud Guertin for welcoming me in to his office and for his help with the sometimes excessive laboratory policies. Dr. Amanda Porta, Dr. Luca Scotto Lavina and Dr. Diego Stocco for making me feel like at home in Nantes. Prof. Alessandra Tonazzo for all the help she provided during my stay in Paris and for the email exchange in the spring 2009 from which all this started. Dr. Michel Obolensky for his great experience and knowledge kindly shared with me and all his help in the most difficult times. Dr. Jaime Dawson for the contagious enthusiasms she always puts in to work and for the time she dedicated to review this manuscript. Dr. Didier Kryn and Dr. Davide Franco for the always fruitful discussions and priceless advice about physics, electronics, computing and the nice dinners at their places. To whom I shared the hard life of a Ph.D. student, Tarek Akiri at the beginning, Anthony Onillon, Romain Roncin and Guillaume Pronost at the end.

I wish also to thank all my collaborators who make the Double Chooz experiment a pleasant and challenging working environment, which motivated me to do my best. In particular I'm grateful to Prof. Ines Gil Bottella and the Double Chooz CIEMAT members who welcomed me during many visits to Madrid, to Prof. Masahiro Kuze and the Kuze Lab members for the nice

time I had during my visit at the Tokyo Institute of Technology. Dr. Masaki Ishitsuka and Dr. Camillo Mariani for the discussions, the suggestions an their continuous support to my work.

To the friends with whom I shared the everyday work and sometimes the frustration to be a mere Ph.D. student. Kazu, a good friend 24/7 available to discuss silly topics, solve problems and understand things together. I am going to miss our after work beers, the chitchatting about the collaboration, our common hate of HS and the dream of a better job (now we can change!). Anselm and Sebastian, who always made the time spent in Chooz fun and crazy the after-meeting nights. I will never forget the Delirium Cafe in Brussels. Bernd, to have kindly hosted many times two gipsy students at his place. Pau, who initiated me to the amazing python language, always available to discuss the mystery of our offline code and share his experience, also beyond the work life. I will miss to work with you buddies.

Agli amici che ho avuto la fortuna di incontrare a Parigi... la mia famiglia all'estero. Pietro, che mi ha prestato la sua camera senza neanche conoscermi ed è diventato poi un ottimo amico. Sempre disponibile per una birra, quattro chiacchiere e cose pazze tipo i film di Bud Spencer o la nostra dieta a base di fagioli e cipolle. Martino, il miglior compagno di scalate che avrei potuto incontrare. Importanti le nostre discussioni sulla sfera femminile (TT), il suo buon gusto per il cibo e gli alcolici hanno sempre reso indimenticabili le nostre cene (a seconda della quantità di vino). Franceschina, per le infinite chiacchiere, i calamari ripieni e la nostra prima ed imbarazzante mattina in rue d'Avron. Michela, la più divertente e piacevole persona con cui ho condiviso l'ufficio, sempre in grado di capire cosa c'era di sbagliato, e non solo nel lavoro. Grazi anche ad Aurora, Claudio, Davide Federica, Filippo, Nicolais, Samir e Teresa.

Agli amici di una vita, Cisco, Fra, Giova, Greg, Loris e Marcos. Per farmi sentire,ogni volta che torno a Torino, come se non fossi mai partito. Ora so che sarà sempre così.

Alla mia famiglia, Mamma, Papà, Nonna, Federico, Andrea, Barbara, Beatrice & Leonardo sempre vicini ogni giorno, anche a centinaia di km di distanza.

Ed in fine alla persona più importante di tutte, Stefania, che mi ha accolto in casa sua e poi non siamo più riusciti a fare a meno l'uno dell'altra. Grazie per essere stata e continuare ad essere sempre presente.

Contents

Chapter 1

Introduction

The Standard Model has been widely confirmed by many experiments to be the theory regulating the interactions among subatomic particles. However, some modifications were introduced in order to explain the peculiar behaviour of the neutrino. For this reason, neutrino physics is one of the most important branches of modern particle physics. Among the different interesting aspects regarding the neutrinos, one of the most fascinating phenomena is the so-called neutrino oscillation.

Since the late 1960s several experiments observed discrepancies between the number of neutrinos coming from the Sun and the theoretical prediction. Similar discrepancies were found observing neutrinos produced in the top of the Earth atmosphere. These discrepancies, known as the *solar* and *atmospheric neutrino anomalies* respectively, remained unsolved for about thirty years until being recently understood in terms of the oscillation mechanism.

Neutrino oscillation was postulated by Pontecorvo in 1957 in analogy with the $K^0 \leftrightarrow \overline{K}^0$ oscillations. When the second neutrino family was discovered, Maki, Nakagawa and Sakata proposed in 1962 the possibility of oscillation among the neutrino families, introducing the concept of lepton flavour mixing.

In analogy with the mixing in the quark sector, the lepton flavour mixing implies that the weak eigenstates can be regarded as superpositions of mass eigenstates. The mass eigenstates travel at different speeds in the vacuum, causing different propagation phases and resulting in an oscillation among the flavour eigenstates. Such oscillation requires neutrinos to be massive particles, with a non degenerate mass spectra.

The observation of neutrino oscillation implies a modification in the Standard Model, in order to account for flavour mixing in the lepton sector and massive neutrinos, opening the possibility to explore new physics.

The mixing is mathematically described by the so-called mixing matrix, depending from 3 mixing angles and a complex phase whose values have to be measured experimentally. The solar and atmospheric experiments measured for the first time the mixing angles θ_{12} and θ_{23}, whose values were later confirmed by long baseline reactor and accelerator based experiments. The third mixing angle, θ_{13}, has been recently measured by the new generation of accelerator and reactor experiments. Finally, the CP violating phase δ_{CP} remains still to be measured.

Neutrino physics is widely discussed in Chapter 2 focusing on the neutrino oscillation, both from the theoretical and experimental point of view. Open questions and future efforts to be addressed by the neutrino community are also briefly discussed in the same chapter.

Double Chooz is a new generation reactor experiment designed to measure the third mixing angle θ_{13}. The experiment uses $\bar{\nu}_e$ emitted by the nuclear chain reaction produced in the Chooz nuclear power plant (France). The value of θ_{13} is inferred by a rate and shape analysis to search for a distortion in the measured energy spectrum due to $\bar{\nu}_e$ disappearance.

In order to reduce the systematic uncertainties related to the $\bar{\nu}_e$ detection and to the knowledge of the un-oscillated $\bar{\nu}_e$ spectra produced by the reactor core, two functional identical detectors are employed to perform a relative measurement.

The far detector is installed in the laboratory hall previously used by the CHOOZ experiment, located at a mean distance of 1050 m from the two reactor cores, near the first oscillation minimum due to θ_{13}. The near detector will be placed at a mean distance of 400 m from the reactor cores, where oscillation effects due to θ_{13} are expected to be negligible.

The detector design consists of a 10.3 m^3 of liquid scintillator target, surrounded by passive and active veto volumes. The $\bar{\nu}_e$ are detected through the inverse β-decay reaction in liquid scintillator. The signal consists in a coincidence between a prompt event, produced by the positron with an energy related to the $\bar{\nu}_e$ energy, and a delayed event, produced by the neutron capture. The signal signature is improved by doping the target scintillator with gadolinium since it provides a better energy signature for the delayed event, with the emission of $\sim$ 8 MeV γ rays, and speeds up the neutron capture process with respect to the H of the liquid scintillator. The detector design, has been optimised to reduce the background contamination.

The far detector was build between 2009 and 2010 and began data taking in April 2011. The near laboratory hall construction will finish by the end of 2012 and the near detector is expected to start data taking by the end of 2013. In this first phase with the far detector only, the simulation of the reactor $\bar{\nu}_e$ flux is required to perform the oscillation analysis.

The detailed description of the Double Chooz experiment is presented in Chapter 3, highlighting the major improvements with respect to the previous CHOOZ experiment.

The measurement of θ_{13} has been recently performed by analysing far detector data, taken from 13th April 2011 to 30th March 2012. A rate and shape analysis has been performed by comparing the $\bar{\nu}_e$ energy spectrum measured at the far detector with the expected un-oscillated spectrum from the simulation of the reactor $\bar{\nu}_e$ flux. A shape consistent with θ_{13} related oscillation has been observed. The analysis is described in Chapter 4 highlighting the improvements obtained with respect to the first Double Chooz result.

The precision and accuracy of the measurement relies on precise knowledge of the rates and spectral shapes of the backgrounds contaminating the $\bar{\nu}_e$ selection over the neutrino oscillation expected region. For this reason most of the effort have been focused on the estimation of the background, which is due to three main sources: natural radioactivity, cosmogenic radio isotopes and correlated background.

This thesis studies the correlated background produced by cosmic muons interacting in the detector or in its surrounding, whose prompt and delayed events come from the same physical process. The correlated background contamination is strongly reduced by adding dedicated cuts to the $\bar{\nu}_e$ selection. The remaining background contamination and its spectral shape are estimated by a dedicated analysis developed in Chapter 5. For the first time, a pure sample of correlated background is studied in the energy region dominated by $\bar{\nu}_e$, defining dedicated tagging strategies based on the direct detection of background events by the outer-most detectors of Double Chooz: the "inner-veto" and the "outer-veto" detectors.

The results obtained in this thesis are summarised in Chapter 6 with possible improvements and further development, which could be foreseen for the future.

Finally, Chapter 7 briefly summarises the results and contributions achieved during the development the present thesis.

Chapter 2

Neutrino physics

In this chapter the physics related to the neutrino is widely discussed both from the theoretical and experimental point of view, with a particular focus on neutrino oscillation. The current state of the art regarding the measurement of the oscillation parameters is given with a description of the most important experiments in this field. The problem related to the nature of the neutrino mass is also briefly described. Finally, the open questions and the future efforts to be addressed by the neutrino community are also discussed.

2.1 The standard model of particle physics, an overview

The Standard Model of particle physics ($\mathcal{SM}$) is the theory describing how the fundamental constituents of our universe interact.

From the technical point of view the $\mathcal{SM}$ is a renormalisable gauge field theory, based on the symmetry group $SU(3)_C \otimes SU(2)_L \otimes U(1)_Y$ which describe strong, weak and electromagnetic interaction, via the exchange of spin-1 gauge field: eight massless gluons for the strong interaction, one massless photon for the electromagnetic interaction and three massive bosons, $W^\pm$ and Z^0 for the weak interaction.

The known elementary particles and antiparticles are fermions with spin-1/2 and are organised in two families according on how they interact: quarks and leptons. Quarks interacts with all the three forces, while leptons interact only through the electromagnetic and/or the weak force. Quarks and leptons exist in three generations or flavours, with different masses and flavour quantum numbers, but with identical interactions, which make the $\mathcal{SM}$ symmetric with respect to the flavour. A summary of $\mathcal{SM}$ fermions and bosons is shown Fig. 2.1.

The fermions are a representation of the symmetry group and can be written as:

$$\begin{bmatrix} \nu_l & q_u \\ l^- & q_d \end{bmatrix} = \begin{pmatrix} \nu_l \\ l^- \end{pmatrix}_L , \begin{pmatrix} q_u \\ q_d \end{pmatrix}_L , l_R^- , q_{uR} , q_{dR} \tag{2.1}$$

where the left-handed fields are $SU(2)_L$ doublet, while the right handed fields are $SU(2)_L$ singlets. Neutrinos interact only via the weak force and they are experimentally observed with left-handed helicity, thus a right-handed neutrino is not included in the $\mathcal{SM}$.

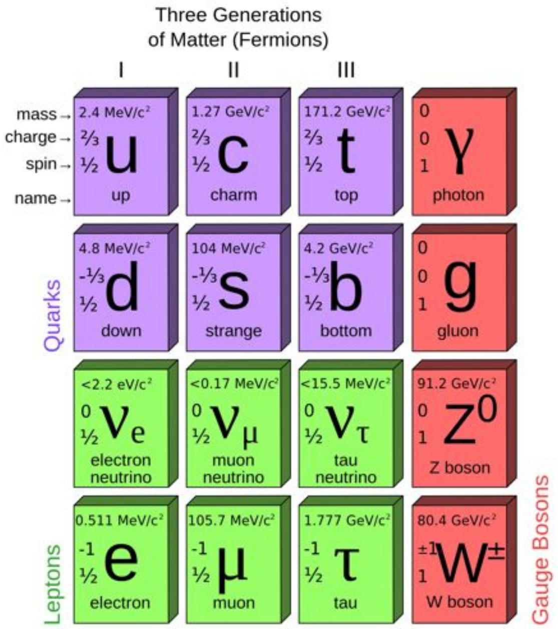

Figure 2.1: The Standard Model of elementary particles (antiparticles are not show for brevity), with the gauge bosons in the rightmost column.

Due to the gauge symmetry of the theory, particles are so far massless. While such assumption appears as a good approximation at high energies (E $\gg$ M$_Z$, M$_W$), where the weak and electromagnetic interactions have similar strengths and are described by the unique electroweak force, at low energies the mass of the W$^\pm$ and Z bosons make the weak interaction weaker than the electromagnetic interaction.

The weak gauge bosons masses are acquired by introducing a new scalar field and breaking the gauge symmetry by choosing an expectation value for its vacuum state. This mechanism, known as spontaneous symmetry breaking, generates the masses for the weak bosons and give rise to the appearance of the spin-0 Higgs boson. The photon and the gluons remain, by construction, massless particles in agreement with experimental observations.

Once the gauge symmetry is broken, also fermions are allowed to acquire a mass term through the so called Higgs mechanism which couples the right-handed singlets with the left-handed doublets via the Yukawa coupling constant, providing masses of the form of:

$$\mathcal{L}_Y = m_l \bar{l}_L l_R + m_q \overline{q}_L q_R + h.c. \tag{2.2}$$

where the mass term for the fermions (as example) is given by m_l:

$$m_l = \frac{v}{\sqrt{2}} \Gamma_l \tag{2.3}$$

where v is the vacuum expectation value of the Higgs field and Γ_i is the Yukawa coupling constant, that assumes different values for the different fermions. To explain the observed masses, Γi varies from ∼1 for the heaviest fermion, the quark top, to $\sim 10^{-5}$ for the lighter charged fermion, the electron.

Since the observed neutrinos are only left-handed, they are not allowed to acquire mass though the Higgs mechanism, remaining massless in the $\mathcal{SM}$.

The $\mathcal{SM}$ provides a beautiful theoretical model which is able to accommodate most of the present knowledge on electroweak and strong interactions. It is able to explain many experimental facts and, in some cases, it has successfully passed very precise tests. Even the long search for the Higgs boson has recently provided conclusive evidence for the discovery of a new particle, consistent with the $\mathcal{SM}$ Higgs boson hypothesis [11].

In spite of the impressive phenomenological success, the $\mathcal{SM}$ leaves many unanswered questions to be considered as a complete description of the fundamental forces. There is no understanding regarding the existence of three (and only three) fermions families as well as their origins. There is no answer to the observed mass spectrum and mixing pattern. These, and others questions remain open and require new physics beyond the $\mathcal{SM}$. As will be stressed in the rest of this chapter, first hint from such new physics has emerged with evidence of neutrino oscillations.

2.2 Neutrino history in brief

The neutrino was postulated by Pauli in 1930 as an effort to explain the continuous electron energy spectrum observed in nuclear β decays [82]. Pauli proposed a new particle, electrically neutral to conserve charge, with spin 1/2 to conserve angular momentum, weakly interacting since it was not detected at that time and with a mass lighter than the electron. Following the discovery of the neutron by Chadwick in 1932 , Fermi explained theoretically the β-decay [58] as the decay of a neutron in proton, electron and a neutrino:

$$n \to p + e^- + \overline{\nu}_e \tag{2.4}$$

The Fermi theory is now understood as low energy limit of a $\mathcal{SM}$ charged current interaction with the exchange of a W boson.
In 1956 Cowan and Reines first detected antineutrino created in a nuclear reactor using the inverse β-decay reaction [87]:

$$p + \overline{\nu}_e \rightarrow n + e^+ \tag{2.5}$$

The detector was made of a tank containing 200 l water with about 40 kg of dissolved cadmium chloride, three layer of plastic scintillator and 110 5" photomultiplier tube. The positron from the inverse β-decay quickly finds an electron and annihilates, rising gamma rays detectable in the scintillator. The neutron is captured by the Cadmium giving further gamma rays with a delay of about 5 μs.
The second neutrino family was discovered in 1962 at Brookhaven National Laboratory [48]. A spark chamber detector was exposed to the first neutrino beam created by the decay of pions. Neutrinos were observed to create muons through charged current interaction in the detector, suggesting such neutrinos were of a different species with respect to the one observed by Cowan and Reines.
When in 1975 the third family charged lepton, the τ, was discovered [83], it was postulated that a third type of neutrino, ν_τ, would have to exist. The tau neutrino was finally directly observed in 2001 by the DONUT experiment at Fermilab [55].
The CERN experiments at LEP during the 1990s studied in detail the property of the $W^{\pm}$ and Z bosons. The number of active neutrinos was precisely constrained to three families by measuring the Z decay width [10], which depends from the number of kinematically accessible decay channels:

$$N_\nu = \frac{\Gamma_{inv}}{\Gamma_\nu^{SM}} = 2.9840 \pm 0.0082 \tag{2.6}$$

where Γ_{inv} is the total Z with minus the measured individual contribution from charged fermions and Γ_ν^{SM} is the theoretical contribution of one neutrino flavour. It should be noted that the LEP measurement constrains only the numbers of active neutrinos, the ones for which the decay $Z \rightarrow \nu_x \overline{\nu}_x$ is kinematically allowed. The existence of a fourth sterile neutrino family with masses bigger than $m_Z/2 \simeq 45.5$ GeV is not excluded.
Within these experimental evidences, neutrinos are coupled with corresponding leptons in a flavour doublet and $\mathcal{SM}$ interactions conserve the lepton flavour quantum number (i.e. charged-current interactions transform the ν_l ($\overline{\nu}_l$) into the corresponding charged lepton l^- (antilepton l^+)).
Nevertheless, since the late 1960s several experiments observed some discrepancies between the number of neutrinos coming from the sun and the theoretical prediction. Such discrepancies known as the *solar neutrino anomalies* remained unsolved for about thirty years until being later understood

in terms of the so called neutrino oscillation mechanism. As explained with more details in the following sections, the oscillation mechanism requires the neutrino to have non-null mass and lepton flavour quantum numbers are no longer conserved.
The $\mathcal{SM}$ is clearly not complete and requires extension to accommodate neutrino oscillation mechanism and its consequences.

2.3 Neutrino oscillation, the theory

Neutrino oscillation were postulated in 1957 by Pontecorvo [86]. In analogy with $K^0 \leftrightarrow \overline{K}^0$ oscillations, Pontecorvo suggested the possibility of neutrino-antineutrino oscillation $\nu \leftrightarrow \overline{\nu}$. When the second neutrino family where discovered, Maki, Nakagawa and Sakata proposed in 1962 the possibility of oscillation among the neutrino families introducing the concept of lepton flavour mixing [101]. The neutrino oscillation mechanism is based on the fact that if neutrino have a non-null mass, flavour states $|\nu_\alpha\rangle$ (interaction states) and mass states $|\nu_i\rangle$ (propagation states) could not coincide, in analogy to the mixing in the quark sector:

$$|\nu_\alpha\rangle = \sum_i U^*_{\alpha,i}|\nu_i\rangle \tag{2.7}$$

where α represent the flavour families (e, μ, τ), $|\nu_i\rangle$ the mass states of mass m_i (with $i = 1, 2, 3$) and U is the so called PMNS[1] unitary mixing matrix. Neutrinos are produced via weak interaction in a defined flavour eigenstate $|\nu_\alpha\rangle$ together with the corresponding lepton α. Assuming the neutrino is produced at time $t = 0$:

$$|\nu(t = 0; L = 0)\rangle = |\nu_\alpha\rangle = \sum_i U^*_{\alpha,i}|\nu_i\rangle \tag{2.8}$$

and propagates as a free particle following the Schrodinger equation, after a time t:

$$|\nu_\alpha(t, L)\rangle = \sum_i U^*_{\alpha,i} e^{-i(E_i t - pL)}|\nu_i\rangle \tag{2.9}$$

assuming the three mass eigenstates propagate with the same momentum with relativistic energies ($p \simeq E \gg m$):

$$E_i = \sqrt{p^2 + m_i^2} \simeq p + \frac{m_i^2}{2p} \simeq E + \frac{m_i^2}{2E} \tag{2.10}$$

Eq. 2.9 could be written, using natural units ($c = \hbar = 1$), as:

$$|\nu_\alpha(t, L)\rangle = \sum_i U^*_{\alpha,i} e^{-i\frac{m_i^2}{2E}L}|\nu_i\rangle \tag{2.11}$$

---

[1] Pontecorvo-Maki-Nakagawa-Sakata matrix

the initial mass state components evolve independently acquiring phases depending from their masses. In an equivalent way, reverting Eq. 2.9 to express the mass eigenstate $|\nu_i\rangle$ as a function of the flavour eigenstate $|\nu_\beta\rangle$:

$$|\nu_\alpha(L)\rangle = \sum_{\beta\in\{e,\mu,\tau\}} \left(\sum_i U^*_{\alpha,i} e^{-i\frac{m_i^2}{2E}L} U_{\beta,i} \right) |\nu_\beta\rangle \tag{2.12}$$

the neutrino created at $t = L = 0$, with α flavour state, evolves as a linear superposition of the existing lepton states. Like the production, the detection of neutrinos occurs via the weak interaction. The probability to observe a neutrino created with flavour α, at $L = 0$, with a different flavour β, after a distance L, is obtained from Eq. 2.11:

$$\begin{aligned} P(\nu_\alpha \to \nu_\beta) &= |\langle\nu_\beta|\nu_\alpha(L)\rangle|^2 = \left| \sum_i U^*_{\alpha,i} U_{\beta,i} e^{-i\frac{m_i}{2E}L} \right|^2 \qquad (2.13) \\ &= \sum_i |U_{\alpha,i} U^*_{\beta,i}|^2 + 2Re\left(\sum_{i>j} U_{\alpha,i} U^*_{\beta,i} U^*_{\alpha,j} U_{\beta,j} e^{-i\frac{\Delta m_{ij}^2}{2E}L} \right) \end{aligned}$$

An oscillation term appears as a function of the distance between the neutrino creation point (source) and the detection point (detector), and the neutrino energy. The oscillation frequency is proportional to the squared difference between the mass states $\Delta m_{ij}^2 = m_j^2 - m_i^2$ while the oscillation amplitude is proportional to the PMNS matrix elements $U_{\alpha,i}$.

The PMNS mixing matrix have a complicated form:

$$U = \begin{pmatrix} c_{12}c_{13} & s_{12}c_{13} & s_{13}e^{-i\delta} \\ -s_{12}c_{23} - c_{12}s_{23}s_{13}e^{i\delta} & c_{12}c_{23} - s_{12}s_{23}s_{13}e^{i\delta} & s_{23}c_{13} \\ s_{12}c_{23} - c_{12}c_{23}s_{13}e^{i\delta} & -c_{12}s_{23} - s_{12}c_{23}s_{13}e^{i\delta} & c_{23}c_{13} \end{pmatrix} \tag{2.14}$$

where $c_{ij} = \cos\theta_{ij}$ and $s_{ij} = \sin\theta_{ij}$. The angles θ_{12}, θ_{13}, θ_{23} represent the mixing angles and δ is a CP violation phase. Two additional phases have to be taken into account if neutrinos are Majorana particles but such phases do not impact the neutrino oscillation.

As shown in Eq. 2.13, neutrino oscillation depends also from the mass squared differences between mass states: Δm_{12}^2, Δm_{23}^2 and Δm_{31}^2 which only two of them are independent because related through:

$$\Delta m_{12}^2 + \Delta m_{23}^2 + \Delta m_{31}^2 = 0 \tag{2.15}$$

Consequently neutrino oscillation depends on 6 free parameters: 3 mixing angles, 2 mass squared differences and one complex CP violation phase.

For practical reasons, the mixing matrix is usually factorized in terms of three matrices $M_{2,3} \times M_{1,3} \times M_{1,2}$:

$$U = \begin{pmatrix} 1 & 0 & 0 \\ 0 & c_{23} & s_{23} \\ 0 & -s_{23} & c_{23} \end{pmatrix} \begin{pmatrix} c_{13} & 0 & s_{13}e^{-i\delta} \\ 0 & 1 & 0 \\ s_{13}e^{-i\delta} & 0 & c_{13} \end{pmatrix} \begin{pmatrix} c_{12} & s_{12} & 0 \\ -s_{12} & c_{12} & 0 \\ 0 & 0 & 1 \end{pmatrix} \tag{2.16}$$

$M_{2,3}$ is parametrized in terms of θ_{23} which is the mixing angle dominating the $\nu_\mu \to \nu_\tau$, related to the oscillation of atmospheric neutrino. $M_{1,2}$ is parametrized in terms of θ_{12} dominating the transition $\nu_e \to \nu_{\mu,\tau}$, related to the oscillation of neutrino coming from the sun. Finally, M_{13} depends on θ_{13} which is the mixing matrix dominating the oscillation $\nu_\mu \to \nu_e$. The CP phase always appears multiplied by the terms $\sin\theta_{13}$, so it would be measurable only if θ_{13} is different than zero.
To conclude, the observation of the neutrino oscillations has two main consequences: neutrinos have a non-zero mass and the lepton flavour is not conserved.

2.4 Measuring neutrino oscillation parameters

To easily understand neutrino oscillation experimental results, the simpler case with only two active neutrino is considered. The mixing among two neutrino families can be described by a real and orthogonal 2×2 matrix with one mixing parameter, the rotation angle θ between the flavour and the mass eigenstates:

$$\begin{pmatrix} \nu_\alpha \\ \nu_\beta \end{pmatrix} = \begin{pmatrix} \cos\theta & \sin\theta \\ -\sin\theta & \cos\theta \end{pmatrix} \begin{pmatrix} \nu_1 \\ \nu_2 \end{pmatrix} \tag{2.17}$$

The oscillation probability take the form:

$$P(\nu_\alpha \to \nu_\beta) = \sin^2(2\theta)\sin^2\left(\frac{\Delta m^2 L}{4E}\right) \tag{2.18}$$

the amplitude of the oscillation, $\sin^2 2\theta$, is determined by the mixing angle θ and does not allow to distinguish between θ and $\pi/2 - \theta$, which are not physically equivalent.
Restoring the physics units, the oscillation phase becomes:

$$\phi = 1.27\left(\frac{\Delta m^2(eV^2)L(km)}{E(GeV)}\right) \tag{2.19}$$

In the limit where $\phi \ll 1$, $P(\nu_\alpha \to \nu_\beta) \simeq \sin^2 2\theta(\Delta m^2 L/(4E))^2$, so the measurement of the oscillation probability would determine information only on the product $\sin^2(2\theta) \times \Delta m^2$. The oscillation would not have enough time to develop and the number of neutrino oscillation events measured in the

detector is approximately independent from the distance L (the oscillation goes $\sim (L/E)^2$ and the neutrino flux diminish as $1/L^2$).
In the opposite limit where $\phi \gg 1$ the oscillation are so fast that get averaged out, $P(\nu_\alpha \to \nu_\beta) \simeq 1/2 \sin^2 2\theta$. In this limit the oscillation probability does not depend from the oscillation phase and the number of oscillation events decrease as $1/L^2$.
In order to measure both oscillation parameters, the measurement of the averaged probability is not enough, moreover the L (or E) dependence must also be measured to characterise the oscillation pattern. The best possible experimental condition to characterise oscillation parameters is then to have an oscillation phase of $\simeq 1$.
Even if three neutrino families exist, the mixing parameters are such that the dominant oscillation pattern is driven by the two flavour mixing, while the third flavour contribute at the second or higher order. For this reason the results of oscillation experiments are often shown in a two neutrino scenario and determine a single mixing angle and squared mass difference.

2.4.1 Experimental determination of Δm^2_{12} and θ_{12}

Measurement of Δm^2_{12} and θ_{12} oscillation parameters has been performed by Super-Kamiokande (SK) and SNO using neutrino created in the thermonuclear reaction produced in the sun. The same parameters has also been measured by KamLAND using terrestrial $\bar{\nu}_e$ emitted by nuclear power plant. Results from global analysis is shown in Fig. 2.2 [91].

Solar neutrinos

Solar neutrino are ν_e coming from the process responsible for solar power production: $4p + 2e^- \to {}^4He + 2\nu_e + 26.7$ MeV. The process take place through different reactions and consequently solar neutrino are characterised by different energy spectra as shown in Fig. 2.3 [39]. The typical neutrino flux reaching the earth is of about 10^8 ν/s/m^2.
Several experiments measured the solar neutrino flux, starting with the pioneering Chlorine experiment in the Homestake mine, proposed by Davis [50]. The ν_e flux were measured in a tank of 400 m^3 of C_2Cl4 counting the number of radioactive Ar nuclei produced by the inverse beta decay reaction ${}^{37}Cl + \nu_e \to Ar + e^-$. Only one third of the neutrino flux predicted by the Standard Solar Model were measured. At that time an error on the experimental measurements or in the Standard Solar Model was assumed as possible explanation of the observed deficit. While error in the theoretical model were excluded by a better understanding of the sun, further experimental measurements, performed with different technique by Gallex [61], Sage/GNO [13] and Super Kamiokande [63] confirmed the deficit in the solar neutrino flux.

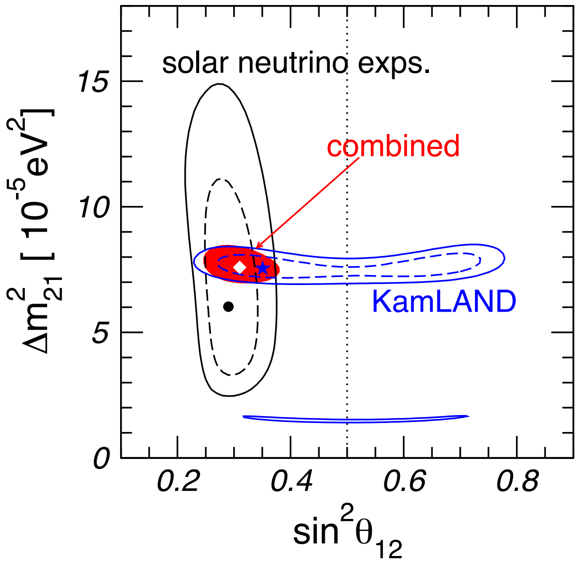

Figure 2.2: Δm^2_{12} and θ_{12} parameters from global analysis of solar and reactor experiments [91].

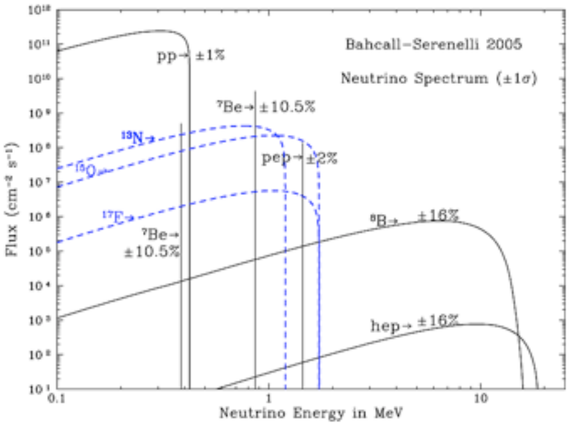

Figure 2.3: Different processes contributing to the solar neutrino spectrum [39].

The so called solar neutrino anomaly was finally solved by the SNO experiment [30] using an heavy water (D^2O) Cherenkov detector, sensible to neutrino interactions through three different processes.
Elastic scattering, $\nu_x + e \rightarrow \nu_x + e$ with $x = e, \mu, \tau$, involve all types of neutrinos but with a different cross-section for ν_μ and ν_τ. Naming Φ_x the neutrino flux for the flavour x, elastic scattering allow to determine the flux $\Phi_e + 0.155(\Phi_\mu + \Phi_\tau)$. The charged current interaction, $D + \nu_e \rightarrow 2p + e$, only involve electron neutrino and therefore determines Φ_e. Finally the neutral current interaction, $D + \nu_e \rightarrow p + n + \nu_e$, involves all neutrino flavour with the same cross-section and allow to determine the total neutrino flux, $\Phi_{tot} = \Phi_e + (\Phi_\mu + \Phi_\tau)$.
The three different reactions measured three independent linear combination of electron, muon and tau neutrino fluxes, as shown in Fig. 2.4. Such measurement allowed to obtain clear evidence of solar neutrino oscillation in term of $\nu_e \rightarrow \nu_{e,\mu,\tau}$, of which ν_e is only one third of the total. Moreover, the total initial ν_e flux has been determined independently from theoretical model.

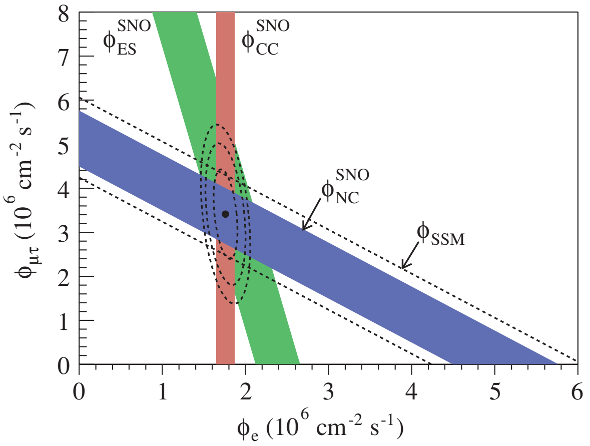

Figure 2.4: Solar neutrino fluxes determined by SNO through elastic scattering (ES) neutral current (NC) and charged current (CC) interactions. The expected flux from the SSM is also shown and it is in agreement with the measured total flux [30].

Long baseline reactor neutrinos

The Kamioka Liquid-scintillator Anti-Neutrino Detector (KamLAND) experiment also played an important role in the determination of the solar oscillation parameters [16].
KamLAND detected $\bar{\nu}_e$ emitted by several nuclear power plant in Japan.

The neutrino energy is of the order of few MeV and the average distance between detector and reactors is of about 200 km. Given the mass squared difference measured by solar experiments of $\sim 7.5\times10^{-5}$ eV^2, the oscillation phase $\Delta m^2_{12}L/(4E)$ is of the order of 1, which provide the best condition for a precise measurement of the oscillation parameters.
The $\bar{\nu}_e$ detection is performed through charged current inverse beta decay reaction $\overline{\nu}_e + p \rightarrow e^+ + n$ in liquid scintillator. The positron and the delayed neutron capture on H gives a clean signature of $\bar{\nu}_e$ interaction. The $\bar{\nu}_e$ energy is directly measured from the positron energy, $E_{\overline{\nu}_e} = E_{e^+} + m_n - m_p$, giving the possibility to measure the neutrino oscillation probability as a function of the energy.
A precise determination of Δm^2_{12} and the shape of the oscillation pattern are obtained as shown in Fig. 2.5.

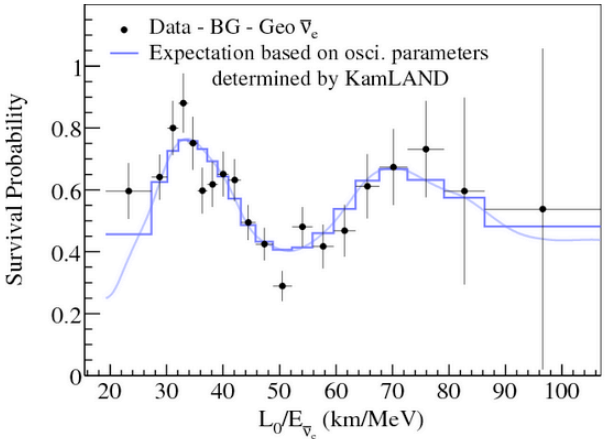

Figure 2.5: Ratio of the background and geo-neutrino subtracted anti-neutrino spectrum to the expectation for no-oscillation as a function of L/E. L is the effective baseline taken as a flux-weighted average (L=180km) [16].

2.4.2 Experimental determination of Δm^2_{23} and θ_{23}

The first measurement of Δm^2_{23} and θ_{23} has been performed by SK using atmospheric neutrinos. Further measurements have been performed to confirm SK results by K2K, MINOS and Opera using ν_μ produced at accelerators. Results from global analysis are shown in Fig. 2.6 [91] and described in more details in the following sections.

Atmospheric neutrinos

Atmospheric neutrinos are produced by cosmic rays interacting in the high atmosphere producing mainly pions and kaons. The charged pions mainly

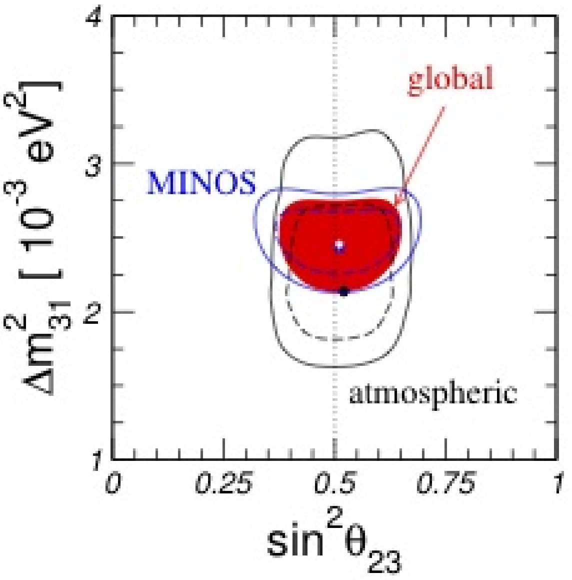

Figure 2.6: Δm^2_{23} and θ_{23} parameters from global analysis of atmospheric and accelerator experiments [91].

decay though weak charged current $\pi^{\pm} \rightarrow \mu^{\pm}\nu_{\mu}(\overline{\nu}_{\mu})$. The muons subsequently decay as $\mu^{\pm} \rightarrow e^{\pm}\nu_{e}(\overline{\nu}_{e}) + \overline{\nu}_{\mu}(\nu_{\mu})$ giving, as a first approximation two muon neutrinos for each electron neutrino.

Atmospheric neutrinos travel a distance between ~ 10 km (if coming from small zenith angles) and $\sim 10^4$ km (if coming from large zenith angles) as schematised in Fig. 2.7. Their energy spans from a few MeV up to several GeV. Since neutrinos can be generated at any point of the atmosphere, neutrinos of the same energy can travel very different distances before reaching the detector, giving different oscillation probabilities. Thus a detector able to distinguish muon neutrinos from electron neutrinos and also able to recognise their incoming direction is necessary.

SK is a large water Cherenkov detector located in the Kamioka mine (Japan) under 2.7 km of rock to shield the detector from cosmic rays. It contains about 50 ktons of water and it is surrounded by about 13000 PMTs. Neutrinos undergo charged current interaction producing charged leptons. The lepton is generally produced with ultra-relativistic energy and it is detected through the cone of Cherenkov light produced as it travels through the detector. The flavour of the lepton is identified by the shape of the Cherenkov ring. The position of the ring allows to determine the lepton directions, which is correlated to the neutrino direction for energies larger than ~ 1 GeV. The lepton energy could also be obtained from the amount

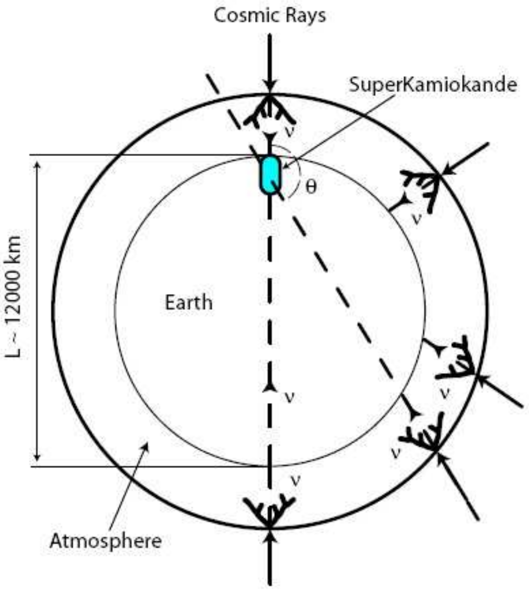

Figure 2.7: Flight distance between the creation point and the SK detector for neutrinos created in atmosphere.

of light collected by the PMTs if the lepton stops into the detector. Even if the lepton energy is not strongly correlated to the neutrino energy it allows to handle the energy dependence of the oscillation probability.

SK provided in 1998 the first firm evidence of neutrino flavour transition comparing the expected number of events with the observed ones, as a function of the zenith angle. SK observed that there are twice as many downward going ν_μ than upward going ν_μ, as shown in Fig. 2.8 [96]. The hypothesis that ν_μ have interacted crossing the earth is not reliable because the earth is nearly transparent for neutrinos with energy of about few GeV and a similar behaviour should have also been found for ν_e. Moreover, since no excess of the electron neutrino flux has been found, the observed oscillation is attributed to the transition $\nu_\mu \to \nu_\tau$.

Accelerator experiments

Experiments using neutrino produced at accelerator have also been performed to confirm the results obtained by SK.

The K2K experiment in Japan used ν_μ produced from a pulsed beam at KEK and the SK detector placed at about 250 km. The average neutrino energy is slightly above 1 GeV. Given the mass squared difference of about 2.5×10^{-3} eV^2 measured with atmospheric neutrino by SK, the oscillation

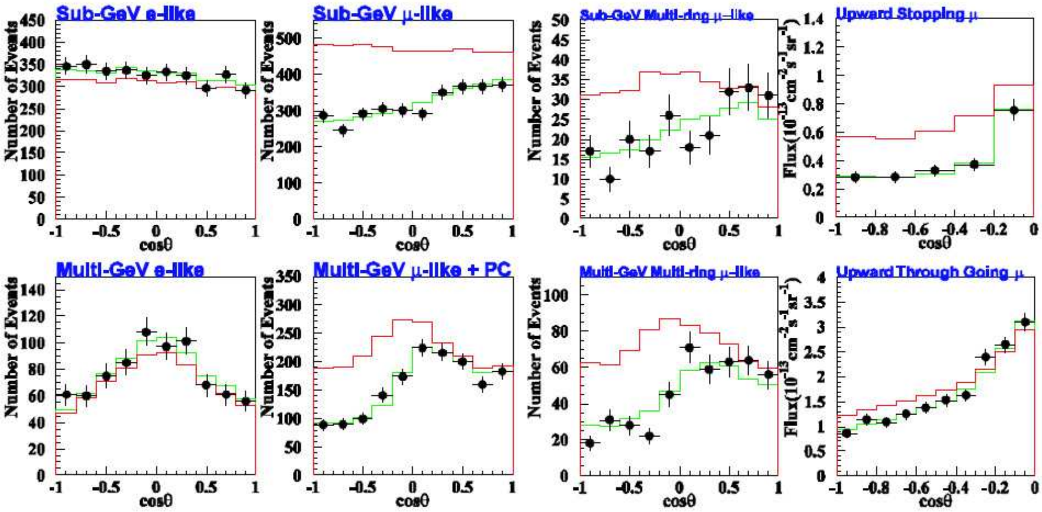

Figure 2.8: The ν_e and ν_μ fluxes are measured as a function of the zenith angle and divided with respect to the lepton energy. Black points represent data, green histogram represent MC expectation with oscillation hypothesis and red histogram represent MC expectation in case of no oscillations [96].

phase is of the order of 1, which represent the best condition to measure oscillation.

The oscillation parameters are measured through ν_μ disappearance, $P(\nu_\mu \to \nu_\mu) = 1 - P(\nu_\mu \to \nu_x)$, comparing the ν_μ flux observed at SK with the unoscillated flux measured by a 1 kton water Cherenkov detector placed at about 300 m from the neutrino source. Results from K2K are reported in [32].

Another important experiment is MINOS, placed in the Sudan mine, at 735 km from a neutrino pulsed beam produced at Fermilab. The neutrino energy is higher than K2K as to obtain an oscillation phase of the order of 1. Like K2K, the initial flux is measured by a near detector and compared with the flux at the far detector to observe ν_μ disappearance. Both near and far detectors are steel-scintillator sampling calorimeters made of alternating planes of magnetised steel and plastic scintillators.

Disappearance measurements of ν_μ determined θ_{23} and Δm^2_{23} in agreement with SK [24]. The beam capability to switch between ν_μ to $\overline{\nu}_\mu$ allows to measure oscillation parameters in case of $\overline{\nu}_\mu$ disappearance [26]. MINOS can also detect ν_e interaction through compact electromagnetic showers and attempt measurement of $\nu_\mu \to \nu_e$ oscillation, thus θ_{13} [23].

The Opera detector, installed at LNGS, instead of measuring oscillation parameters via ν_μ disappearance, is designed to explicit detect ν_τ appearance. Direct observation of ν_τ would confirm the interpretation of SK results in

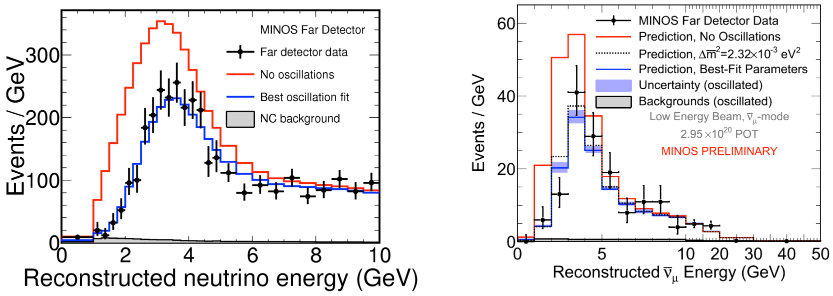

Figure 2.9: Result from MINOS for ν_μ (left) and $\overline{\nu}_\mu$ (right) disappearance. The reconstructed neutrino energy is compared with expected spectrum in the non oscillation hypothesis and the best oscillation fit [24] [26].

term of $\nu_\mu \to \nu_\tau$ oscillation. The ν_μ beam, with a mean energy of about 17 GeV, is produced from a pulsed proton beam at the CERN SPS, about 730 km from Gran Sasso. The τ lepton produced by ν_τ charged current interaction is detected through the topology of its decay in nuclear emulsion films. The expected signal statistics is not very high, 2 ν_τ have been observed (2.1 events expected and 0.2 expected background) since data taking started in 2008 [9].

2.4.3 Experimental determination of θ_{13}

The mixing angle θ_{13} is the smallest angle of the PMNS matrix. For this reason the related oscillations have been the most difficult to observe. Direct and indirect bounds on its value were set in the past by CHOOZ [36], MINOS [23] and from the analysis of sub-leading effects in the solar and atmospheric oscillation, as shown in Fig. 2.10 [91]. However, such bounds were not sensitive enough to exclude a zero value of θ_{13}.

The value of θ_{13} become accessible just recently thanks to the new generation of reactor and accelerator experiments, which provide sensitivities to small mixing angle of about one order of magnitude better than previous limits.

The Tokai to Kamioka experiment (T2K) uses a muon neutrino beam produced at the J-PARC accelerator facility, a segmented near detector with a tracking system to precisely measure the non-oscillated flux and the well known SK detector in order to directly measure the appearance of ν_e. The ν_μ beam is directed 2-3 degree away from the SK baseline of about 295 km. This off-axis configuration lower the neutrino flux but provide a narrow energy spectrum peaked at about 600 MeV.

In summer 2011 T2K reported the observation of six ν_e in the SK detector, with an expected background level of 1.5±0.5 (sys.) events, providing a sig-

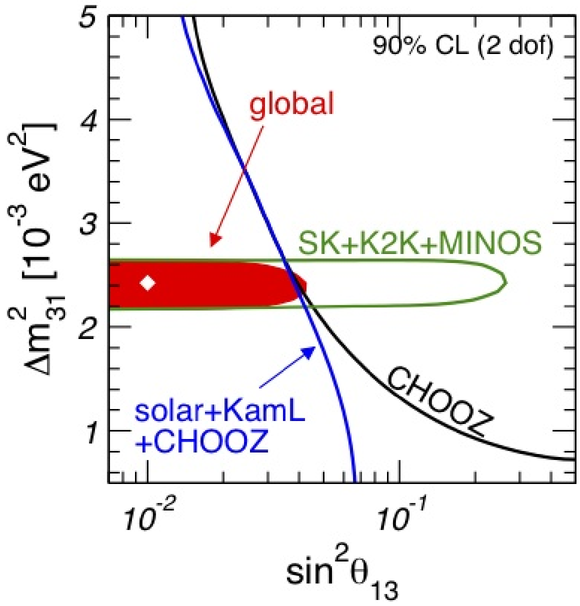

Figure 2.10: Δm^2_{13} and θ_{13} parameters from global analysis of reactor, atmospheric and accelerator experiments [91].

nal significance of about 2.5σ [15]. The T2K results have been updated in 2012 with about 80 % more statistics and improved systematics uncertainty. A total of 10 ν_e events have been observed in the SK detector, with 2.37 expected background events, providing a signal significance of 3.2σ [9].
The new generation reactor experiments, Double Chooz, Daya Bay and RENO aim to measure θ_{13} by looking for distortion in the measured energy spectrum due to $\bar{\nu}_e$ disappearance, in a similar way KamLAND did for solar oscillation. Since the phase for θ_{13} oscillation is proportional to $\Delta m^2_{13} \simeq \Delta m^2_{23}$, about two order of magnitude bigger than the solar mass split, the baseline for θ_{13} measurements has to be of the order of 1 km, two order of magnitude smaller than KamLAND.
The three reactor experiments are similar in concept and design, while differ mainly in the number of detectors and reactors and their relative positions. Daya Bay uses 8 detectors placed at different distances from 6 reactors while RENO uses 2 detectors located near 6 reactors. The Double Chooz experiment, the detector concept and its design are described in full detail in Ch. 3.
The first result from reactor experiment was released by Double Chooz in November 2011 [19] and shortly followed by Daya Bay [33] and RENO [31] in March 2012. In July 2012 Double Chooz released an updated analysis with twice the statistics and major improvements on many aspects of the

analyses [20]. The full and detailed description of the Double Chooz analysis is presented in Ch. 4.

Reactor $\bar{\nu}_e$ experiments are complementary to long baseline accelerator experiments in determining θ_{13}, since they are insensitive to the CP violating phase δ_{CP}, and the dependence from the solar mass split is weak. Furthermore, over short baselines of $\sim$ 1 km the reactor $\bar{\nu}_e$ does not suffer from matter effects. Fig. 2.11 show a summary plot of the recent results from reactor and accelerator experiments.

2.4.4 Neutrino anomalies

So far neutrino oscillation is well established in terms of a three flavour framework. However, there are some experiments whose results are not explained by this framework and might require the introduction of an extra sterile neutrino, i.e. a neutrino not participating in the $\mathcal{SM}$ interactions.

The first evidence of more than three neutrino flavours came from the LSND experiment [27]. Using a $\bar{\nu}_\mu$ from pion decay detected in a liquid scintillator, LSND found $> 3\sigma$ evidence of $\bar{\nu}_\mu \rightarrow \bar{\nu}_e$ transition which would require a mass splitting of about 0.2 eV^2, larger than the atmospheric one.

The LSND anomaly has been tested by MiniBooNE in both neutrino and antineutrino mode. The results obtained in the neutrino mode disfavour most of the parameter space defined by LSND but are not conclusive [28]. The results obtained in the antineutrino mode instead are consistent with LSND signal and consistent with a mass split of between 0.1 eV^2 and 1 eV^2 [29].

Further hints of the existence of sterile neutrinos came from measurements of neutrino fluxes from intense radioactive sources in the GALLEX [60] and SAGE [14] detectors. An unexpected reduction of the ν_e flux consistent with ν_e disappearance has been found at 2.7 σ. The interpretation in term of sterile neutrino oscillation indicates a value for the squared mass difference of about 0.35 eV^2.

Recent re-evaluation of the expected antineutrino flux from nuclear reactor indicate that the measured flux is about 3 % below the prediction with 3σ significance [71]. Even if such a deficit could still be due to some unknown effects in the reactor neutrino production or a non accurate knowledge of the fission product contribution to the antineutrino spectrum, it is consistent with $\bar{\nu}_e$ flux suppression due to sterile neutrino oscillation with mass split of about 2.4 eV^2.

In summary, there are hints compatible with the existence of sterile neutrinos from several experiments, using different sources and detection technique, but none of them could claim a discovery. Many experiments have been proposed for for sterile neutrino search and an exhaustive list could be found in [12].

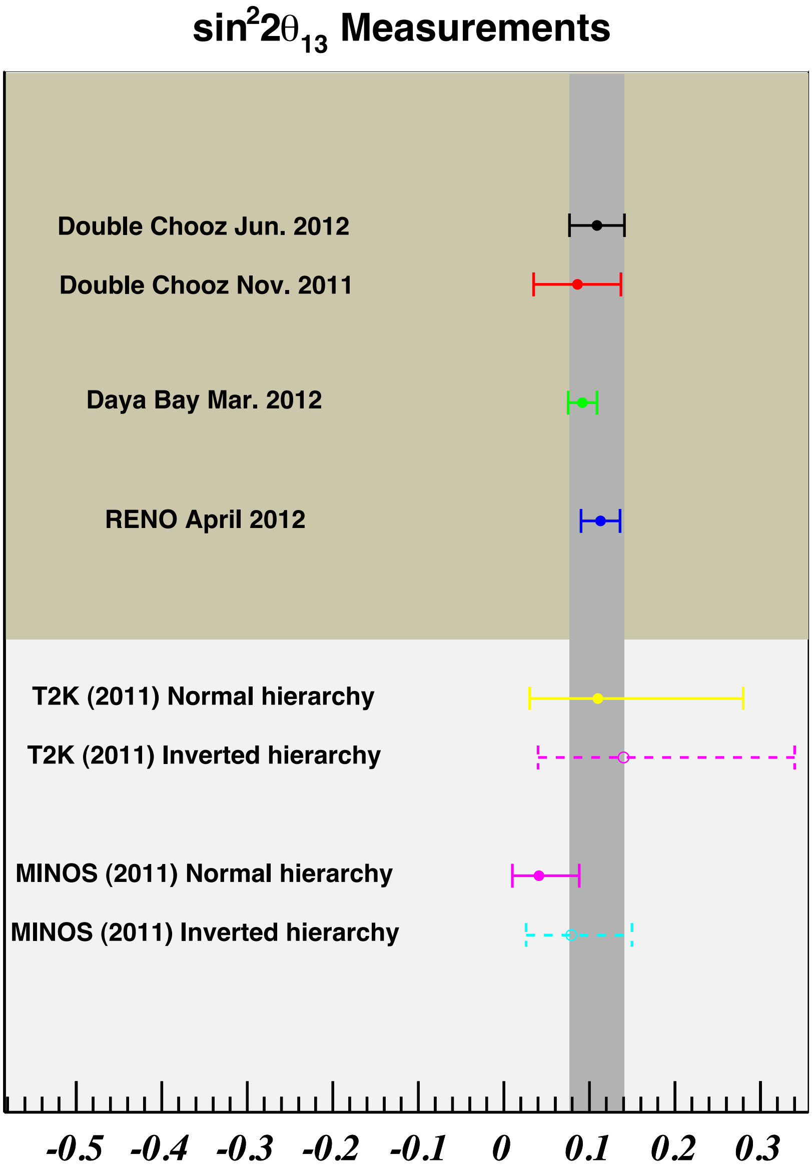

Figure 2.11: Comparison of recent reactor and accelerator-based measurements of $\sin^2(2\theta_{13})$ from Double Chooz [19] [20], Daya Bay [33], RENO [31], T2K [15], and MINOS [23]

2.5 The problem with the neutrino mass

As highlighted in Sec. 2.1, $\mathcal{SM}$ neutrinos are not allowed to acquire masses through the Higgs mechanism because they exist only in the left-handed chiral state (right-handed for anti-neutrinos). However, experimental evidences of neutrino oscillations imply the neutrino must be a massive particles.

Further hints of a non-null neutrino mass also comes independently from neutrino oscillation. In particular, experiments looking for distortion induced by massive neutrinos on the β-decay end point of tritium, $^3H \rightarrow ^3He + e^- + \overline{\nu}_e$, limit ν_e mass below 2 eV [41]. Similarly, the observation of the cosmic microwave background and the density fluctuations, and other cosmological measurements, put a combined upper limit on neutrino mass around 0.5 eV [76], which is six orders of magnitude smaller than the electron mass. Is then necessary to extend the $\mathcal{SM}$ to include neutrino masses. The most natural extension of the $\mathcal{SM}$ add a right-handed neutrino singlet. In this case, neutrino masses are acquired through the Higgs mechanism, like all other fermions:

$$\mathcal{L}_D \simeq -m_D \overline{\nu}_L \nu_R + h.c. \tag{2.20}$$

the mass term is gauge invariant and conserves lepton number. The m_D is the so called Dirac mass term and has the same form of the fermion masses in Eq. 2.3:

$$m_\nu = \frac{v}{\sqrt{2}} \Gamma_\nu \tag{2.21}$$

With this model the Yukawa coupling constant $\Gamma_\nu \simeq m_\nu / v$ needs to be of the order of 10^{-12}, which is far too small compared to the other fermions ($\Gamma_e \sim 0.3 \times 10^{-5}$) and it is commonly considered as unnatural.

Since neutrinos do not have electromagnetic charge, they could be described in term of a Majorana particles:

$$\nu^c = C \overline{\nu}^T \equiv \nu \tag{2.22}$$

where $\nu^c = C\overline{\nu}^T$ is the charge conjugate of the field ν^c, and C is the charge conjugation. Considering a left-handed Majorana particle, $\nu = \nu_L + \nu_L^c$, a Majorana mass term of the form:

$$\mathcal{L}_M \simeq -m_M \overline{\nu^c}_L \nu_L + h.c. \tag{2.23}$$

could be considered. It should be noted that the Majorana mass term involves left-handed neutrino only and is not gauge invariant, $m\overline{\nu^c}\nu \rightarrow m\overline{\nu^c} e^{i2\alpha}\nu$, violating lepton flavour number by two units.

The smallness of the neutrino mass term is no longer dependent on the unnatural Yukawa coupling constant, but nonetheless a mass term for a left-handed neutrino is not allowed by the $\mathcal{SM}$ because it implies an Higgs

triplet with isospin 1.
Once a right-handed neutrino is introduced to obtain a Dirac mass term, a Majorana mass term could also be obtained in case the right-handed neutrino is Majorana particle. The most general mass term can thus be written as mix of Dirac and Majorana term:

$$\begin{aligned}\mathcal{L}_{D+M} &= \mathcal{L}_D + \mathcal{L}_{M_R} + \mathcal{L}_{M_L} \\ &= -m_D\overline{\nu}_L\nu_R - m_{M_R}\overline{\nu^c}_R\nu_R - m_{M_L}\overline{\nu^c}_L\nu_L + h.c \qquad (2.24)\end{aligned}$$

which could be written as:

$$\mathcal{L}_{D+M} = -\frac{1}{2}\begin{pmatrix} \overline{\nu^c}_L & \overline{\nu}_R \end{pmatrix}\begin{pmatrix} m_L & m_D \\ -m_D & m_R \end{pmatrix}\begin{pmatrix} \nu_L \\ \overline{\nu}_R \end{pmatrix} + h.c. \qquad (2.25)$$

The term m_L is the left-handed neutrino Majorana mass, m_R is the right-handed neutrino Majorana mass and m_D is the Dirac mass. The mass matrix can be diagonalised in term of the mass eigenstate:

$$\nu_L = \cos\theta\nu_1 + \sin\theta\nu_2 \qquad (2.26)$$

$$\nu_R^c = -\sin\theta\nu_1 + \cos\theta\nu_2 \qquad (2.27)$$

with eigenstate $m_{1,2}$:

$$m_{1,2} = \frac{1}{2}\left(m_L + m_R \pm \sqrt{(m_L - mR)^2 + m_D^2}\right) \text{ and } \tan 2\theta = \frac{2m_D}{m_R - mL} \qquad (2.28)$$

Since the left handed Majorana mass term requires an Higgs triplet, in the minimal $\mathcal{SM}$ extension, m_L is usually set to zero. The right-handed Majorana neutrino is an electroweak singlet acquiring a mass independently from the Yukawa coupling.
In the limit where $m_L = 0$ and $m_R \gg m_D$:

$$\tan\theta \simeq \frac{2m_D}{m_R} \simeq 0\ ;\ m_1 \simeq \frac{m_D^2}{m_R} \text{ and } m_2 \simeq m_R \qquad (2.29)$$

with one light left-handed neutrino and one heavy right-handed neutrino:

$$\nu_1 \simeq (\nu_L - \nu L^c) \qquad (2.30)$$

$$\nu_2 \simeq (\nu_R + \nu R^c) \qquad (2.31)$$

This is the so called see-saw mechanism, which involves two Majorana particles: a very heavy right-handed neutrino and the observed light left-handed neutrino. The smallness of the observed neutrino mass could then be explained in terms of a Dirac mass of the order of the electroweak energy scale, without the unnatural Yukawa coupling constant, and a much bigger Majorana mass term. The term m_R is generally related to the grand unification

scale around the Planck scale at 10^{16} eV.
The Dirac or Majorana nature of the neutrino is not yet known. Experimentally it is possible to investigate this question through processes violating the lepton number like the neutrino-less double beta decay, which violated the lepton quantum number by two units. Many experiment are currently, or will soon, searching the neutrino-less double beta decay, CUORE [38], GERDA [22], EXO [49] and SUPER-NEMO [85], but not signal has been observed up to now.

2.6 Summary and open questions

Over the last twenty years many experimental efforts have provided clear confirmation that neutrinos are massive particle and that there is mixing between flavour and mass eigenstates. The status of the current knowledge is summarised in term of the mixing parameter and the mass splitting in Fig. 2.12 [41]. In Summary:

- The anomaly between the measured and the expected solar neutrino flux has been solved by SNO [30] and KamLAND [16]. The missing solar neutrino flux is interpreted within the neutrino oscillation scenario in term of ν_e oscillation into a linear superposition of the three neutrino flavour.
  The mixing angle is $\theta_{12} \simeq 32^\circ$ and $\Delta m^2_{12} = (7.50 \pm 0.20) \times 10^{-5}$ eV^2.

- The atmospheric neutrino oscillations has been characterised by SK [96] and long baseline accelerator experiment as K2K [32] and MINOS [24]. The observed disappearance of atmospheric ν_μ has been interpreted in term of oscillations into a linear superposition of, mainly, ν_τ and ν_μ. The most stringent limit on atmospheric neutrino oscillation parameters is provided by MINOS: $\sin^2 2\theta_{23} > 0.90$ (90 % C.L.) and $|\Delta m^2_{23}| = (2.43 \pm 0.13) \times 10^{-3}$ eV^2.

- The latest mixing angle θ_{13} is currently under measurement from accelerator experiment, through $\nu_\mu \to \nu_e$ appearance channel, and reactor experiments, through $\bar{\nu}_e$ disappearance. Measurements with sensitivity $> 3\sigma$ has been recently published and further improvement are expected in the near future.

With the current characterisation of the PMNS matrix, new measurements will be possible in order to improve the current knowledge and to complete neutrino oscillation picture:

- The CP violation phase δ could be measured in long-baseline experiments, studying oscillation probability asymmetries between neutrino and antineutrino: $P(\nu_\mu \to \nu_e) \neq P(\bar{\nu}_\mu \to \bar{\nu}_e)$.

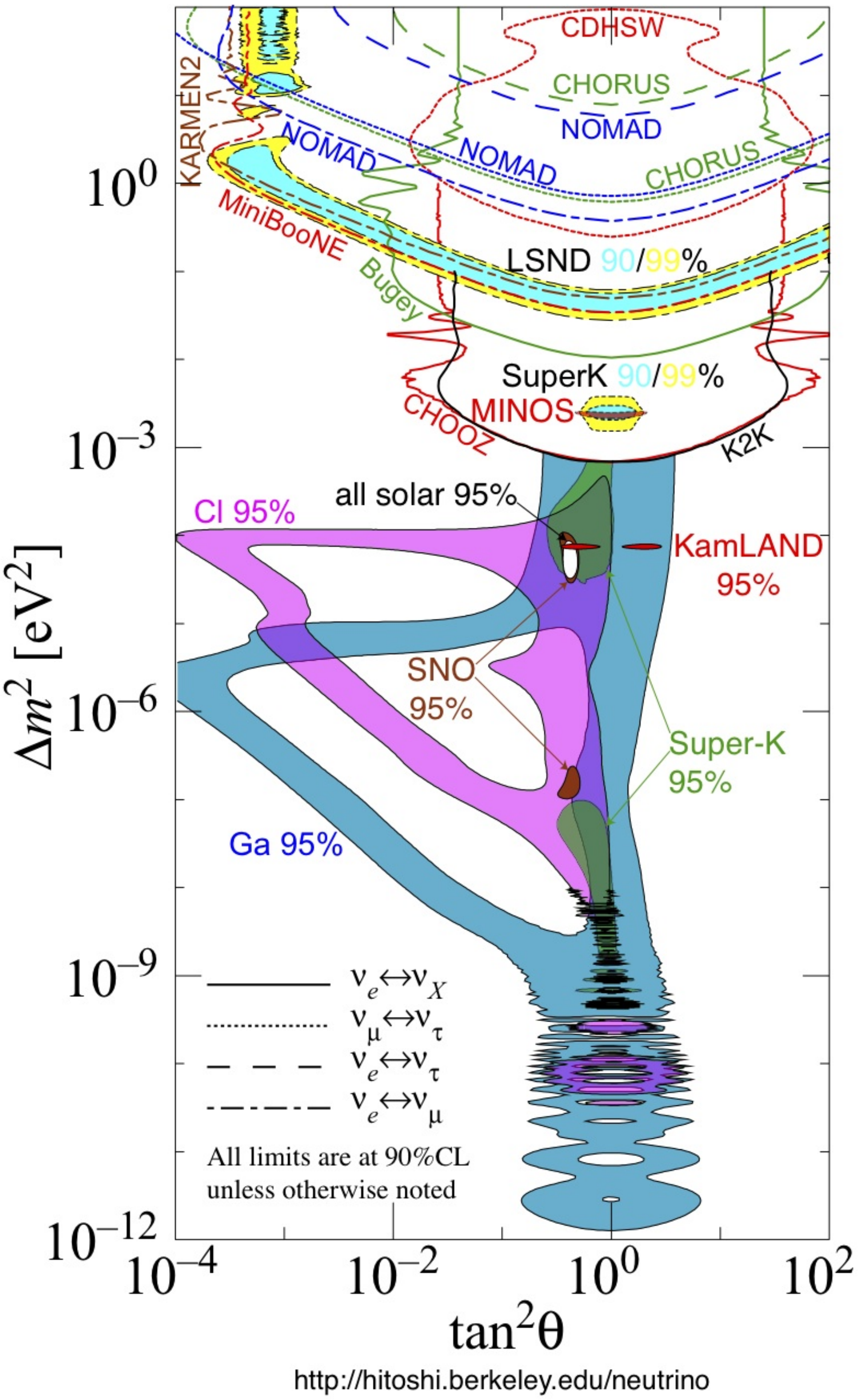

Figure 2.12: Summary of current knowledge on neutrino oscillation in $\Delta m^2 - \tan^2\theta$. PDG 2011 update [41]. Does not contain yet 2012 results on θ_{13}.

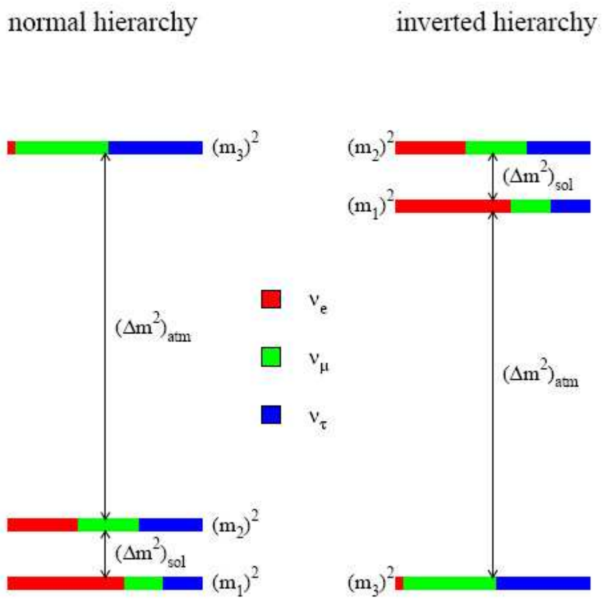

Figure 2.13: The normal and inverted neutrino mass hierarchy. The different colours show the weights of the flavour mixing for a given mass eigenstate.

- The matter effect[2] could be used in long baseline experiment to measure the sign of Δm^2_{23} and establish the neutrino mass hierarchy. As shown in Fig. 2.13, a positive (negative) Δm^2_{23} imply the neutrino separated by the atmospheric mass splitting is heavier (lighter) than the neutrinos separated by the solar mass splitting. In case of normal hierarchy, $\Delta m^2_{23} > 0$, the matter effect would enhance the $\nu_\mu \leftrightarrow \nu_e$ oscillations while suppressing the $\bar{\nu}_\mu \leftrightarrow \bar{\nu}_e$. In case of inverted hierarchy, $\Delta m^2_{23} < 0$, the opposite would happen.

- A combination of reactor $\bar{\nu}_e$ disappearance and both accelerator ν_μ disappearance and ν_e appearance would discriminate the sign of $\theta_{23} - \pi/4$. The degeneracy on the measurement of θ_{23} at accelerator experiment will be broken by the reactor θ_{13} measurement which does not depend on θ_{23}. Such measurement would allow to discriminate the fraction of ν_μ and ν_τ contained by the mass state ν_3.

Beyond neutrino oscillation, is then necessary to measure the absolute mass of the neutrinos, their Dirac or Majorana nature and to confirm or reject the existence of a fourth sterile neutrino.

---

[2] Not discussed in this chapter for brevity, but available e.g. in [97].

Chapter 3

The Double Chooz experiment

A nuclear reactor core is an abundant source of $\bar{\nu}_e$ emitted by the β-decays occurring to the products of the nuclear fission. Since the energy released during the β-decays is smaller than $\sim$ 10 MeV, no μ nor τ are produced, providing a pure flux of $\bar{\nu}_e$. Therefore, only disappearance experiments can be performed using the nuclear reactors as source of neutrinos.
The probability for an $\bar{\nu}_e$ to remain in an $\bar{\nu}_e$ state, at a given distance L from its production point is obtained from Eq. 2.18:

$$P(\bar{\nu}_e \to \bar{\nu}_e) = 1 - \sin^2(2\theta_{13}) \sin^2 1.27 \left(\frac{\Delta m^2_{13}(eV^2) L(km)}{E(GeV)} \right) \tag{3.1}$$

where $\Delta m^2_{13} \simeq \Delta m^2_{23}$. The disappearance probability is shown in Fig. 3.1, for two different values of Δm^2_{23}. Given the reactor $\bar{\nu}_e$ mean energy of $\langle E_{\bar{\nu}_e} \rangle \simeq 3$ MeV and the mass splitting $\Delta m^2_{23} \simeq 2 \times 10^{-3}$ eV^2, the first minimum of the oscillation probability is found at a distance $L \simeq 1100$ m from the $\bar{\nu}_e$ source.
The $\bar{\nu}_e$ are detected through inverse β-decay reaction (IBD) in liquid scintillator:

$$\bar{\nu}_e + p \to e^+ + n \tag{3.2}$$

The IBD reaction has a kinematical energy threshold of 1.8 MeV and provide a clear signal signature. The e^+ quickly looses its energy before it annihilates with an electron of the scintillator, producing two γ of 511 keV. The neutron could be captured on hydrogen, producing γ of 2.2 MeV. The signal then consists in a coincidence between a prompt event, produced by the positron with an energy related to the $\bar{\nu}_e$ energy, and a delayed event, produced by the neutron capture.
The signal signature is improved by doping the scintillator with gadolinium (^{155}Gd and ^{157}Gd) since it provides a better energy signature, with the emission of $\sim$ 8 MeV γ rays, and speed up the neutron capture process thanks

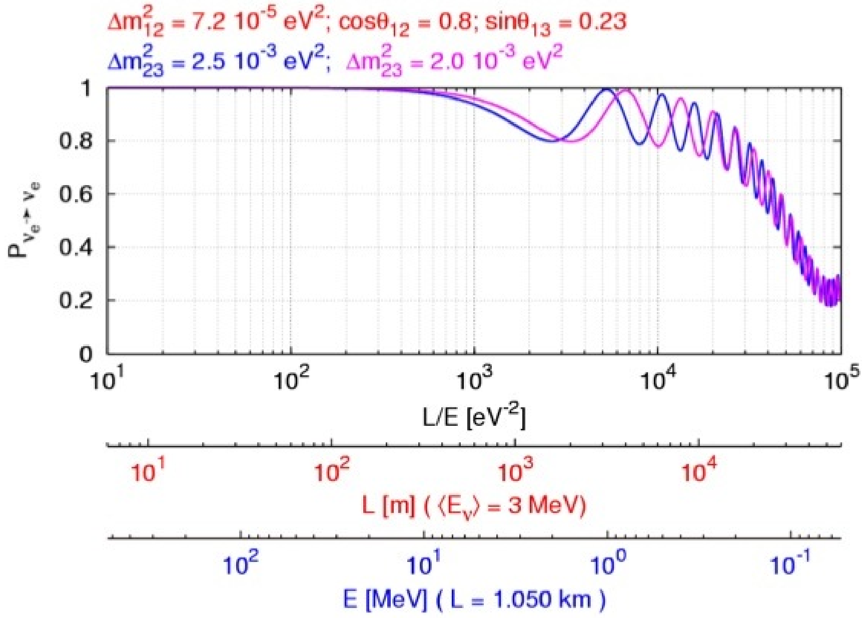

Figure 3.1: The $\bar{\nu}_e$ survival probability as a function of the parameter L/E, L and E separately, given fixed values of the other parameters. The blue curve corresponds to $\Delta m^2_{23} = 2.5 \times 10^{-3}$ eV^2 and the pink curve corresponds to $\Delta m^2_{23} = 2.0{\times}10^{-3}$ eV^2. For both cases, $\Delta m^2_{21} = 7.2{\times}10^{-5}$ eV^2, $\cos\theta_{12} = 0.8$ and $\sim \theta_{13} = 0.23$ were used.

to its high thermal neutron cross section.
In order to reduce the systematic errors two identical detectors are employed. A far detector, located around the first minimum of the $\bar{\nu}_e$ disappearance probability, measures the deficit in the $\bar{\nu}_e$ flux. A near detector, placed as closest as possible to the reactor core, measures the un-oscillated $\bar{\nu}_e$ flux, in order to get rid of the uncertainty on the knowledge of $\bar{\nu}_e$ flux. Furthermore, identical detectors at different distances allow to perform a relative measure reducing the detector related uncertainties.

This chapter describe in full details the Double Chooz experiment (DC). The detector design is described accurately in Sec. 3.1 highlighting the improvements with respect to the previous CHOOZ experiment. The detector read-out chain, from the photon electrons generated by the PMT to the waveform digitised by the FADC is described in Sec. 3.2. The online system which read, upon trigger, the FADC memories and write data events on disk is described in Sec. 3.3. Sec. 3.4 briefly describes the systems dedicated to the calibration of the detector response.
Sec. 3.5 discuss the simulation of the reactor $\bar{\nu}_e$ flux, used to obtain the expected neutrino energy spectrum to compare with the one measured by the FD and infer the value of the mixing angle θ_{13}. The detector Monte Carlo model and the simulation of the read-out chain used to simulate the detector response are described in Sec. 3.6 and 3.7.
Finally, the algorithms used to reconstruct important quantities such as the deposited charge, the energy and the interaction vertex of each recorded event are described in Sec. 3.8.

3.1 The Double Chooz detector

Two functional identical detectors located at different baselines from the nuclear reactors are employed by DC for $\bar{\nu}_e$ detection.
The FD is installed in the laboratory hall previously used by the CHOOZ experiment [36], located at a mean distance of 1050 m from the reactor cores, near the first oscillation minimum due to θ_{13}. The detector has an overburden of 300 m.w.e of rock, which reduce the muon trigger rate to about 10 Hz in the inner detector volume. An average of about 36 $\bar{\nu}_e$ /d has been observed by the FD in the period considered in Ch. 4 with about 2.2 evt./d of background contamination.
The near detector (ND) will be placed at a mean distance of 400 m from the reactor cores, where oscillation effects due to θ_{13} are expected to be negligible. The ND will have an overburden of about 120 m.w.e. As a result of the proximity of the ND to the reactors, a rate of 400 $\bar{\nu}_e$ /d is expected with a background contamination of about 11 evt./d [37].
The FD was build between 2009 and 2010 and is taking regular data since

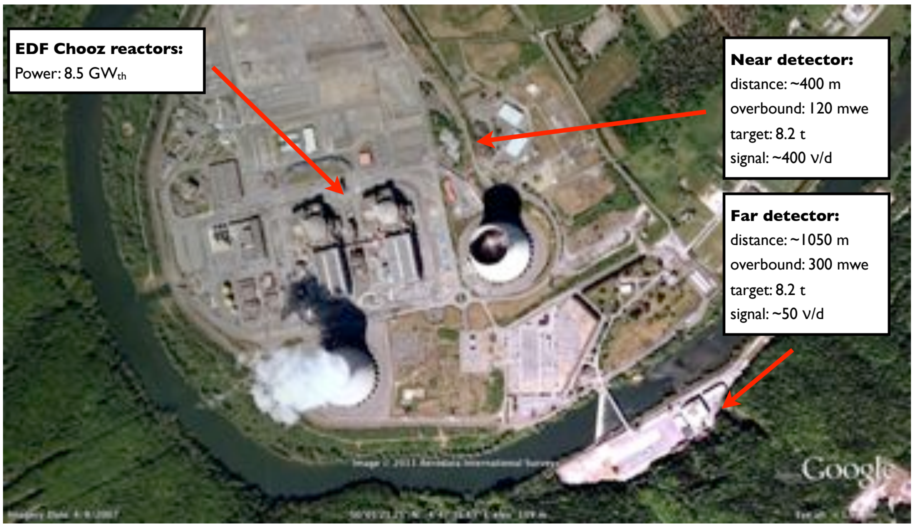

Figure 3.2: Aerial view of the experimental site.

April 2011. The near laboratory hall construction is expected to finish by the end of 2012 and the ND is expected to start data taking by the end of 2013. An aerial view of the experimental site is shown in Fig. 3.2.
The DC detector has been inspired by the former experiment CHOOZ. The detector design is shown in Fig. 3.3 and consists in three optically isolated sub-detectors: the inner detector (ID), the inner-veto (IV) and the outer-veto (OV). The ID consists of 3 cylindrical volumes namely, from inside to outside, target, gamma catcher and buffer. The IV is a cylindrical volume surrounding the ID. The OV is installed on the top of the cylindrical detectors and both for electronics and read-out point of views, is independent from the ID and the IV.
The setup has been optimised towards an higher neutrino detection rate and a larger signal over background ratio. The detector components have been chosen in order to constrain the radioactivity background level below 10 Bq in the ID [37].

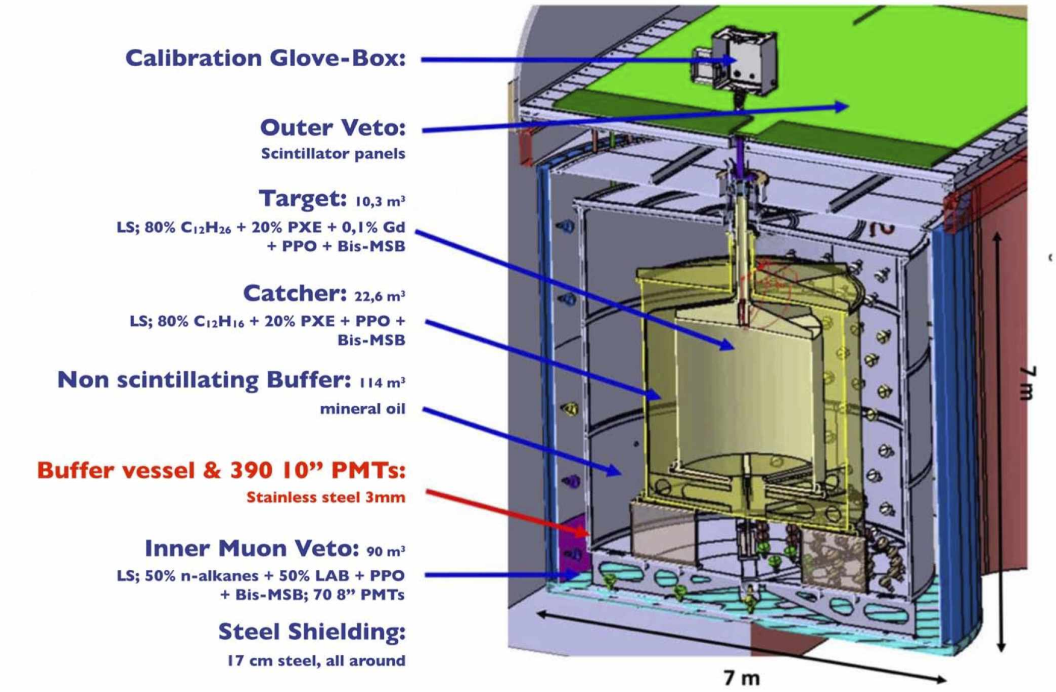

Figure 3.3: The DC FD design.

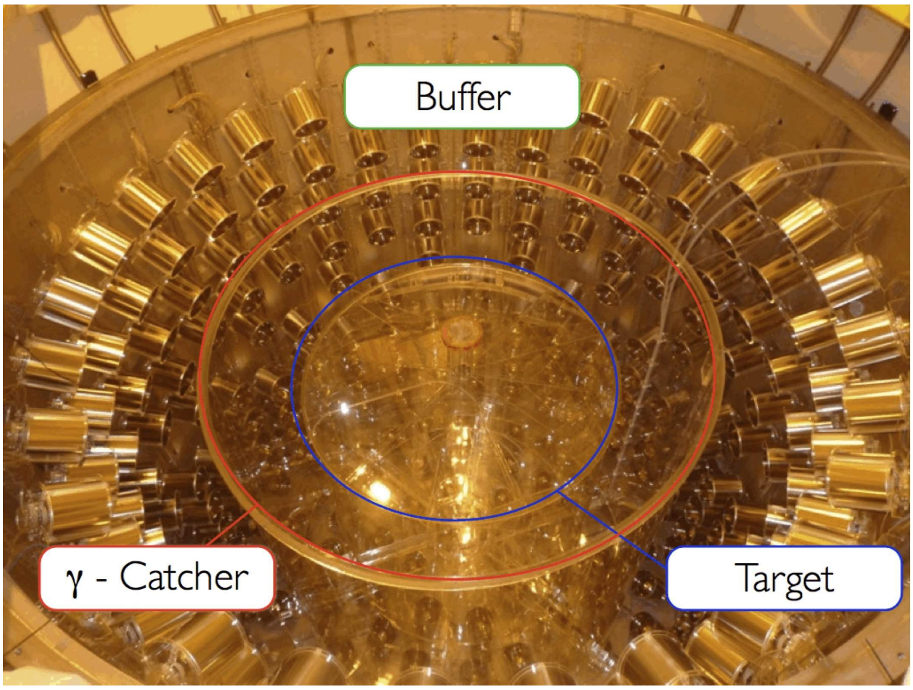

Figure 3.4: View of the Inner Detector. From inside to outside, the target, gamma-catcher and buffer volume equipped with 390 PMTs.

3.1.1 Target

The target volume (T) is the effective fiducial volume for $\bar{\nu}_e$ interaction. It consists in a 8 mm thick acrylic vessel filled with 10.3 m^3 of organic liquid scintillator.

The liquid scintillator in the target is composed of 80 % dodecane ($C_{12}H_{26}$), 20 % PXE (C_6H_{18}), 7 g/l of PPO, 20 g/l of bis-MSB and 1 g/l of Gd. PXE and dodecane are aromatic molecules which get easily excited or ionised by energy deposition. The energy is transferred non-radiatively to a PPO and bis-MSB molecule which shift the scintillating light frequency to match the PMT quantum efficiency range.

To ensure time stability of the Gd-doped liquid, the Gd atoms are encapsulated in a Gd(dpm)$_3$ molecule, for an efficient dissolving in the scintillator and a durable transparency. The optical stability of the liquid scintillator is granted by the stability of the energy peak of neutron capture on Gd, which has been found stable within 1 % over about one year [20]. This is one of the main improvement with respect to the CHOOZ experiment, which was limited in sensitivity because the optical instability of its liquid scintillator.

The proton number in the target (i.e. the absolute number of H nuclei) and its associated error are crucial parameters for the experiment. The error on the proton number is minimised by using a well defined and pure chemicals in combination with a precise knowledge of the weights of each chemical added in the scintillator production. The amount of scintillator in the target has been determined upon liquid thermalisation by weight measurement, with a precision of 0.04 %. The H fraction in the target scintillator is known with a 0.3 % precision [21].

3.1.2 Gamma Catcher

The gamma catcher volume (GC) surrounds the target with the function to collect gammas from IBD and n-Gd capture increasing the energy containment efficiency of the detector. It consists in a 12 mm thick acrylic vessel filled with 22.3 m^3 of liquid scintillator.

The GC liquid scintillator composition consists of 30 % dodecane, 66 % mineral oil, 4 % PXE, 2 g/l of PPO and 20 mg/l of bis-MSB. Liquid composition is tuned to match target liquid density and light yield to assure the safety of the acrylics vessel and increase uniformity of the detector response.

3.1.3 Buffer

The buffer optically isolates the ID from the IV and serves as support for the 390 ID photomultiplier tubes. The buffer is another main improvement with respect to CHOOZ design, its main function is to shield the T and the GC volumes from gammas radioactivity (mainly from PMTs photocathode) and neutrons created by muon interacting in the rock surrounding the detector. It consists in a 105 cm thick volume of 114 m^3 filled with non scintillating oil.

Oil composition consists of 47.2 % CobersolC70 and 52.8 % Ondina917 oils and has been chosen to ensure material compatibility with the GC acrylics vessel and PMTs and high transparency in the scintillator emission wavelengths.

3.1.4 Inner Veto

The IV is an active liquid scintillator detector surrounding the ID. Its main purpose is to shield the ID against low energy radioactive background and to detect with high efficiency cosmic muons and spallation neutrons crossing its volume.

The IV consists of a cylinder of 90 m^3 filled with liquid scintillator, $\sim$50 % n-alkanes and $\sim$50 % LAB (linear alkyl benzene) with 2 g/l of PPO and 20 mg/l of bis-MSB as wavelength shifters.

The IV is equipped with 78 PMTs fixed on the bottom, on the lateral surface of the 10 mm thick inner veto tank and on the upper buffer lid. The PMTs

Figure 3.5: View of the Inner Veto.

are contained in a stainless steel encapsulation, with transparent PET window at the front end. The capsules are filled with mineral oil to match the optical properties of the liquid scintillator. In order to increase light collection, reflective foils and white paint has been used to cover the outer buffer wall and the inner veto tank.
The number of IV PMT and their spatial configuration have been optimised through a dedicated MC simulation in order to obtain an homogenous detector response and maximise the light collection [52].

3.1.5 Shielding

The outer part of the IV is surrounded by 15 cm thick low activity and demagnetised stainless steel shielding. Its main purpose is to protect the detector from low energy gammas coming from the surrounding rock. The thickness and the shape of the shield was determined by a full detector simulation of the natural radioactivity backgrounds from the rocks.
Due to the limited size of the access tunnel, the shield was divided in about 50 pieces with a 60 degree "V" shape interface to mach two consecutive pieces. This is a major improvement with respect to CHOOZ, which used low radioactivity sands to shield the active part of the detector.

Figure 3.6: View of the Outer Veto.

3.1.6 Outer Veto

A further improvement with respect to the CHOOZ experiment is the OV. It is installed above the stainless steel shield, with the purpose to tag muons, which could cause $\bar{\nu}_e$ background events through muon correlated physics.
The OV allows to track (x, y) coordinates for muons passing through an area of 13 m × 7 m centred on the detector chimney. A smaller upper OV installed above the chimney allows to cover an area of 1.1 m × 0.30 m left open around the chimney.
The OV consists of 64 plastic scintillator strips of $5 \times 1 \times 320$ cm or 360 cm coupled to 1.5 mm diameter wavelength shifting optic fibers. The strips are superimposed to form x and y plane of 32 strips each.
To be noticed that the OV dimensions extend beyond the IV diameter to allow the tagging of near-by muons not entering in the detector, which could cause muon correlated physics in the ID.
The OV has been active for about 69 % of the data considered in this work, while the upper OV has been installed recently and is not considered here.

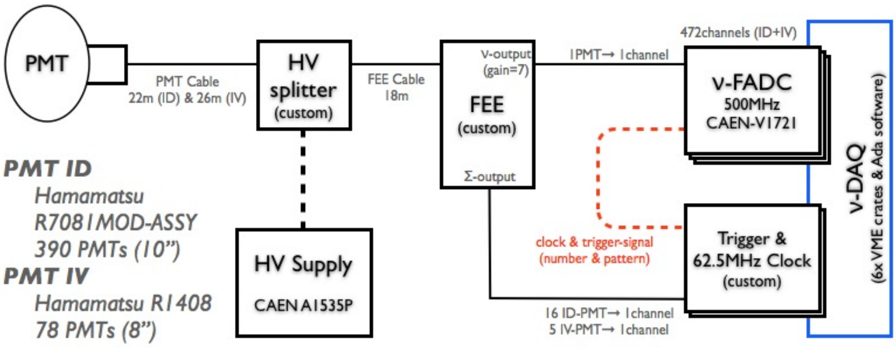

Figure 3.7: Schema of the FD read out chain and DAQ system.

3.2 The detector read-out

The read-out chain for both ID and IV is schematised in Fig. 3.7 from left to right. The OV has an independent read-out chain.

The energy deposited by a particle interacting within the active volume of the detector is converted in scintillation light by the liquid scintillator and, upon wavelenght shifting, reach the PMT photocathode surface.

The PMT converts the light into a charge signal which is carried outside the detector on the same cable as the high voltage. The signal is decoupled from the high voltage by the splitter and then sent toward the frond-end-electronics (FEE).

The FEE amplify the signals to match the dynamic range of the flash analog to digital converter (FADC) used to digitise the signals. At the same time the FEE sum the signals coming from different PMTs and send it to the trigger system which, upon discrimination, release the trigger signal to the FADC.

Once the trigger signal is received, the digitised waveforms are recorded by the data acquisition system (DAQ).

3.2.1 PMT and HV

To detect scintillation light the detector is equipped with 390 PMTs in the ID and 78 PMTs in the IV. The PMTs are powered by positive high voltage using CAEN modules SY1527LC and A1535P [3]. The HV values are tuned to provide a PMT gain of about 10^7.

ID PMTs are based on the model R7081 by Hamamatsu [5]. They have 10 inches photocathode with about 25 % quantum efficiency, provide a total coverage of about 13 % and a total photon detection efficiency around 5 %. Up to about 3 MeV of deposited energy, a single photoelectron (SPE) pulse is produced per channel. SPE pulses have an amplitude of about 5 mV after

40 m of cable and before the amplification provided by the FEE. Each ID PMT is shielded by a mu-metal cylinder to suppress effects from the earth magnetic field.
IV PMTs are based on the model R1408 by Hamamatsu, have 8 inches photocathode and provide a total coverage of about 0.6 %.
As shown in Fig. 3.8, the ID PMTs has a quantised SPE response following a simple Poisson statistics, while the IV PMTs have an exponential response, which make the calibration of the IV response more complicated.

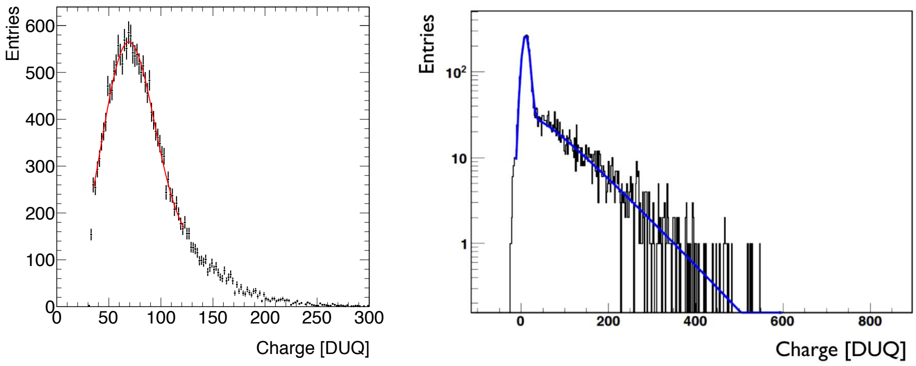

Figure 3.8: ID (left) and IV (right) PMTs single photoelectron response in arbitrary units of charge. The baseline has been subtracted for the ID PMTs response while it has not been subtracted for the IV PMTs response. The ID PMTs have a quantised SPE response which follow a Poisson statistics. The IV PMTs have an exponential SPE response described by a more complicated statistics, which makes the energy calibration of the IV more complicated.

3.2.2 FEE

The FEE boards were custom made to match the dynamic range of the FADC system. The FEE amplify the PMT signals with a gain of 7, which bring the amplitude of SPE pulses to about 40 mV. It also allows to reduce signal noise and to keep the baseline stability. The FEE also delivers the sum of the PMT signals, whose amplitude is proportional to the charge, to a custom trigger system.

3.2.3 FADC

The FADC cards are based on CAEN-VX1721 model, designed in partnership between CAEN and APC laboratory (Paris). A FADC card has 8 channels sampling signals at 500 MHz, with 8 bit resolution and 1 V dynamic range.

The FADC are designed to deal with signal from SPE/channel level up to about 50 MeV, without saturation. The 40 mV SPE pulse correspond to > 6 ADC counts. Energies up to the GeV level are covered with amplitude saturation, which leads to some degree of non-linearity above 100 MeV. The non-linearity is estimated up to 40 % above 500 MeV.

Every FADC channel has 2 MB of memory buffer, holding up to 1024 waveform of 4 μs length. The memory buffer is split into pages with adjustable size (i.e., read-out window length). Upon a trigger is received, the waveform is stored and the memory page is changed, giving the possibility to read-out the memory and continue to sample data without introducing dead times. The read-out window is set to 256 ns, which contain > 90 % of the scintillation light emitted. Each waveform consists then in 128 samples of 2 ns each.

Every PMT (390 from ID, 78 from IV) and FEE output (26 from ID and 18 from IV) are connected to a FADC channel, for a total amount of 512 FADC channels.

3.2.4 Trigger system

DC implements a custom trigger system which relies on the estimation of the deposited energy in the detector based on the analog sum of the signals provided by the FEE. There are four units: three trigger boards (TB) and one trigger master board (TMB). One TB is dedicated to trigger on the energy in the IV, the other two are dedicated to the ID.

ID trigger boards

ID PMTs are divided in 12 sectors containing 32 PMTs each. Half of the PMTs from a given sector are connected to the first trigger board TB-A while the others are connected to the second one TB-B. The FEE sums signals from a sector, by group of 16 PMTs, and sends it to the trigger boards. The PMTs are connected to the TBs in such a way each PMT connected to the TB-A is surrounded by PMT connected to TB-B and vice versa. Each TB looks at the same detector volume, so the trigger decision should be always the same among the two boards. This allows an intrinsic trigger efficiency monitoring (Sec. 4.4.1).

The trigger is made if the detector energy satisfies one of the two configurable thresholds: pre-scaled ($E \gtrsim 0.2$ MeV) and neutrino-like ($E \gtrsim 0.35$ MeV). In case one trigger condition is fulfilled, the TB form an eight bit word containing the trigger decision and sends it to the TMB.

IV trigger board

The IV is designed to identify possible muons and fast neutrons coming from outside the detector. The limited number of PMT and the geometry of the veto itself do not allow a precise measurement of the calorimetric energy deposited in the IV. For such reason the trigger condition is based on the hit pattern of groups of 3 to 6 PMTs. Particular attention is given on the event topology in the bottom part of the IV, which allows to know if a muon cross the entire volume or stops in the detector. Another 8 bit trigger word containing the trigger decision is sent to the TMB.

Trigger master board

The TMB receives the 8 bit words from the TBs. An OR logic is form if one of the bit of the trigger words is set to 1 and the trigger signal together with a 32 bit event number are distributed to the FADC. Other 8 bits are reserved for external trigger from the calibration system, OV and dead time monitor. The TMB also distributes a 62.5 MHz clock signal to all the FADC for synchronisation.

The dead time monitor release two trigger every second, asynchronous with the trigger clock, to monitor the read-out dead time and the FADC pedestal.

3.2.5 OV read-out

The OV read-out is independent from the ID and IV read-out. The light from the 64 OV scintillator strips is collected by optic fibers coupled at one end to the Hamamatsu M64 multi-pixel-PMT. The other end of the fiber is mirrored to reflect the light. The M64 is connected to a custom front-end board with the MAROC2 chip [40] which allows adjustment of the electronic gain of each pixel channel. Signals exceeding a common threshold are sent to a 12-bit ADC for digitisation and are read-out through a USB card.

The OV system is synchronised with the main read-out system through the TMB clock. The event timestamp is then used in the offline analysis to search for a coincidence between the OV and ID or IV triggers.

3.3 The online system

The online system is schematised in Fig. 3.9, from left to right. The FADC and the trigger boards are plugged into VME crates and read-out through VME-bus by the VME master card, called in the following read-out processor (ROP). The FD needs 5 VME crates with 5 ROPs, 4 for the FADC cards and one for the trigger system.

The data collected by the ROPs are sent to the event builder processor (EBP) and written on disk on binary files. A processing stage is performed

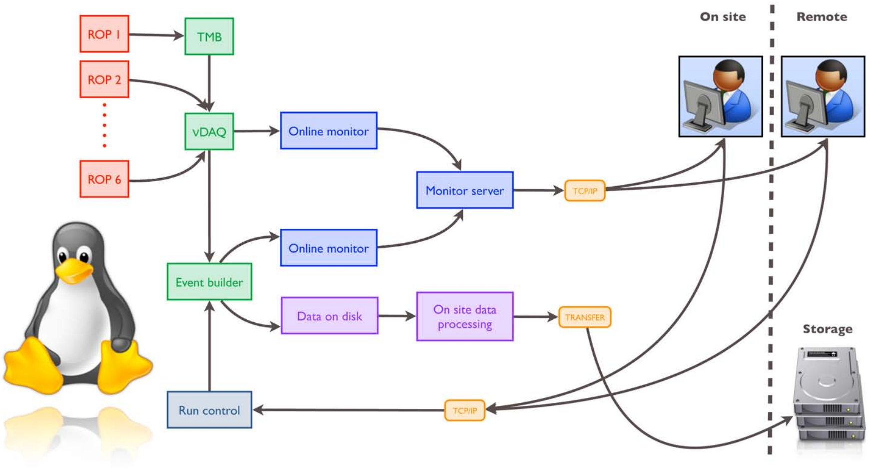

Figure 3.9: Schema of the FD online system.

to convert binary files into ROOT format [7]. The data are then sent to the main storage system at CCIN2P3 (Lyon, France) [1].
The data acquisition is controlled by both onsite and offsite (remote) shifter through the run control (RC) and monitored by a monitoring system.

3.3.1 Data acquisition

The data acquisition is performed by the 5 ROPs continuously polling the FADC cards to check if a trigger signal was received. When trigger is received the ROPs read-out the FADC memory buffer and sent the data to the EBP via TCP/IP protocol over 1 Gb/s ethernet connection.
The EBP is a multi-thread software which collects data from the different ROPs and write them on a binary file. One binary files per run is written on a local 450 GB disk. The raw data volume, produced by the read-out of 512 FADC waveform, amounts to about 64 kB/trigger, for a total amount of about 30 GB/hour or 720 GB/day given a trigger rate of about 140 Hz, as measured during the current data taking.

3.3.2 Run control

The RC and its Graphical user interface (GUI) represent the control interface between the shifter, both onsite or remote, and the DAQ. It allows to configure the parameters of the run through different run profiles (physics run, calibration run, test run, etc.), to start and to stop the data acquisition. The communication between the RC and the DAQ is provided by internet connection to the DAQ servers. For each run, related informations as start/stop time stamp, run length, shifter names, run profiles and comments are saved on a database.

3.3.3 Onsite data handling

The online data handling is performed by DataMigro, a daemon running on the background of a given machine able to perform a general set of tasks on the files of a given run.

DataMigro main action is to periodically query a database and check if a new run is ready to be processed. The status flag of each task is logged to the database together with an error flag to help the identification of misbehaviour and the expert troubleshooting. The status flag of a given task is used to trigger the next task. A recovery procedure is also supported and initiated upon an error flag is raised by a specific task as shown in Fig. 3.10. Like other online systems, DataMigro status is periodically reported to the data taking shift crews through a dedicated messaging system over network. In case of failure a detailed log is also sent to them.

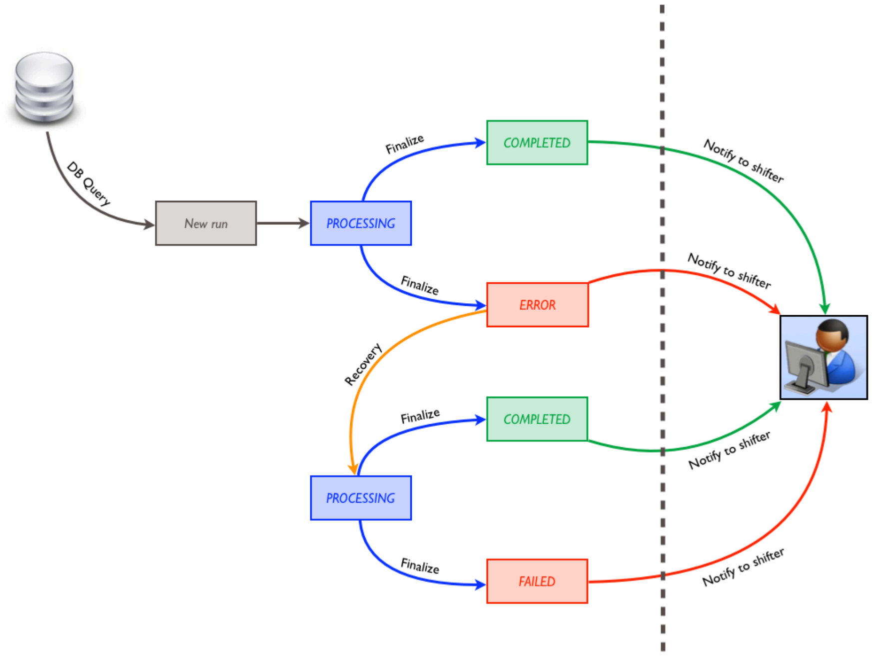

Figure 3.10: Schema of the DataMigro flag-driven logic

The schema of the tasks performed by DataMigro is shown in Fig. 3.11 from left to right. Once a new run is found, the very first task performed is the transfer of the binary files produced by the EBP on a storage server

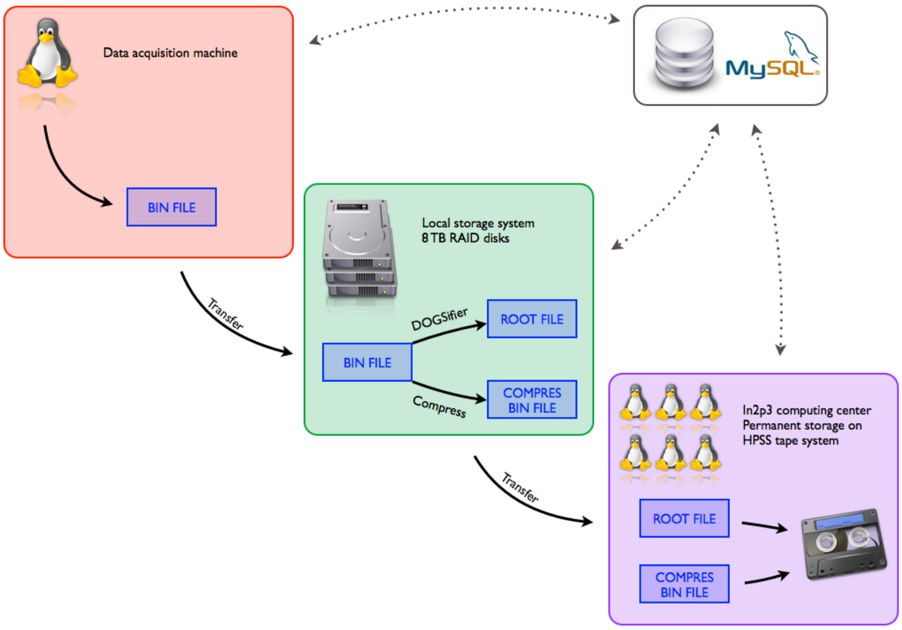

Figure 3.11: Schema of the tasks performed by DataMigro

with 11 TB of disk space in RAID[1] configuration. The storage server acts as a disk buffer and allow to store onsite about two weeks of raw data ($\sim$ 10 TB). Due the limited disk size of the EBP computer, once the binary files get successfully transferred on the disk buffer, they are removed on the EBP computer to make free room for the next runs. An high speed local network is used to transfer data at about 100 MB/s.

As soon as the binary files arrive on the storage server, another instance of DataMigro starts the next tasks. The binary files are compressed to reduce the file size by a factor $\sim$5 and then transferred to CCIN2P3. In parallel the binary files are translated by the DOGSifyer into DOGS[2] format, based on ROOT [7], and then transferred to CCIN2P3.

The files transfer to CCIN2P3 is performed through the Integrated Rule-Oriented Data System (iRODS) at about 10 MB/s. The iRODS system is a generic large data collection manager, implementing many different features the interested reader could found in [6]. For the need of the experiment, iRODS is used both for its high performance transfer protocol and its interface to the permanent CCIN2P3 High Performance Storage System (HPSS), a large scale tape storage server capable of 1 to 100 PB.

---

[1] Redundant array of independent disks

[2] DC Offline Group Software

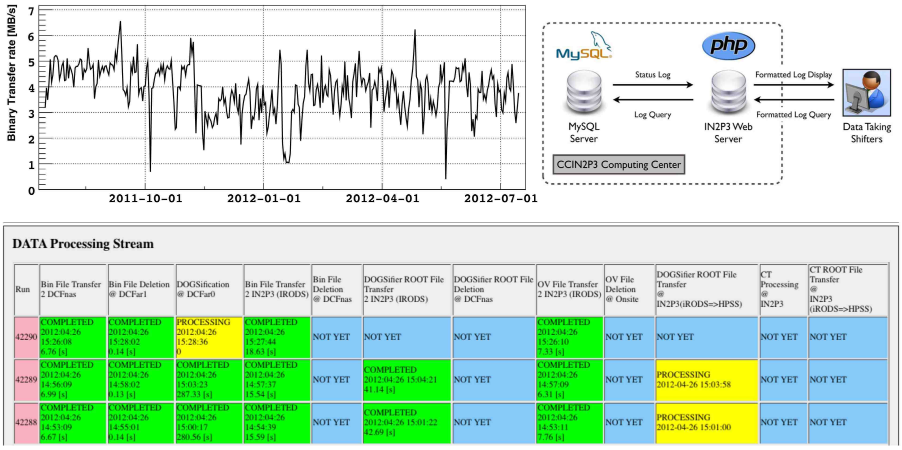

DATA Processing Stream

Run	Bin File Transfer 2 DCFnas	Bin File Deletion @ DCFar1	DOGSification @ DCFar0	Bin File Transfer 2 IN2P3 (IRODS)	Bin File Deletion @ DCFnas	DOGSifier ROOT File Transfer 2 IN2P3 (IRODS)	DOGSifier ROOT File Deletion @ DCFnas	OV File Transfer 2 IN2P3 (IRODS)	OV File Deletion @ Onsite	DOGSifier ROOT File Transfer @ IN2P3(iRODS=>HPSS)	CT Processing @ IN2P3	CT ROOT File Transfer @ IN2P3 (iRODS=>HPSS)
42290	COMPLETED 2012:04:26 15:26:08 6.76 [s]	COMPLETED 2012:04:26 15:28:02 0.14 [s]	PROCESSING 2012:04:26 15:28:36 0	COMPLETED 2012:04:26 15:27:44 18.63 [s]	NOT YET	NOT YET	NOT YET	COMPLETED 2012:04:26 15:26:10 7.33 [s]	NOT YET	NOT YET	NOT YET	NOT YET
42289	COMPLETED 2012:04:26 14:56:09 6.99 [s]	COMPLETED 2012:04:26 14:58:02 0.13 [s]	COMPLETED 2012:04:26 15:03:23 287.33 [s]	COMPLETED 2012:04:26 14:57:37 15.54 [s]	NOT YET	COMPLETED 2012:04:26 15:04:21 41.14 [s]	NOT YET	COMPLETED 2012:04:26 14:57:09 6.31 [s]	NOT YET	PROCESSING 2012-04-26 15:03:58	NOT YET	NOT YET
42288	COMPLETED 2012:04:26 14:53:09 6.67 [s]	COMPLETED 2012:04:26 14:55:01 0.14 [s]	COMPLETED 2012:04:26 15:00:17 280.56 [s]	COMPLETED 2012:04:26 14:54:39 15.59 [s]	NOT YET	COMPLETED 2012:04:26 15:01:22 42.69 [s]	NOT YET	COMPLETED 2012:04:26 14:53:11 7.76 [s]	NOT YET	PROCESSING 2012-04-26 15:01:00	NOT YET	NOT YET

Figure 3.12: Data-stream monitoring informations. Left: binary files transfer rate as a function of the day. Right: Schema of the data-stream monitoring. Bottom: data-stream monitoring web page.

Once both binary and ROOT files are successfully transferred at CCIN2P3 the files are removed from the local storage system after a configurable delay. A dedicate php-based framework has been developed to allow a simple query of the task status through a formatted, configurable and user friendly web page, as shown in Fig. 3.12. The web page allows shifters, both onsite and remote, and expert to monitor the data-stream from anywhere in the world.

3.3.4 Monitoring system

Different monitoring stages are performed on the data both during the data taking (online monitoring) and after (pseudo-online monitoring and offline monitoring). The online monitoring represents the lower level monitoring stage. It is performed by the EBP to ensure the correct behaviour of the DAQ and the trigger system. The pseudo-online monitoring is performed by the DOGSifyer to check the data quality. It takes care to flag bad/unexpected behaviour on an event and channel-wise basis. An event or a channel flagged as bad is not used during offline analysis. Finally the offline monitoring is performed during the offline data reconstruction.
Each monitoring stage consists in many independent monitoring units, which perform plots of different observables to be monitored to check the correct behaviour of the data taking and the quality of the data being taken. Output of the monitoring units is made available collaboration-wide through HTTP and java-based clients interfaces, to allow detector experts an early, quick and efficient diagnosis and troubleshooting. The origin of the misbehaviour is investigated by experts and normally solved in a short amount of

time. The outputs of two monitoring units developed during the detector commissioning are shown as example in Fig. 3.13 and 3.14.

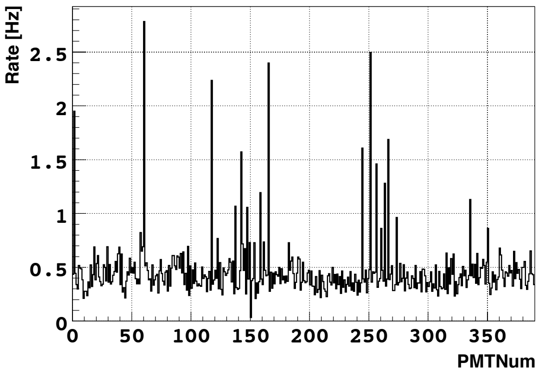

Figure 3.13: Rate of SPE pulses (roughly defined as waveform peak between 3 and 10 ADC counts) as function of the ID PMT number. This monitoring unit allows to identify noisy channel which presents SPE pulse rate higher than the average.

3.4 The calibration system

The knowledge of the detector response, the $\bar{\nu}_e$ detection efficiencies and their related systematics uncertainties are critical for the sensitivity of the experiment. As proposed in [37], the goal of DC is a relative error on detection efficiency of about 0.5 %. For such purpose it is important to determine accurately the scintillator response, the detector optical model, the energy scale and the time offset and gain of the PMTs. The goal of the calibration system is then to understand the detector behaviour through processes with well known particle, energy and position.

The experiment is calibrated using light sources, radioactive sources, cosmic muons and natural radioactivity. Optic fibers are used to inject light into the ID and the IV from a set of fixed points. The radioactive sources were deployed into the detector along the detector axis and the gamma catcher guide tube. Finally, cosmic rays are used to identify their interaction products such as Michel electrons, spallation neutrons and cosmogenic isotopes.

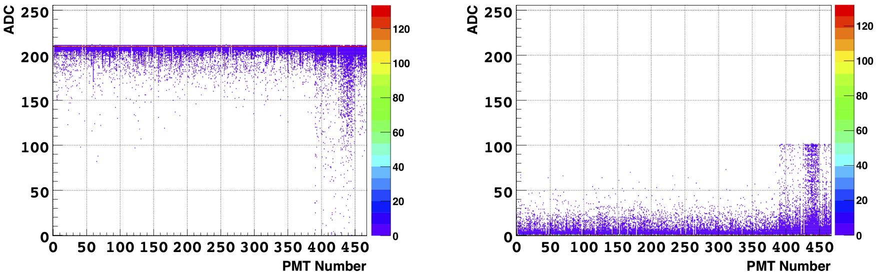

Figure 3.14: FADC baseline mean position (left) and RMS (right) as function of the PMT number. ID PMT are identified by PMT number smaller that 390 while IV PMT by number bigger than 390. This monitoring unit allows to identify abnormal channels through the position and the fluctuation of the FADC baseline.

3.4.1 Light Injection

LED fibers system is used to inject light of known waveform into the ID an the IV. The fibers are routed inside the detector on the edge of some PMTs. Some injection points are equipped with diffuser plates to illuminate widely the detector. The fibers are connected to a blue and UV LEDs flasher which rate and light intensity is controlled remotely. The light injection system is used daily to monitor the stability of the PMT gain and their timing response.

3.4.2 Radioactive Sources

Gamma sources ^{137}Cs (0.667 MeV), ^{68}Ge (2×0.511 MeV), ^{60}Co (1.173 and 1.333 MeV) and neutron source ^{252}Cf, whose rates is at the level of 50 Hz, have been deployed into the target and the gamma catcher.

Deployment in the target is performed along the symmetry axis using a motorised pulley-and-weight system, operated from a glove-box installed above the chimney. The deployment range span from 1 cm above the target bottom up to the target chimney, with 1 mm precision on the source position. Deployment in the gamma catcher is performed using a motor driven wire, guided through a rigid looped tube. The guide tube traverses the gamma catcher passing near the boundaries of the target and the buffer. The source position is known within 1 cm precision along the loop and the perpendicular distance between the source and the target wall is known within 2 mm.

3.5 Reactor neutrino flux simulation

Since the ND is not yet available, the simulation of the reactor $\bar{\nu}_e$ flux is a necessary step to obtain the un-oscillated $\bar{\nu}_e$ energy spectra to compare with the one measured by the FD. An accurate modelling of the reactor cores and the simulation of the time evolution of the reactor operation and fuel are required to obtain the energy spectrum corresponding to the time period covered by the data taking.

The $\bar{\nu}_e$ detected by DC are produced by two reactors located at the Chooz-B nuclear power plant operated by Electricité de France (EDF). Both reactors are PWR (Pressurised Water Reactor) N4 type with a thermal power of about 4.27 GW_{th} each (Fig. 3.15).

The reactor fuel consists in uranium dioxide (UO2) powder enriched with 3.45 % of ^{235}U and arranged in 205 fuel assemblies per reactor. More than 99.7 % of the energy production comes from the fission of four main isotopes, ^{235}U, ^{239}Pu, ^{238}U and ^{241}Pu. The fission is initiated by a thermal neutron, and releases a mean energy of about 200 MeV. Nuclear fuel in the reactor vessel is engaged in a fission chain reaction producing lighter nuclei but also γ rays, fast neutrons and β particles. Antineutrinos are produced by the β-decay of the fission products.

The kinetic energy of reaction products heat the water in the primary coolant loop up to 320°. To prevent the primary coolant loop water to boil, the circuit is kept under a pressure of typically $150 - 160$ bar. The hot primary coolant is pumped into a heat exchanger, where it flows through hundreds or thousands of tubes. Heat is transferred through the walls of these tubes to the lower pressure secondary coolant circuit where it evaporates to pressurised steam. The transfer of heat is accomplished without mixing the two fluids, which is desirable since the primary coolant is radioactive. The pressurised steam is fed through a steam turbine which drives an electrical generator connected to the electric grid for distribution. After passing through the turbine the secondary coolant is cooled down and condensed in a condenser. The condenser converts the steam to a liquid so that it can be pumped back into the steam generator. The yield of this thermal power transformation is ~ 33 %.

One third of the fuel needs to be changed on ~ 12 months cycle, and for this reason one reactor is expected to be off about one month per year.

3.5.1 Expected $\bar{\nu}_e$ rate

The expected rate of $\bar{\nu}_e$ interaction in the detector is given by:

$$R_{exp.} = \frac{\epsilon N_p}{4\pi} \sum_{R1,R2} \frac{1}{L_R^2} \frac{P_{th}^R}{\langle E_f \rangle_R} \langle \sigma_f \rangle_R \tag{3.3}$$

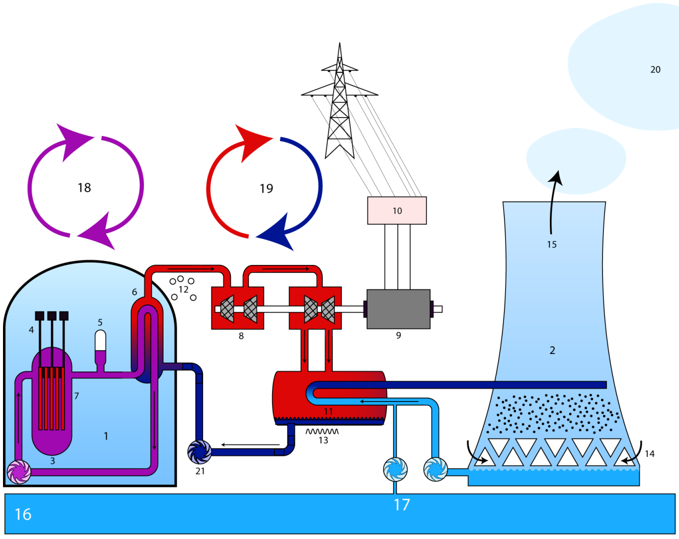

1. reactor block
2. cooling tower
3. reactor
4. control rod
5. support for pressure
6. steam generator
7. fuel element
8. turbine
9. generator
10. transformer
11. condenser
12. gaseous
13. liquid
14. air
15. air (humid)
16. Meuse river
17. cooling-water circulation
18. primary circuit
19. secondary circuit
20. water vapor
21. pump

Figure 3.15: Schematic view of a PWR nuclear plant.

where the sum is performed over the two reactor cores. The term ϵ is the total detection efficiency, N_p is the number of protons in the target volume, L is the detector distance from the center of each reactor, P_{th} is the reactor thermal power, $\langle E_f \rangle$ is the mean energy released per fission and $\langle \sigma_f \rangle$ is the mean cross section per fission. The first three terms depend on the detector and are constant. The last three terms instead depend from the reactors and are time dependent. The reactor thermal power depend on the operation of the reactor, while $\langle E_f \rangle$ and $\langle \sigma_f \rangle$ depends on the evolution of the fuel composition.

3.5.2 Reactor thermal power

The instantaneous thermal power of each reactor core is provided by EDF and is evaluated over time steps of 1 minute. This information and other important variable for the reactor core modelling are downloaded every two weeks and stored in a database.

The instantaneous thermal power is derived from in-core instrumentations measuring the temperature of the water in the primary cooling loop. The thermal power in-core measurement is cross-checked and calibrated though heat balance in the secondary cooling loop.

Since the accuracy of the thermal power measurement determines the maximum power at which the reactor can operate, EDF has performed a detailed study of the uncertainty in this measurement [94], resulting in the maximum thermal power of $P_{th} = 4250.0 \pm 12.2$ MW (0.4 % at 95 % CL). The thermal power for both Chooz reactors is shown in Fig. 3.16 as a function of the day since the FD data taking has started.

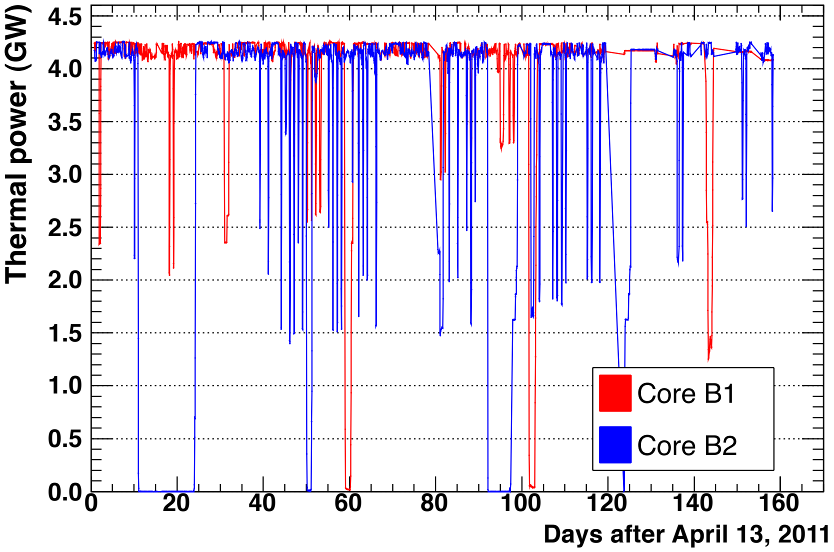

Figure 3.16: Chooz reactors thermal power, from EDF measurements, as function of the day, since the FD data taking has started. The observed variation of the thermal power reflect the status of the operation of the reactors. Single reactor off periods (i.e. thermal power drop to zero) of few days are also visible.

3.5.3 Mean energy per fission

The mean energy per fission $\langle E_f \rangle$ is given by:

$$\langle E_f \rangle = \sum_k \alpha_k \langle E_f \rangle_k \tag{3.4}$$

where α_k is the fractional fission rate of the k-th isotope contributing to the neutrino production by its β-decay and $\langle E_f \rangle_k$ is the mean energy released per fission by the same isotope. The values of $\langle E_f \rangle_k$ are taken from [69] and summarised in Tab. 3.1.

Isotope	$\langle E_f \rangle_k$ [MeV]
^{235}U	201.92 ± 0.46
^{239}Pu	209.99 ± 0.60
^{238}U	205.52 ± 0.96
^{241}Pu	213.60 ± 0.65

Table 3.1: Mean energy released per fission by the isotopes contributing to the neutrino production [69].

3.5.4 Mean cross section per fission

The mean cross section per fission is effectively a cross section averaged over the $\bar{\nu}_e$ spectra from the different fission isotopes:

$$\langle \sigma_f \rangle = \sum_k \alpha_k \langle \sigma_f \rangle_k = \sum_k \alpha_k \int_0^\infty S_k(E) \sigma_{IBD}(E) dE \tag{3.5}$$

where α_k is the fractional fission rate, $S_k(E)$ is the reference $\bar{\nu}_e$ spectrum and σ_{IBD} is the inverse β-decay cross section.

The $\bar{\nu}_e$ spectrum for each fission isotope is the result of the β-decays of many different fission products. The reference spectra for ^{235}U, ^{239}Pu and ^{241}Pu are derived in [65], converting the measurements of the β spectra performed at the ILL research reactor. The ^{238}U spectrum is obtained from an *ab initio* calculation performed in [75]. *Ab initio* calculation for ^{238}U spectrum is necessary since this isotope is fissioned only by fast neutrons and no direct measurement of its β spectrum is available at the moment. The reference spectra are shown in Fig. 3.17.

The conversion of the β spectra has been improved by using more data on the many β-decay branches and high order energy corrections [65, 75]. Since ILL spectra were measured after 1 day irradiation of U or Pu, contributions from decays with life times longer than 1 day were considered [75]. The uncertainty on these reference spectra is energy dependent but is of the order of 3 %.

3.5.5 Inverse beta decay cross section

The $\bar{\nu}_e$ energy spectrum in the detector is obtained considering the simplified inverse β-decay cross section from [95]:

$$\sigma_{IBD}(E_\nu) = E_{e^+} K \sqrt{E_{e^+}^2 - m_e^2} \tag{3.6}$$

where E_{e^+} and m_e are the positron mass and energy and the constant $K = 0.961 \times 10^{-43}$ cm^2 MeV^{-2} has been found using the neutron life time

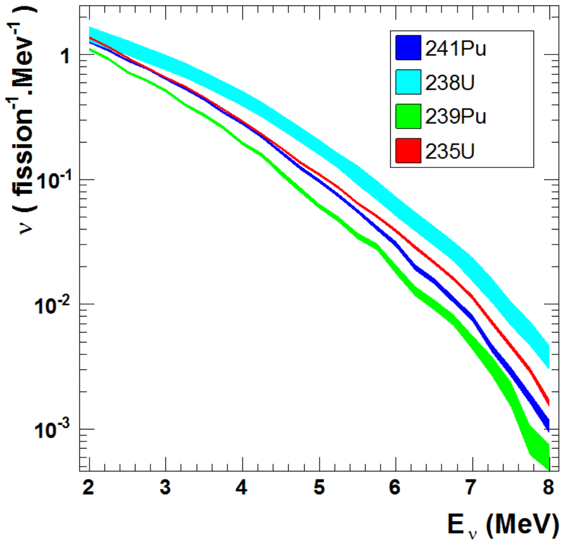

Figure 3.17: Reference $\bar{\nu}_e$ spectra from [65, 75] and related uncertainties.

measured in [84]. The $\bar{\nu}_e$ energy is related to the positron energy by:

$$E_{e^+} = \frac{1}{2}\left(\sqrt{m_n^2 - 4m_p\left(\frac{\Delta^2 - m_e^2}{2m_p} + \Delta - E_\nu\right)} - m_n\right) \tag{3.7}$$

where m_p and m_n are the masses of the proton and the neutron respectively and $\Delta = m_n - m_p$.

3.5.6 Fission rates

The fission rates α_k evolve in time depending from the reactors thermal power and the evolution of the fuel assemblies. The thermal power for a given fission is relatively insensitive to the specific fuel composition since the mean energy released per fission differs by less than 6 % among the different isotopes. However the detected number of $\bar{\nu}_e$ directly depend from the different spectra of the isotopes. For such reason an accurate modelling of the evolution of the reactor core has been developed.

Two complementary simulation codes have been used to model the reactor cores evolution, MURE and DRAGON [72, 70]. MURE is a Monte Carlo code which use a statistical approach to solve the neutron transport equation in a 3-D reactor core. DRAGON uses a deterministic approach to solve, with some approximations, the neutron transport equation in a 2-D core. The performance of the codes are compared against each other and validated against data from the Takahama-3 reactor [67].

The EDF provided the informations required to simulate the fission rates as a function of the time, including initial burnup[3] of the assemblies. To determine the inventories of each assembly composing the core at the startup of the data-taking cycle, assemblies simulations are performed and the inventories at the given burnup computed. Fission rates as a function of the day are shown in Fig. 3.18 and their averaged values are summarised in Tab. 3.2. The systematic uncertainty on the fission rates are obtained by varying different input parameters of the simulation, such as the thermal power, the boron concentration, the water and fuel temperatures, the mean energy released per fission and the geometrical parameters of the cores. The maximum discrepancies observed comparing the two different simulation code are also included in the fission rate systematic error. The breakdown of uncertainties for ^{235}U is shown in Fig. 3.19 as an example.

Isotope	$\langle \alpha_k \rangle$
^{235}U	0.469 ± 0.016
^{239}Pu	0.351 ± 0.013
^{238}U	0.087 ± 0.006
^{241}Pu	0.066 ± 0.007

Table 3.2: Averaged fission rate $\langle \alpha_k \rangle$ of the isotope k, as obtained by the simulation of the reactor evolution.

3.5.7 Bugey4 normalisation and errors

The large uncertainties in the reference spectra limit the DC sensitivity to θ_{13} in the current far-detector only configuration. This effect is reduced *anchoring* the normalisation of the mean cross section per fission to the Bugey4 rate measurement at 15 m from the Bugey reactor core [51]:

$$\langle \sigma_f^{DC} \rangle = \langle \sigma_f^{Bugey} \rangle + \sum_k (\alpha_k^{DC} - \alpha_f^{Bugey}) \langle \sigma_f \rangle_k \qquad (3.8)$$

The second term correct for the different core inventories of the Bugey4 with respect to the Chooz reactors. Since the correction term is small (0.9 ± 1.3) %, the uncertainties on the reference spectra are suppressed and the dominant uncertainty comes from the Bugey4 measurement, of about 1.4 %. Using the Bugey4 measurement as anchor point, the overall contribution of the reactor related systematics decrease from 2.7 % to 1.7 %. The

---

[3] Measure of how much energy is extracted from a primary nuclear fuel source. It is measured as actual energy released per mass of initial fuel in gigawatt-days/metric ton [GWd/t]

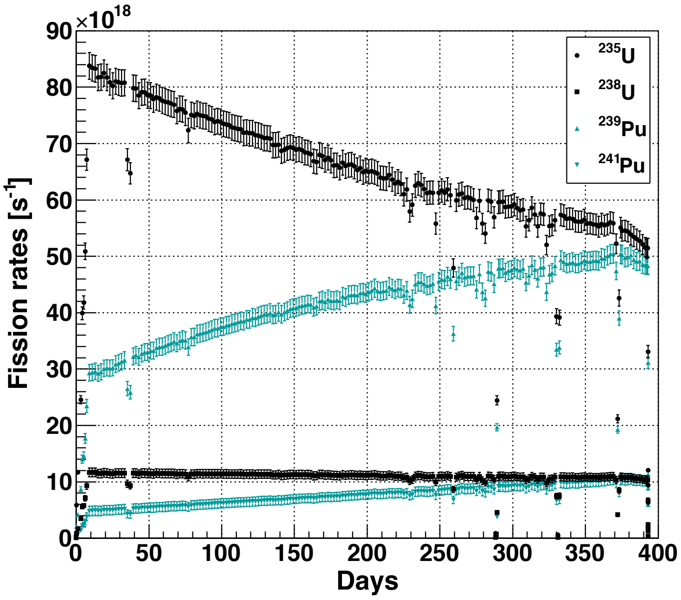

Figure 3.18: Fission rates as function of the day since start of data taking, as obtained by the simulation of the reactor evolution. The decrease of the U isotopes and the increase of the Pu isotopes reflect the evolution of the reactor fuel, which burn U isotopes creating Pu isotopes.

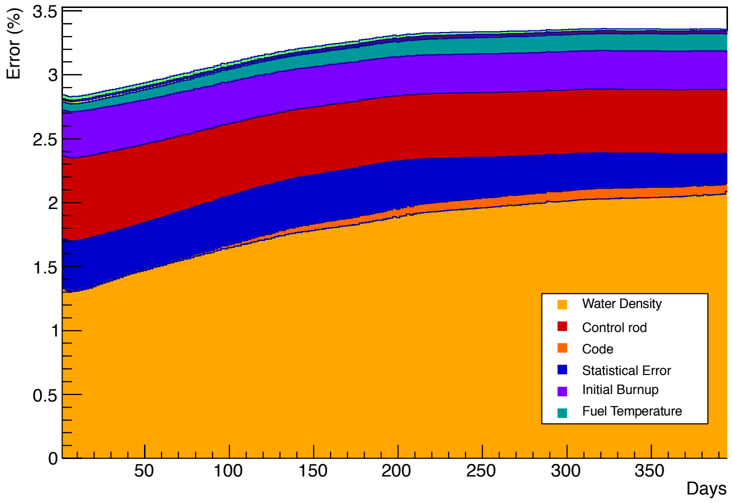

Figure 3.19: Breakdown of simulation uncertainties on the ^{235}U fission rate, as obtained by varying different input parameters of the simulation.

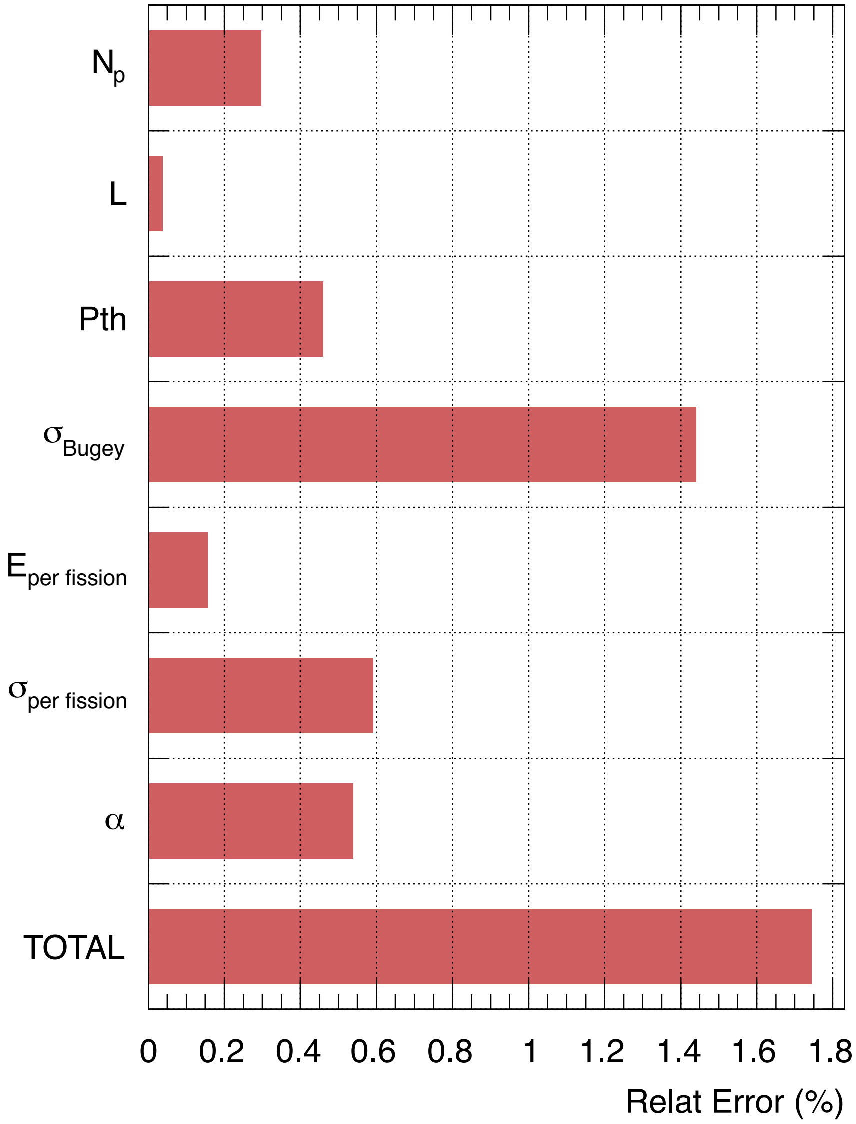

Figure 3.20: Breakdown of uncertainties on the reactor $\bar{\nu}_e$ rate prediction from Eq. 3.3. The main contribution to the total uncertainty comes from the normalisation of the mean cross section per fission to the Bugey4 measurement, of about 1.4 %. Nevertheless, the use of the Bugey4 measurement as anchor point reduce the overall systematics from 2.7 % to 1.7 %.

breakdown of the different contribution to the prediction of the reactor $\bar{\nu}_e$ rate uncertainty is shown in Fig. 3.20.

3.6 Detector simulation

The detector response is modeled through a detailed Geant4 [4] simulation with improvements on the scintillation process, photocathode optical surface model and thermal neutron model.

The custom scintillation process implements detailed light waveforms, spectra, re-emission and Birks law quenching. The photocathode model is based on a standard model of a thin, semitransparent surface with absorption and refractive index, including also the photoelectron collection efficiency as a function of the position of the emission on the photocathode. The custom neutron thermalization process implements molecular elastic scattering for neutrons below 4 eV and a radiative capture model with improved final state gamma modeling.

The detector geometry is modeled to a fine level of details, with a particular regard to the geometry of the PMTs, the mu-metal shield and all the materials near the active volume such as tank walls and supports. The dimension of the tank walls, of the supports and the position and orientation of the PMTs were checked during installation and verified by photographic survey with sub-mm accuracy.

The optical parameters used in the detector model are based on dedicated measurements [8] and tuned with calibration data. The scintillator emission spectrum, light attenuation and quenching were measured on scintillator sample with dedicated laboratory setup [21].

The $\bar{\nu}_e$ events are generated in correspondence with data taking runs, with fluxes and rates obtained through the reactor simulations. The radioactive decays from calibration sources were simulated using detailed models of nuclear levels for each source, taking into account branching ratios and energy spectra.

3.7 Read-out system simulation

The Geant4-based detector simulation outputs the deposited charge and the time at which each PE strikes the photocathode of each PMT. The read out system simulation (RoSS) converts these informations into an equivalent waveform as digitised by the FADC.

RoSS accounts for the response of elements associated with detector readout as the PMTs, FEE, FADC, trigger system and DAQ. The simulation relies on the measured probability distribution function (PDF) to empirically characterise the response to each single PE as measured by the full read-out chain.

A dedicated setup consisting in one read-out channel was built to measure most of the necessary PDFs and to tune the design of the full read-out chain. Variation channel-to-channel such as gains, baselines, SPE width, etc. are considered including dispersion effects. In this way the simulation exhibit non-linearity effects as observed in the data. Upon calibration, data and MC energies agree within 1 %.

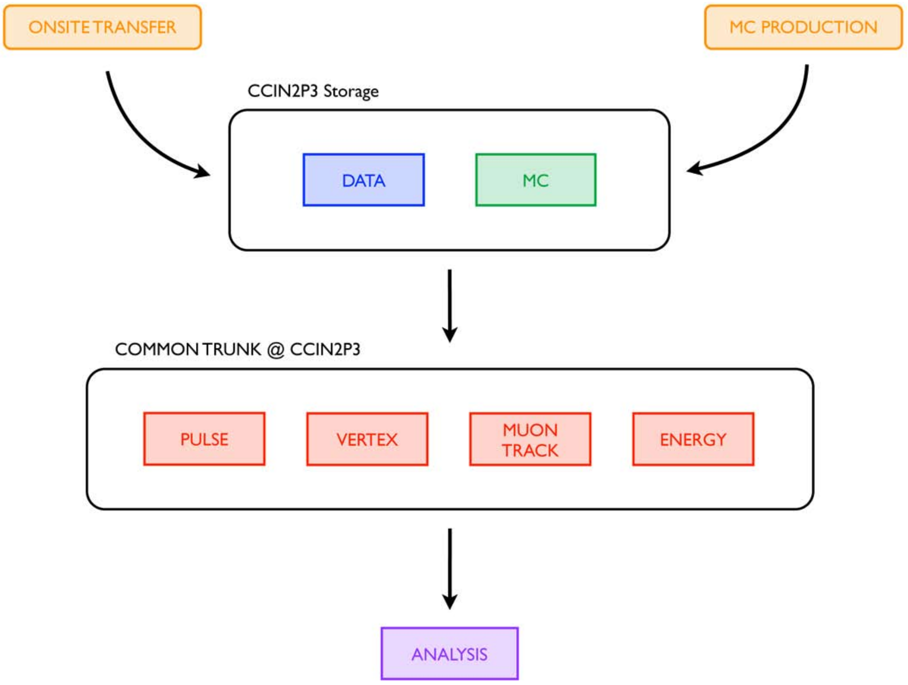

Figure 3.21: Schema of the DC reconstruction strategy. Both data and MC follows the same reconstruction process, performed at CCIN2P3 by the Common Trunk.

3.8 Data reconstruction

Both data and MC are subjected to the same reconstruction process, performed by the common trunk (CT). The CT takes place at CCIN2P3 as soon as the MC generation ends or the data files are transferred from onsite. A schematic view of the reconstruction steps performed by the CT is shown in Fig. 3.21.

For each event, the pulses contained in the digitised waveforms are reconstructed to obtain charge and timing information. Such informations are then used to reconstruct the interaction vertex, the muon track (if a muon is identified) and the deposited energy.

Once reconstructed, data and MC are made available to the whole collaboration for analysis.

3.8.1 Pulse reconstruction

The pulse reconstruction is performed by a custom code called "DCRecoPulse", a collection of generic algorithms and tool meant to perform pulse charge and timing reconstruction as well as baseline analysis.
The estimation of the baseline is the first step to be performed toward charge reconstruction, since it needs to be substracted to obtain the actual signal. The baseline of each channel can be estimated either from short time window (few ns) prior to each signal (floating baseline estimation), or from a full time window in special events taken by the two external triggers with a rate of 1 Hz (external baseline estimation) [78]. The floating baseline method depends on the position of the pulse within the read-out window. It is not valid for broad pulses coming from instrumental noise, which are usually located at the beginning of the read-out window. On the other hand external baseline method is known to be biased if the external trigger happen after a large energy deposition, such as muons. For this reason an hybrid schema is adopted. The pedestal estimation from the floating method is adopted by default, but if the RMS of the floating pedestal is larger than 0.5 DUQ[4] than the RMS obtained from the external method, the pedestal obtained from the external method is employed for the channel [79].
The pulse charge is reconstructed used the so called "sliding window" algorithm. The maximum charge is searched in a fixed size time window. Once the peak of the pulse containing the maximum charge is reconstructed, the integration window is slide in another part of the waveform, until the charge in the integration window falls below a given threshold. To ensure the reconstructed pulse actually comes from PE signal and not from pedestal fluctuation, the threshold on the measured charge is set as:

$$Q_{min} = n_\sigma \times \sigma_{ped} \times \sqrt{WS} \tag{3.9}$$

Where n_σ is the number of σ_{ped} defining the threshold amplitude and WS is the integration time window size [78]. With some consideration on charge integration efficiency, impact on SPE resolution and linearity of the energy scale, the charge threshold is set as 1 sigma away from pedestal fluctuation, while the integration time window size is set at 112 ns [79].
In addition, for each pulse some timing characteristics are also computed (Fig. 3.22):

Start time: time at 30 % of maximum amplitude before it is reached

---

[4] Digital Unit of Charge, defined as integral of the Digital Unit of Current (DUI, i.e. ADC counts).

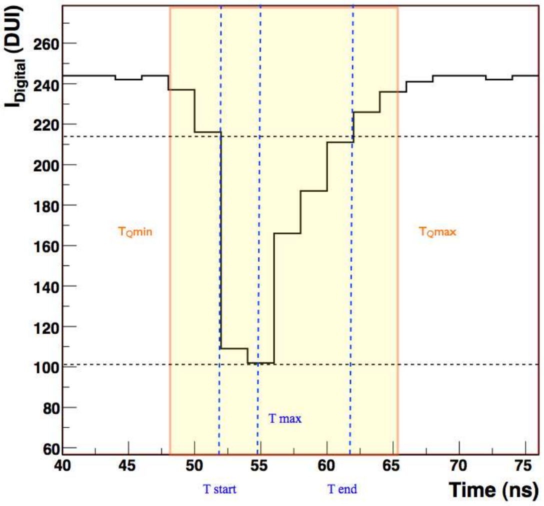

Figure 3.22: Schema of the reconstructed pulse timing characteristics

End time: time at 20 % of maximum amplitude after it is reached

Max amplitude time: time at maximum amplitude

Rise time: difference between max amplitude time and start time

Fall time: difference between end time and max amplitude time

3.8.2 Vertex reconstruction

The vertex reconstruction is based on charge and time maximum likelihood algorithm using hit/no-hit probability for each PMT. The event is assumed to be a point like source of light and characterised by $\mathbf{X} = (x_0, y_0, z_0, t_0, \Phi)$, where (x_0, y_0, z_0) represent the event position within the detector, t_0 is the event time and Φ is the light strength (number of photons per sr.). The amount of light and the arrival time at the $i-$th PMT is predicted as:

$$\mu_i = \Phi \times \epsilon_i \times \Omega_i A_i \tag{3.10}$$

and

$$t_i^{(pred)} = t_0 + \frac{r_i}{c_n} \tag{3.11}$$

where ϵ_i is the $i-$th PMT quantum efficiency, Ω_i is the solid angle subtended by the PMT at a distance r_i from the the event vertex, A_i is the light transmission amplitude, and c_n is the effective speed of light in the medium.

The likelihood is defined as:

$$\mathcal{L}(\mathbf{X}) = \prod_{q_i=0} f_q(0;\mu_i) \prod_{q_i>0} f_q(q_i;\mu_i) \times f_t(t_i;t_i^{(pred)};\mu_i) \tag{3.12}$$

The first product concerns only PMTs that have not been hit, while the second product concerns the remaining PMTs that have been hit (non-zero charge q_i reconstructed at time t_i). The two function f_q and f_t are the charge and time probability density function obtained from MC simulation and validated against physics and calibration data [66]. The event reconstruction consists to find the set of event parameters $\mathbf{X}_{min}$ which minimise the negative log-likelihood function:

$$F(\mathbf{X} = -\ln \mathcal{L}(\mathbf{X}) = -\sum_i \ln f_q(q_i;\mathbf{X}) + \ln f_t(t_i;\mathbf{X}) = F_q(\mathbf{X}) + F_t(\mathbf{X}) \tag{3.13}$$

The vertex reconstruction can be performed using only one of the two terms in Eq. 3.13, F_q to perform charge-only reconstruction, or F_t to perform time-only reconstruction, but using information from both charge and time improves the vertex accuracy. The vertex reconstruction accuracy was evaluated using ^{60}Co calibration source deployed at known positions along the z-axis and the guide tube. Source positions were reconstructed with a spatial precision of about 12 cm [80].

During the detector commissioning, a first preliminary validation of both the vertex reconstruction algorithm and the liquid scintillator time response was provided studying the time response of the scintillator. The scintillator time response of Fig. 3.23 shows the characteristic time behaviour of the liquid scintillator such as the fast excitation time ($\sim$ few ns) and the slower de-excitation ($\sim$ few hundreds ns), it also shown the expected 4 ns time spread around the peak (vertex resolution and read-out time spread) and hint of PMT late pulse at about 60 ns.

3.8.3 Muon tagging and track reconstruction

Cosmic muons that reach the underground detector hall, cross the detector and deposit large amounts of energy. More importantly, the muon-correlated physics that follows the passage of a muon in the detector (mainly fast neutrons and cosmogonical-produced isotopes) could mimic the $\bar{\nu}_e$ signature. For such reasons it is important to tag muons crossing the detector and reconstruct their track.

Tagging a muon is not only about identifying a pure sample of cosmic-muons going through the detector, but identifying the muon or any indirect traces associated to the presence of cosmic-muons in the neighborhood of the detector. Examples of indirect traces of the presence of a muon in or near the detector are the observation of Michel electrons/positrons (whose beta spectrum can reach $\sim$ 60 MeV) and fast neutrons (whose detection is granted

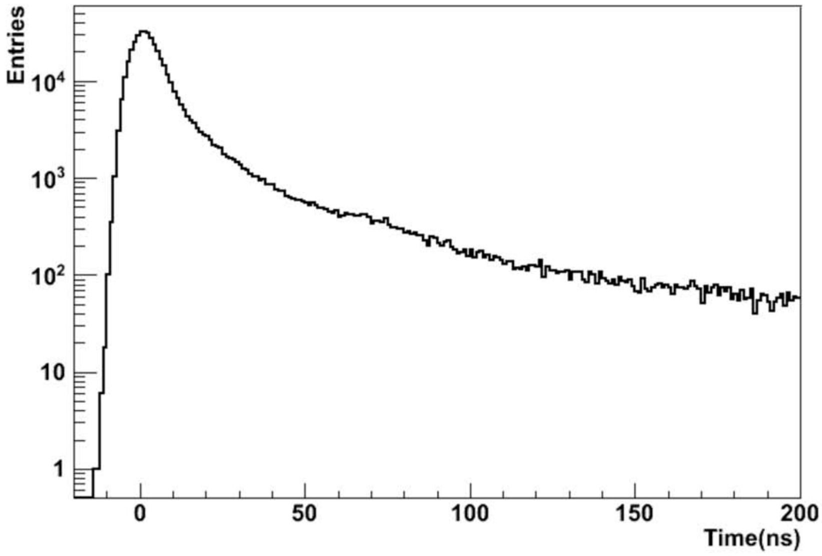

Figure 3.23: Scintillator time response obtained from the PMT pulse start time, corrected by the time of flight of the light between the interaction vertex and the PMT itself.

via neutron captures or via proton recoils).
The IV detector was designed to tag through going muons with very high efficiency. The IV was configured to be self-triggered at around ~ 10 MeV equivalent energy deposition, at the inflection point of the IV energy spectrum in between the natural radioactivity dominated region and the muon dominated region. Through going cosmic muons are expected to be unmissable since ~ 100 MeV (i.e., roughly 49 cm $\times$ 2 MeV/cm for a MIP-μ) of deposited energy is expected. The IV-detector based tagging is set as low as possible around self-triggered energy threshold, $Q_{IV} = 10^4$ DUQ (i.e., roughly 4×1 MeV, which is 4×2174 DUQ = 8588 DUQ as obtained by an approximate IV energy calibration using through-going muons). This cut is expected to tag mainly through going muons (IV or both ID and IV) and fast neutron (via proton recoil in the IV). Dedicated studies performed within the collaboration demonstrate that the IV efficiency, monotonically increasing with the energy deposited in the IV, is > 99.999 % at 10^4 DUQ. Therefore, the only place where muons can sneak into the ID undetected by the IV is via the chimney. There the ID can be used to tagged those events. The tagging based on the ID allows to identify the Michel electron from muon entering through the chimney and stopping on the top of the ID, therefore not crossing the IV. If the muon did not stop, it would be tagged

as it goes through the bottom part of the IV. In addition, the muon is also tagged by the large deposition in the ID due to the long track. A cut of $E_{ID} = 30$ MeV is set. This means that a sneaking muon is tagged via its track-length in the scintillator ($\Delta x > 15$ cm for $\Delta E = 30$ MeV) or via its Michel electron ($\Delta E > 30$ MeV, which covers $\sim 50\%$ of the Michel electron energy spectrum).

Dedicated algorithms has been developed using the ID and the IV to reconstruct the tracks of such muons. The ID algorithm relies on the Cherenkov-like light cone emitted by the muons crossing the scintillator. The IV algorithm is based on a log-likelihood minimisation using the photon arrival time patterns determined from MC simulations. The spatial information provided by the OV is also included in the track reconstruction.

The lateral resolution of the reconstructed track is determined at the detector center, using MC simulations, to be about 35 cm for the ID and 60 cm for the IV.

3.8.4 Energy reconstruction

The mixing parameter θ_{13} is inferred by the comparison between the $\bar{\nu}_e$ energy spectrum obtained with the FD and the expected spectrum from MC simulations. Uncorrected differences between the energy spectra would affect the measured of θ_{13}. The energy reconstruction is thus an important steps towards the comparison of energy spectra.

The energy scale is defined by the visible energy, E_{vis}, measured in MeV units, which provides the absolute calorimetric estimation of the energy deposited per each trigger. The visible energy is obtained from the charge reconstructed on each ID PMTs. The charge is converted into photo electrons (PE) and multiplied by factors correcting for detector uniformity and stability and finally converted in MeV:

$$E_{vis} = PE^m \times f^m_{uniformity} \times f^m_{stability} \times f^m_{MeV}. \tag{3.14}$$

where m refers to data or MC. The PE conversion is obtained from the sum of the charge per channel as:

$$PE = \Sigma_i \ \mathrm{PE}_i = \Sigma_i q_i \times gain_i(q_i) \tag{3.15}$$

The $gain_i(qi)$ is extracted for each channel from the PE distribution obtained during IDLI runs [18]. It corrects the non-linearity of the charge reconstruction around the SPE charge equivalent, as shown in Fig. 3.24. Such curve is measured per each power-cycle period and per channel.

The detector response is intrinsically non-uniform across the detector volume due to several effects of the optical model. Response map of the H-capture gamma line is then used to characterise the response variations across the full volume in the ID [88]. The response uniformity factor, $f_{uniformity}$ of

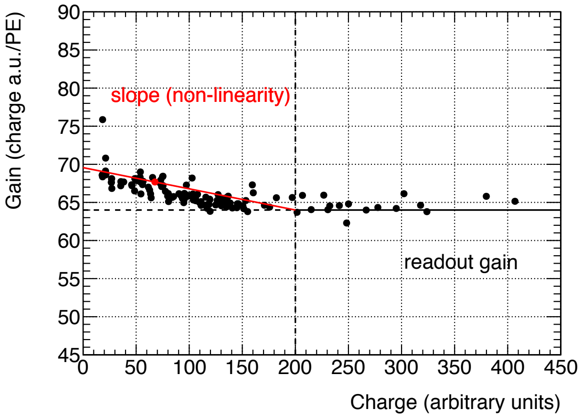

Figure 3.24: Linear PE calibration for one channel. The dashed line shows the constant component of the gain in the multi-PE charge equivalent region (> 200 a.u.). The calibration utilises a linear approximation in the SPE charge equivalent region (< 200 a.u.) to describe non-linearity. at low charges.

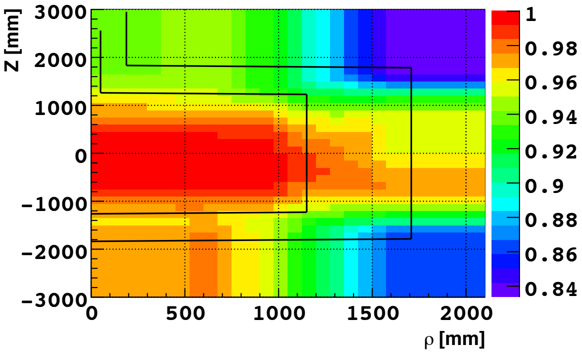

Figure 3.25: Detector calibration map as sampled with spallation neutrons captured on H across the ID. The Colour shows energy correction factors distributed as a function of reconstructed vertex. A similar map is constructed to calibrate the MC energy.

Eq. 3.14, convert the response of any energy deposition in PE to its equivalent at the detector center (ρ=0,z=0). Detector response map obtained at H capture gamma line is shown in Fig. 3.25. The map is obtained from a sample of spallation neutron (after muon interacting in the detector) and neutrinos, respectively for data and MC.

Systematic uncertainties are estimated from the data/MC discrepancy of the map obtained at Gd-capture line. Like the map used for the energy reconstruction, Gd-capture response map is obtained from spallation-neutrons and neutrinos, respectively for data and MC. The relative difference across the Target volume is measured to be 0.43 %.

The response stability factor, $f_{stability}$ of Eq. 3.14, take into account variation of the detector response due to drift arising from variations in readout gain and variation of number of channels used to compute the total deposited charge. Relative variation of the detector response is shown in Fig. 3.26. Systematic uncertainties from remaining instability are estimated to be 0.61 % from the relative stability of the H-capture peak, obtained from spallation neutron over the entire data taking [42].

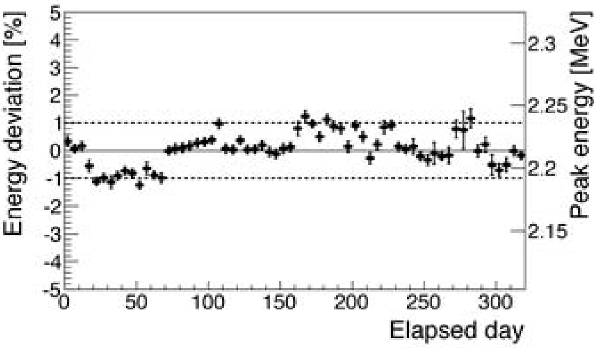

Figure 3.26: Stability of the reconstructed energy as obtained from the spallation neutron H-capture peak, over the entire data taking. The observed steps correspond to power-cycle periods.

Finally the last stage of calibration provide the absolute MeV scale to both data and MC. The MeV scale is defined by the position of the 2.2 MeV n-H capture peak. Conversion factor of about 230 PE/MeV is obtained using neutron from ^{252}Cf calibration source deployed in the center of the detector. The conversion factor is measured both for data and MC as shown in Fig. 3.27. The MeV calibration was measured on 18th August 2011 when the ^{252}Cf was deployed. This moment in time is defined as t_0 reference time for the stability calibration since the response changes before and after.

Some data/MC discrepancies in the absolute energy scale can arise from the relative non-linearity across the prompt energy spectrum range, since

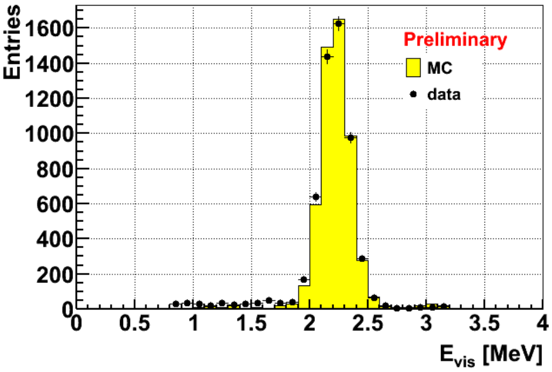

Figure 3.27: Data and MC 2.2 MeV n-H capture peak as obtained from ^{252}Cf calibration source deployed in the center of the detector. The peak position is defined as the energy conversion factor, corresponding to 230 PE/MeV.

the responses are equalised at 2.2 MeV. Such discrepancies were explored by using all calibration sources in the energy range $[0.7, 8]$ MeV deployed along the z-axis and guide tube. A 0.85 % variation consistent with this non-linearity was measured with the z-axis calibration system, and used as the systematic error for relative non-linearity. Consistent results were obtained when sampling with the same sources along the GT.

The systematic uncertainties related to the energy scale are summarised in Tab. 3.3. Upon calibration, the remaining difference in response between data and MC is of 0.3 % [42].

	Error [%]
Relative non-uniformity	0.43
Relative instability	0.61
Relative non-linearity	0.85
Total	1.13

Table 3.3: Contribution to the systematic uncertainty related to the energy scale.

3.9 Conclusions

The DC detector design, the electronics and the online system has been described with details highlighting the major improvements with respect the previous CHOOZ experiment. The FD was build between 2009 and 2010 and is taking regular data since April 2011. The near laboratory hall construction will finish by the end of 2012 and the ND is expected to start data taking by the end of 2013.

Since the ND is not ready, the simulation of the reactor $\bar{\nu}_e$ flux is required to perform the oscillation analysis discussed in the next chapter. The simulation of the expected $\bar{\nu}_e$ flux introduce a systematic uncertainty of 1.8 %. However, such uncertainty together with other detector related systematics, are expected to be suppressed below 1 % once the ND will start the data taking and the relative comparison between near and far detector will be performed to measure the value of θ_{13}.

Chapter 4

Measurement of θ_{13} with the Double Chooz far detector

This chapter presents a description of the oscillation analysis performed by Double Chooz to measure θ_{13}. The analysed data sample consists of the data taken from 13th April 2011 to 30th March 2012, a total of 323 days of data taking.

The definition of the data subsample used for $\bar{\nu}_e$ searches is provided in Sec. 4.1. The $\bar{\nu}_e$ signal selection and the estimation of the backgrounds are discussed in Sec. 4.2, 4.3.1, 4.3.2 and 4.3.3. The correlated background analysis briefly described in Sec. 4.3.3 will be developed in full details in Ch. 5. In Sec 4.3.4 the results of the direct background measurement performed when both Chooz nuclear reactors were off is provided. It should be noted that the possibility to measure background with both reactors off is a unique characteristic of Double Chooz. Daya Bay and RENO are in fact exposed to the antineutrino flux coming from 6 nuclear reactors and the possibility that all reactors are switched off is remote.The description of the analysis continues with the estimation of the selection efficiencies and their systematic uncertainties in Sec. 4.4.

Finally in Sec. 4.6, the $\bar{\nu}_e$ energy spectrum measured with the FD is compared with the reactor flux simulated over the same time period, the observed spectra is then fitted to infer the value of the oscillation parameter θ_{13}. The results discussed in this chapter has been presented at Nu2012 conference [9] and published in [20].

4.1 Data sample

The data sample used for the present analysis correspond to 323 days of data taking from 13th April 2011 to 30th March 2012. The run time, defined as the amount of time the data acquisition system was actively acquiring data, is shown in Fig. 4.1 as a function of the data-taking day. The total run time

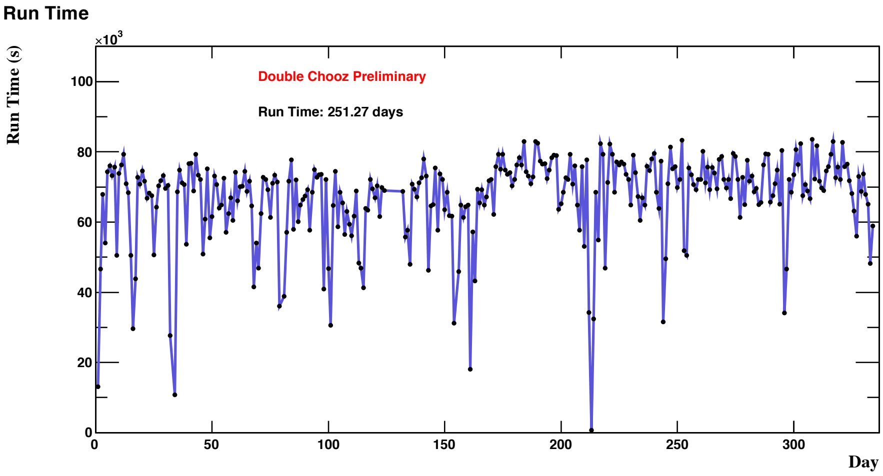

Figure 4.1: Run time in function of the data-taking day. The run time is measured for each data taking run as the difference between the run start and the run end time.

over the whole period is 251.27 days.
Every energy deposition above ID trigger threshold ($\simeq$ 0.5 MeV) or IV trigger threshold ($\simeq$ 4 MeV) are read-out and written to file. For the purpose of this analysis, a subsample of the dataset need to be defined in order to reject events not related to $\bar{\nu}_e$ (signal) or $\bar{\nu}_e$ -like (background). The events rejected are described in the following sections.

4.1.1 External trigger

The external triggered events, mentioned in Sec. 3.2.4, are rejected using the trigger words, which specify the trigger information related to a given event.

4.1.2 Instrumental noise

Scintillation light produced by point-like energy deposition in the target or in the gamma-catcher is most likely emitted uniformly across the detector. Such light is spread over many PMTs and signals are observed within a short amount of time. The PMTs installed in the ID are observed to spontaneously emit light due to electrical discharge of electronic component in the PMT base itself. Such spontaneous light emission, commonly referred as *light noise* among DC collaborators, shows a different nature with respect to physics events [34]. First of all such light is not from scintillation, so it does not present the characteristic time structure of the scintillator. Second the light noise is emitted from the base of one PMT, thus it could create a signal in the PMT itself, through reflection on the PMT mu-metal shield, or in its nearest neighbour. For such reasons light noise events are not expected to be well spread among all the PMTs and the signal time distribution will be much wider with respect to physics events. Fig. 4.2 shows the correlation between the ratio of maximum charge per PMT to total charge (measurement of the spread of the light among the PMTs) and the RMS(T_{start}) (measurement of the time spread of the PMT pulse). Light noise events are rejected requiring the ratio of maximum charge per PMT to total charge in an event is required to be less than 8 % ($Q_{max}/Q_{tot} < 0.08$) and the time spread of the PMT pulse time is required to be less than 40 ns (RMS(T_{start})$<$ 40 ns) [34]. The signal selection efficiencies are evaluated using $\bar{\nu}_e$ MC simulation to be 100 %.

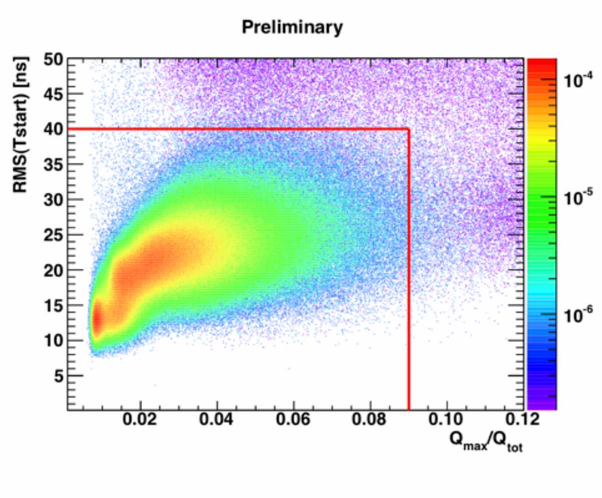

Figure 4.2: Correlation between the measurement of the time spread of the PMT pulses, RMS(T_{start}), and the measurement of the light spread among the PMTs, Q_{max}/Q_{tot}. Physics events are selected within the red box, where a well spread light among the PMTs, PMT maximum charge below 8 % of the total charge, and a short time pulse spread, below 40 ns, is found. Light noise is represented by events outside the red box, where both the time and light spread become worse and the correlation among the two variable is lost.

4.1.3 Muon correlated events

The correlated physics generated by muon crossing the detector is rejected by a veto time upon a tagged muon. Muon are tagged in the reconstruction process by requiring the charge deposited in the IV to be bigger than 10^4 DUQ or the energy deposited in the ID to be bigger than 30 MeV (Sec.

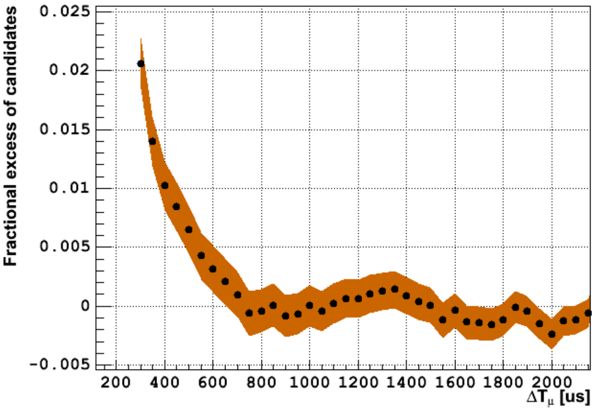

Figure 4.3: Fractional excess of IBD-like candidates with respect to the expected $\bar{\nu}_e$, as a function of the time to the last tagged-muon ($\Delta T(\mu)$). The coloured band represent 1σ uncertainty. The increase of the fractional excess of IBD-like candidate as we get closer it time to the last tagged-muon indicate the existence of correlated background. A veto time of 1000 μs from the last tagged-muon is applied to reject correlated background.

3.8.3). The fractional excess of IBD-like candidates with respect to the expected $\bar{\nu}_e$, as we get closer in time to the last tagged-muon is shown in Fig. 4.3 with 1σ uncertainty, represented by the coloured band. The increase of IBD-like candidates as $\Delta T(\mu)$ goes below 600 μs indicates the existence of correlated events satisfying the $\bar{\nu}_e$ selection as defined in Sec. 4.2. Accidental backgrounds do not contribute to this estimation. For instance, at $\Delta T(\mu)$ around 450 μs, there is 1 % increase in the correlated background leaking into the $\bar{\nu}_e$ sample. A veto time of 1000 μs is set since the increase of correlated background is negligible (less than 0.2 % at 1σ) [89].
Fig. 4.4 shows the detector live time, defined as the run time once corrected by the muon veto time, as function of the day [77]. The muon veto introduces a dead time of 4.4 % with respect to the run time, the total live time of 228.16 d is therefore the effective time devoted to the search for neutrino candidates.

4.2 $\bar{\nu}_e$ signal selection

The $\bar{\nu}_e$ searches are performed looking for time coincidence between a prompt event, defined by the IBD positron energy loss in the scintillator and its following annihilation, and a delayed event, defined by the delayed capture of the IBD neutron on Gd.
The prompt events are selected by requiring their energy to be between 0.7 MeV and 12.2 MeV. The low energy bound is defined by the lowest pos-

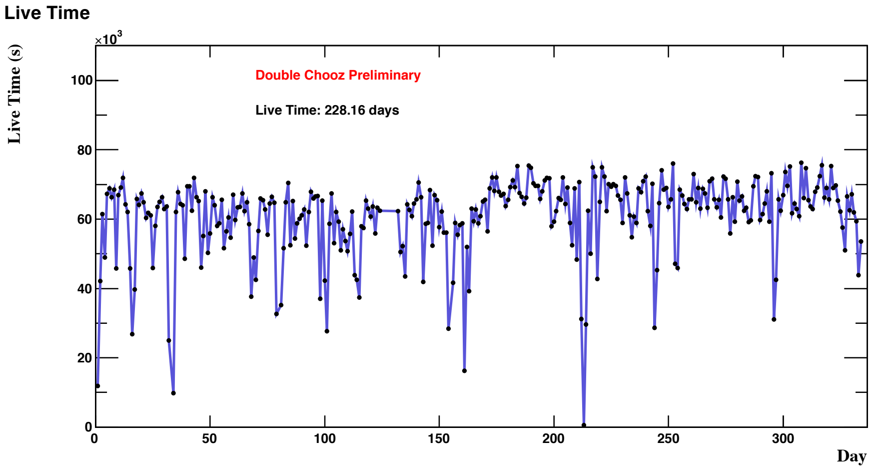

Figure 4.4: Live time in function of the data-taking day. The live time is obtained from the run time corrected by the 1000 μs muon-veto time, applied upon each tagged-muon.

sible energy where the trigger efficiency is 100 %, with negligible uncertainty (Sec. 4.4.1) while the upper bound allows to include the entire reactor-$\bar{\nu}_e$ spectrum in the selection plus some background, to enhance the background constraint in the final θ_{13} fit. The delayed event is selected requiring its energy to be between 6.0 MeV and 12.0 MeV, well containing the n-Gd capture peak.

Fig. 4.5 shows the distribution of Q_{max}/Q_{tot} for both prompt candidate (left) and delayed candidate (right). While $Q_{max}/Q_{tot} < 0.09$ appears reasonable for the prompt candidate, a more stringent cut is tolerate for the delayed candidate. The Q_{max}/Q_{tot} ratio is required to be less than 0.055 for the delayed candidate [35].

The time coincidence between prompt and delayed events is required to be within 2 μs and 100 μs. The lower cut eliminates correlated noise [34] and the upper cut is determined by the approximately 30 μs capture time on Gd.

The time and the spatial correlation between prompt and delayed candidates for data and $\bar{\nu}_e$ MC is shown in Fig. 4.6. The time correlation shows the fast neutron thermalization time, of the order of ~ 5 μs, and the slower neutron-Gd capture time, of the order of ~ 30 μs. The spatial distribution shows correlation up to ~ 1.5 m and a flat uncorrelated component above ~ 1.5 m, most likely due to accidental background contamination.

The spatial vertex of prompt and delayed candidates are distributed homogeneously within the target boundary, as shown in Fig. 4.7. The vertices are limited in the target by the presence of Gd, which implicitly define the

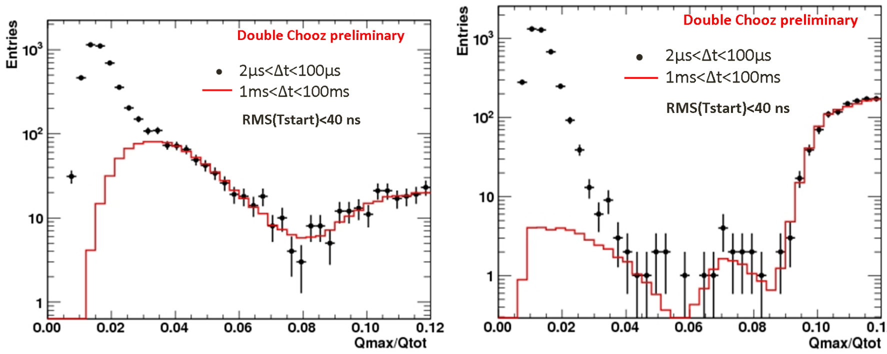

Figure 4.5: Q_{max}/Q_{tot} for prompt (left) and delayed $[6, 12]$ MeV (right) candidate. On time selection with Δt in $[2, 100]$ μs is shown with black points. Off time selection with Δt in $[1, 100]$ ms (rescaled to on time window width) is shown with red histogram.

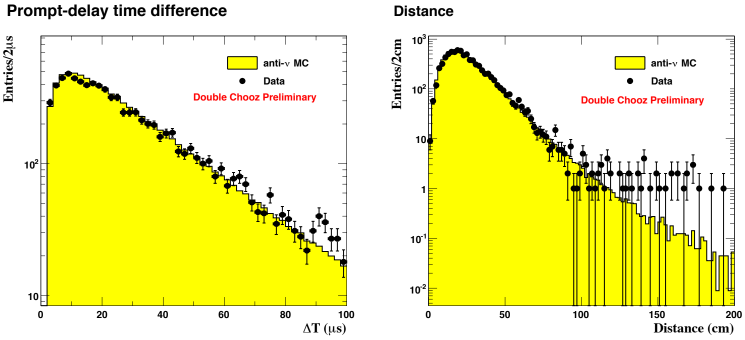

Figure 4.6: Time (left) and spatial (right) correlation between prompt and delayed events. Both data (black points) and $\bar{\nu}_e$ MC (yellow histograms) are shown. The time correlation shows the fast neutron thermalization time, of the order of ~ 5 μs, and the slower neutron-Gd capture time, of the order of ~ 30 μs. The spatial distribution shows correlation up to ~ 1.5 m and a flat uncorrelated component above ~ 1.5 m, most likely due to accidental background contamination.

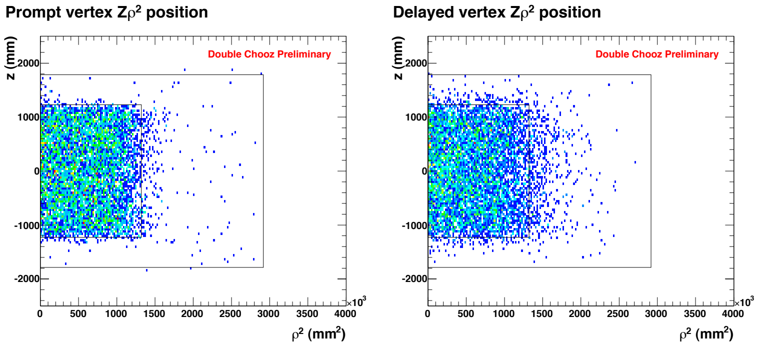

Figure 4.7: Vertex distributions for prompt (left) and delayed (right) events. The vertices are limited in the target by the presence of Gd, which implicitly define the target as the fiducial volume for $\bar{\nu}_e$ searches through neutron capture on Gd.

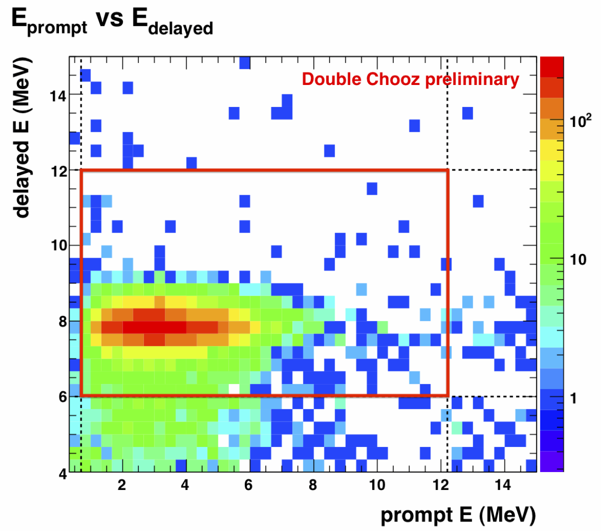

Figure 4.8: Energy correlation between prompt and delayed events. The y-axis shows the Gd-peak between $[7,9]$ MeV and its Compton edge extending to low energies. The x-axis shows the prompt spectrum between $[0.7,15]$ MeV with a maximum at about 3 MeV. The red box represent the energy region where $\bar{\nu}_e$ candidates are selected.

target as the fiducial volume for $\bar{\nu}_e$ searches through neutron capture on Gd. In order to reduce the contamination from muon correlated background and cosmogenic isotopes, further conditions are applied. A multiplicity condition to reject correlated events before (after) the prompt (delayed) is defined as no additional trigger from 100 μs preceding the prompt candidate to 400 μs after it [34]. The IBD-like events in coincidence with an OV hit are tagged as correlated background and rejected, such condition is referred as *OV veto*. The correlated background analysis described in Sec. 4.3.3, estimates a background reduction of about 28 %. The OV veto increase the dead time exposure by < 0.6 % [45]. The IBD-like events within 0.5 s from an high energy muon, defined as an energy deposition bigger than 600 MeV, are tagged as cosmogenic radioisotopes and rejected. The cosmogenic background analysis described in Sec. 4.3.2, estimates a background reduction of about 40 %. The long veto upon high energy muons introduce a dead time of 4.89 ± 1.7 %, estimated by evaluating the fraction of $\bar{\nu}_e$ candidates, over the total, found in a random 0.5 s time window [98].

The energy correlation between the prompt and the delayed events is shown in Fig. 4.8. The y-axis shows the Gd-peak between $[7, 9]$ MeV and its Compton edge extending to low energies. The x-axis shows the prompt spectrum between $[0.7, 15]$ MeV with a maximum at about 3 MeV, as expected for reactor-$\bar{\nu}_e$.

About 8249 $\bar{\nu}_e$ candidate are found for 227.93 days of detector live time, giving an averaged rate of 36.2 ± 0.4 candidates/d [77]. The $\bar{\nu}_e$ rate as a function of day is shown in Fig. 4.9 (black points) with MC expected rate (blue point). The discrepancies between data and MC are due to the background contamination, which is not subtracted.

Time periods where the $\bar{\nu}_e$ rate is lower of about 50 %, corresponds to about 87 d (~ 40 % of detector live time) where one of the two reactor cores was running at low power (< 20 %) or was not running at all. The lower points around day 190 corresponds to the 22nd October 2011, when both reactors were off for approximately 22 h.

4.2.1 Selection cuts summary

In summary, the $\bar{\nu}_e$ searches are performed applying the following selection:

No external triggers

Light noise cuts:

- $Q_{max}/Q_{tot} < 0.09$
- RMS(T_{start})$<$ 40 ns

Prompt candidate:

- E in $[0.7, 12.2]$ MeV

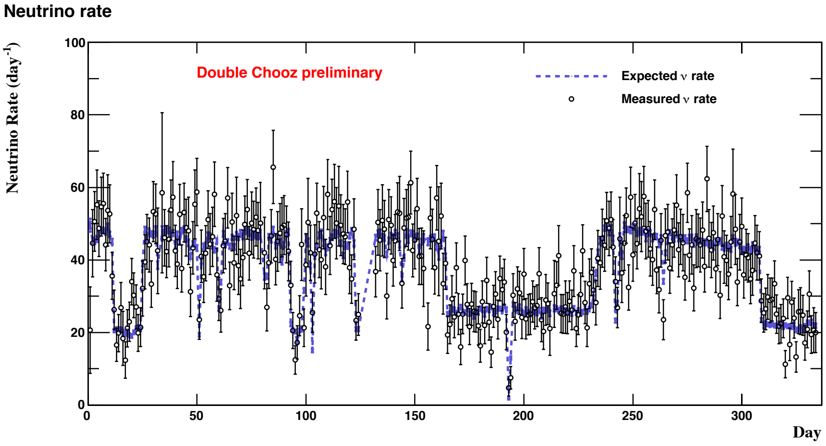

Figure 4.9: Observed (black points) and simulated (blue points) $\bar{\nu}_e$ rate in function of data taking day. The background is not subtracted from the data. The fluctuation of the $\bar{\nu}_e$ rate are due to fluctuations of the power delivered by the reactor. About 8249 $\bar{\nu}_e$ candidate are found for 227.93 days of detector live time, giving an averaged rate of 36.2 ± 0.4 candidates/d [77].

Delayed candidate:

- Delayed E in $[6; 12]$ MeV
- Delayed $Q_{max}/Q_{tot} < 0.05$

Time correlation:

- Δt in $[2; 100]$ μs

Multiplicity cuts:

- No valid triggers in the 100 μs preceding the prompt candidate
- The time window from 2 μs to 100 μs following the prompt can contain only the delayed candidate.
- No valid triggers in $[100, 400]$ μs after the prompt candidate

Reduce muon-correlated events:

- Δt(μ) $>$ 1000 μs after a muon ($E_{ID} > 30$ MeV or $Q_{ID} > 10^4$ DUQ)
- No coincidence with Outer Veto hit

Reduce cosmogenic radioisotopes:

- $\Delta t(\mu) > 0.5$ s after showering muon ($E > 600$ MeV)

4.3 Backgrounds

Three sources of backgrounds with the same prompt-delayed signal signature are identified: accidentals, cosmogenic radioisotopes and muon-correlated background. Three dedicated analysis has been performed to measure the background rates and the spectral shapes and are accounted in the final fit.

4.3.1 Accidental background

The accidental background is due to random coincidences between prompt-like and neutron-like event. Below ~ 3 MeV the prompt-like events are dominated by natural radioactivity gammas, whose spectrum ends with the ^{208}Tl line at ~ 2.684 MeV. Above ~ 3 MeV, the β-decay of the ^{12}B cosmogenic isotope contributes to the accidental background. The neutron-like events are dominated by thermal neutrons and proton recoils from fast neutrons.

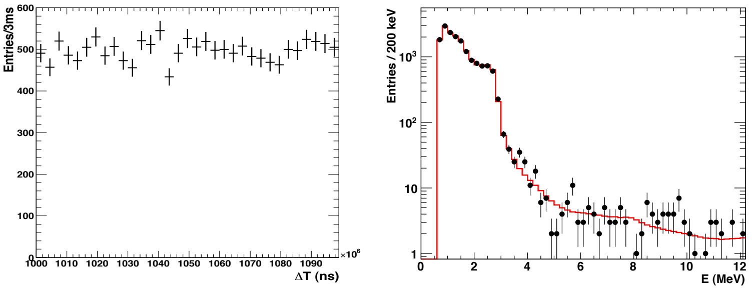

Figure 4.10: Accidental background time correlation (left) and energy spectrum (right), before (red histogram) and after (black point) time coincidences. The time correlation appears flat as expected from random coincidences. The accidental spectrum is dominated by natural radioactivity and decrease of about 2 order of magnitude above ~ 3 MeV.

The accidental background is selected performing the neutrino searches, shifting the coincidence window by 1 s from the time scale of neutron-Gd capture, in order to remove correlated events from the sample. The statistics of the sample is increased by using 198 consecutive selection windows, each shifted from the previous one by 500 μs [81]. The accidental background rate is found to be (0.261 ± 0.002) cpd[1] [81].

No systematic effect has been found moving the time window and repeating the accidental selection 30 times. The dispersion of such 30 measurements is consistent with statistical uncertainty only.

Fig. 4.10 shows the accidental background time correlation (left) and the

---

[1] Refers to *counts per day*. It is widely used in the text as unit for the background rate.

energy spectrum (right). The time correlation appears flat as expected from random coincidences. The prompt-like spectrum is dominated by natural radioactivity and decreases of about 2 order of magnitude above ~ 3 MeV. The accidental background rate is found to be stable over the considered time period, as shown in Fig. 4.11.

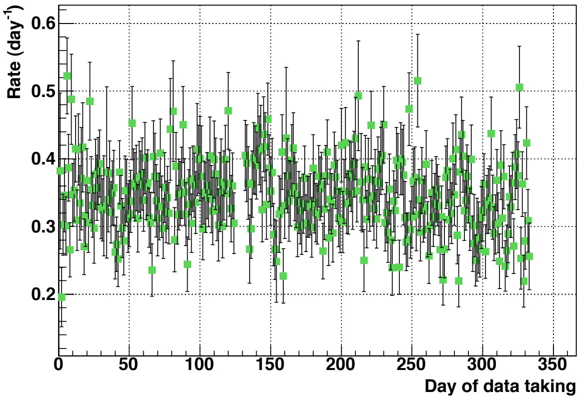

Figure 4.11: Accidental background rate as a function of the data taking day. The accidental background rate is found to be (0.261 ± 0.002) cpd and it is stable over the considered period.

4.3.2 Cosmogenic radioisotopes background

The cosmogenic radioisotopes ^{9}Li and ^{8}He are produced by cosmic muon spallation on ^{12}C in the liquid scintillator [17]. Such isotopes undergoes βn-decays with lifetimes of 257 ms for ^{9}Li and 172 ms for ^{8}He. The initial β-decay and later neutron capture produce two temporally and spatially correlated events, which can mimic the $\bar{\nu}_e$ signal. Due to the long isotope lifetime, the application of a veto time after each muon interacting in the detector would lead to an unacceptably long dead time.

The ^{9}Li rate is obtained by searching for triple fold coincidences between an $\bar{\nu}_e$ -like candidate and a suitable parent muon in a 20 s long time window ($\sim$80 ^{9}Li life time) and fitting the time distribution with an exponential and a flat components [99].

The ^{9}Li rate produced by high energy muons (E$>$ 600 MeV, muons crossing both target and gamma-catcher) is obtained directly by a fit of the Δt distribution as shown in Fig. 4.12. A precise rate of (0.95 ± 0.11) cpd is obtained.

For mid-range energy muons (E in $[257, 600]$ MeV, muons crossing gamma-catcher and a fraction of the target), the ^{9}Li rate for events near to the muon track (d $<$ 0.8 m) is obtained directly from the fit of the Δt distribution

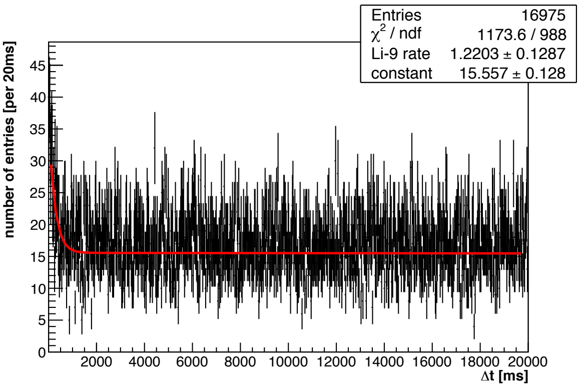

Figure 4.12: Time correlation between $\bar{\nu}_e$ -like candidates and suitable parent muon, for $E_\mu > 600$ MeV. The distribution is fit with an exponential and a flat component. The exponential component allow to estimate the ^{9}Li rate produced by high energy muon to be (0.95 ± 0.11) cpd

while the rate for events far from the muon track is extrapolated based on the lateral distance profile between muon and ^{9}Li candidate observed for high energy muons. A rate of 1.08 ± 0.36(stat) $\pm$ 0.25(syst) cpd is obtained. Lastly, the ^{9}Li rate produced by low energy muons (E< 275 MeV, muons crossing the buffer and fraction of the gamma-catcher) is estimated from the fit of the Δt distribution and it is found compatible with zero. An upper limit of < 0.3 cpd is established by the fit of the Δt distribution for events near the muon track ($d < 0.8$ m).

Finally, studies have been conducted to estimate the systematic uncertainties coming from the inclination of the flat background of random coincidences in the Δt fit and the necessity to accommodate a small fraction (10 ± 10) % of ^{8}He in the selected ^{9}Li data sample [17].

Combining the results obtained from the three muon energy ranges and accounting for the systematic uncertainties of the fitting method, the total ^{9}Li rate is $2.05^{+0.62}_{-0.52}$(stat) $\pm$ 0.26(syst) cpd [99].

High energy muons with E > 600 MeV shower into the detector, they are been found as the most likely the parents of ^{9}Li isotopes. For this reason the 0.5 ms veto is applied to the $\bar{\nu}_e$ selection, after a showering muon of energy above 600 MeV. The definition of parent muon and the veto condition were varied to obtain the maximum veto efficiency for a fixed dead exposures of ~5 %. The reduced ^{9}Li background rate is 1.25 ± 0.54 cpd [98].

Fig. 4.13 shows the ^{9}Li spectrum, obtained by selecting a purer sample of ^{9}Li events subtracting the $\bar{\nu}_e$ background through off-time selection. The obtained spectrum is then compared with MC simulation of the possible ^{9}Li decay branches [56]. The χ^2 test performed between data and MC spectra

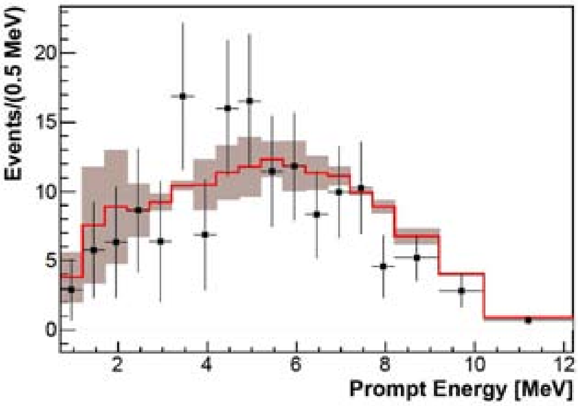

Figure 4.13: The ^{9}Li spectrum from data (black point) and MC (red histogram). The spectrum is obtained by selecting a purer sample of events subtracting backgrounds. The MC spectrum is obtained simulating the possible ^{9}Li decay branches.

gives an excellent agreements with a $\chi^2 = 16.8$ for 18 bins and a probability of about 50 % [100].

4.3.3 Correlated background

Two correlated background contributions were identified, Fast Neutrons (FN) and Stopping Muons (SM) [68]. FN are created by muons interacting in the rock surrounding the detector. Their large interaction length allows them to cross over the full detector. Some of them happen to be slowed down in the scintillator, and eventually be captured in the target. The recoil proton can mimic the positron and the neutron capture shows temporal and spatial correlation similar to a $\bar{\nu}_e$ event. SM are created by low energy muons sneaking into the detector chimney and decay. The muon energy lost by ionization in the ID mimics the prompt event and the Michel electron upon the muon decay mimics the delayed event.
The two contributions have been separated with a cut based on the time difference between prompt and delayed events and evaluated with two dedicated analysis. Rate and spectral shape have been obtained for each component and a total correlated background rate of (0.67 ± 0.20) cpd is found. The correlated background analysis adopted for the second DC publication is described with details in Ch. 5.

4.3.4 Background summary

The background rate estimations obtained in the previous sections are summarised in Tab. 4.1.

Background source	Rate [cpd]
Accidental	0.261 ± 0.002
Cosmogenic	1.25 ± 0.54
Correlated	0.67 ± 0.20
Total	2.2 ± 0.6

Table 4.1: Background rate summary

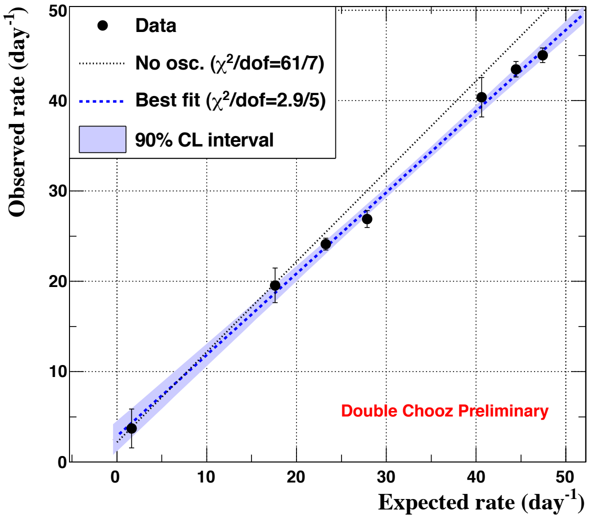

Figure 4.14: Observed $\bar{\nu}_e$ rate as a function of the non-oscillated expected rate. The dashed line show the fit to the data, the dotted line shows the expectation in case of null-oscillation hypothesis. The extrapolation to zero reactor power, i.e zero expected rate, of the fit to the data point provide a background measurement of 2.9 ± 1.1 event per day.

The total background rate is cross-checked by an independent measurement performed comparing the observed and the expected rates a function of the reactor thermal power. The measured $\bar{\nu}_e$ rate is shown in Fig. 4.14 as a function of the non-oscillated expected rate, for different reactor power condition. The extrapolation to zero reactor power, i.e zero expected rate, of the fit to the data point provide an estimation of the background contamination of 2.9 ± 1.1 cpd, in excellent agreement with background estimation.

A further independent measurement of the background is performed by analysing 22.5 h of reactor off-off data. The expected $\bar{\nu}_e$ signal is < 0.3 % events while 3 IBD-like candidate are observed. Two events have the prompt energy of 4.8 MeV and 9.4 MeV and are associated within 30 cm and 240 ms to the closest energetic muon, and are thus likely associated with cosmogenic background. The third candidate has a prompt energy of 0.8 MeV and a spatial distance of 3.5 m from the associated delayed event and is therefore likely to be an accidental coincidence.

About 7 days of reactor off-off data, taken immediately after the dataset used in this work, are currently being analysed and will be the subject of a dedicated paper.

4.4 Selection efficiencies and systematics

Since the current phase of the experiment involve the FD only, the efficiencies related to the data selection are naturally taken into account comparing data with MC expectation, performing an identical selection on the MC. Important quantities are the remaining discrepancies between data and MC that need to be assumed as systematic uncertainties. In the following sections a description of the relevant selection efficiency and related systematics is provided. The values are summarised in Tab. 4.2.

4.4.1 Trigger efficiency

The trigger efficiency is evaluated analysing the FEE stretcher pulse amplitude (Sec. 3.2.2) at the trigger release time for events triggered independently by pre-scaled trigger [92]. The stretcher pulse amplitude is then converted into energy using the correlation map shown in Fig. 4.15.

The trigger efficiency curve obtained with this method is shown is Fig. 4.16. Uncertainty on the trigger efficiency comes mainly from statistical fluctuation, definition of trigger release time, energy conversion and from the method itself. Systematics uncertainty due to the method has been taken into account evaluating the discrepancies on the trigger efficiency obtained with events triggered independently by the IV and by the two trigger boards separately. The breakdown of systematic uncertainty is shown if Fig. 4.17. The trigger efficiency is of about 50 % at 0.4 MeV and $100.0^{0.0}_{0.1}$ % at 0.7 MeV (prompt lower cut). Above 0.8 MeV the trigger efficiency is 100.0 ± 0.0 % [93].

4.4.2 Neutron detection efficiency

The most significant source of inefficiency is the one related to the neutrino detection, i.e. the delayed events. The efficiency related to the identification

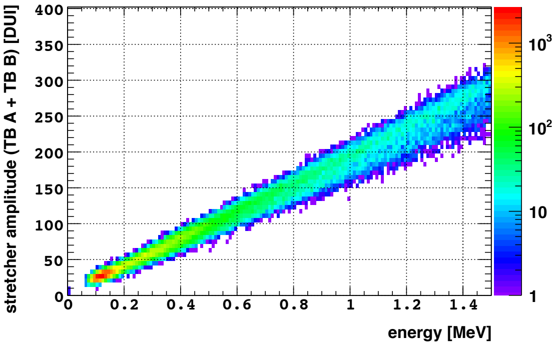

Figure 4.15: Correlation between the amplitude stretcher pulse produced by the FEE and energy deposited in the detector.

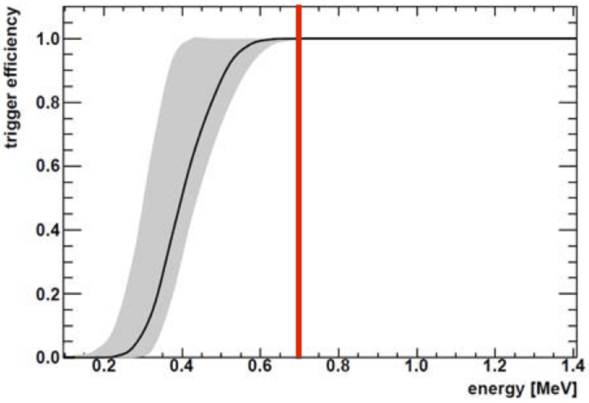

Figure 4.16: Trigger efficiency as function of energy. The trigger efficiency is of about 50 % at 0.4 MeV and $100.0^{0.0}_{0.1}$ % at 0.7 MeV (prompt lower cut). Above 0.8 MeV the trigger efficiency is 100.0 ± 0.0 %.

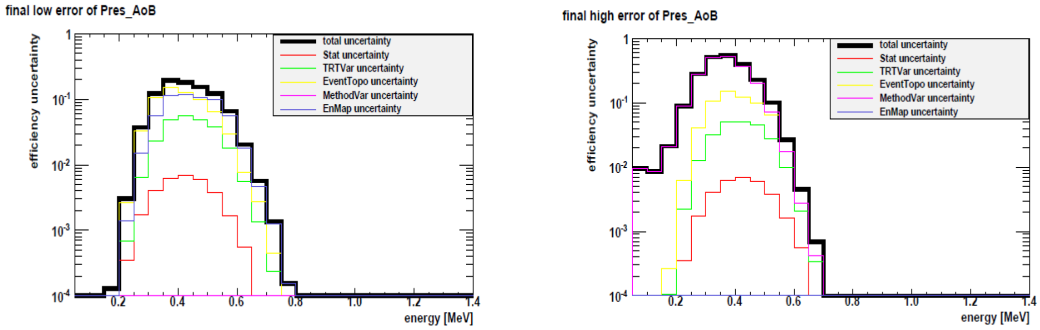

Figure 4.17: Trigger efficiency uncertainty breakdown. Uncertainty on the trigger efficiency comes mainly from statistical fluctuation, definition of trigger release time, energy conversion and from the method itself.

of the delayed events coincides with the neutron detection efficiency and it could be factorized in three terms [90]:

$$\epsilon_n = \epsilon_{Gd} \times \epsilon_{\Delta t} \times \epsilon_{\Delta E} \tag{4.1}$$

where ϵ_{Gd} is the fraction of neutron captures on Gd, $\epsilon_{\Delta t}$ is the fraction of neutron captures within the coincidence window of $[2, 100]$ μs, and $\epsilon_{\Delta E}$ is the fraction of Gd captures in the energy range in $[6, 12]$ MeV. All the three terms are evaluated comparing data and MC for ^{252}Cf calibration source deployed along the detector z-axis and in the guide tube.

Fraction of neutron captures on Gd: ϵ_{Gd}

The quantity is calculated as:

$$\epsilon_{Gd} = \frac{N(Gd)}{N(Gd) + N(H)} \tag{4.2}$$

where $N(Gd)$ is total number of neutron captures on gadolinium, and $N(H)$ is total number of neutron captures on hydrogen. The ^{252}Cf neutron energy spectrum is shown for data and MC in Fig. 4.18 (left). The number of neutron captured by H and Gd is obtained by fitting to the energy spectrum for both data and MC as shown in Fig. 4.18 (right). The H peak is fitted with gaussian plus exponential function to account for natural radioactivity background. The Gd peak is fitted with two gaussian functions to account for the neutron capture on the two main Gd isotopes plus an error function to account for the Compton edge [47]. Due to the ^{252}Cf neutron multiplicity (3.869 ± 0.078 neutrons per fission [53]), peaks for the simultaneous captures of two neutrons on Gd and H ($\sim$ 10 MeV) and two captures on Gd ($\sim$ 16 MeV) are also seen.

The fraction of neutron capture on Gd is found to be 0.8658 ± 0.0015 for data and 0.8798 ± 0.0007 for MC. The ratio of those quantity is 0.9842 and is used as MC correction factor, to account for discrepancy between data and MC. The variation of the selection criteria on the MC reproduces the value estimated on the data within 0.30 %, which is thus assumed as systematic uncertainty [54].

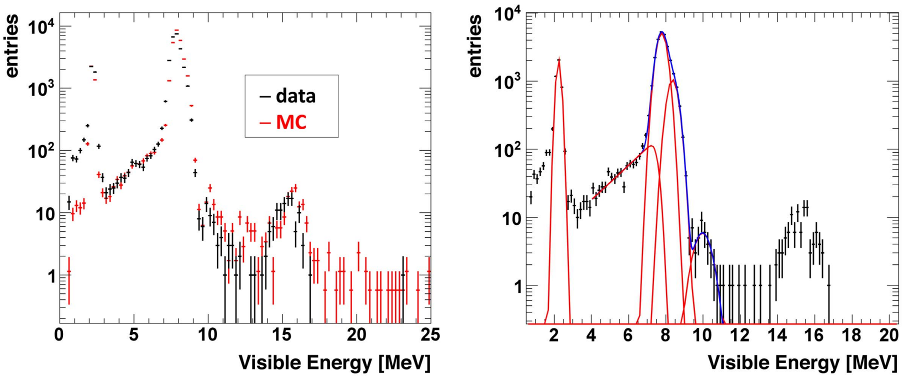

Figure 4.18: ^{252}Cf neutron energy spectrum for data and MC (left). Spectral fit function, used to estimate the fraction on neutron captured on Gd (right). Due to the ^{252}Cf neutron multiplicity (3.869 ± 0.078 neutrons per fission [53]), peaks for the simultaneous captures of two neutrons on Gd and H ($\sim$ 10 MeV) and two captures on Gd ($\sim$ 16 MeV) are also seen.

Time cut efficiency: $\epsilon_{\Delta t}$

The Δt cut efficiency represents the fraction of neutron captures within the $[2, 100]$ μs time window. The efficiency is calculated as a ratio between the events in $[2, 100]$ μs and the events in $[0, 200]$ μs as function of the ^{252}Cf source position along the z-axis and the guide tube as shown in Fig. 4.19 and 4.20 (left). The overall efficiency, averaged over the detector volume, is found to be 96.2 %. The uncertainty are estimated from the discrepancies between data and MC simulation, preformed with a custom Geant4 code to properly account for the low energy neutron physics. Standard Geant4 MC, in fact, assumes neutron capture on free-H, when it is known the H is in a molecular bound state. The effect is a shorter live time than the observed ones. The data are found in good agreement with MC as shown in Fig. 4.21, resulting in a systematic uncertainty of 0.50 % [54]. Data/MC discrepancies are shown in Fig. 4.19 and 4.20 (right) as a function of the source position.

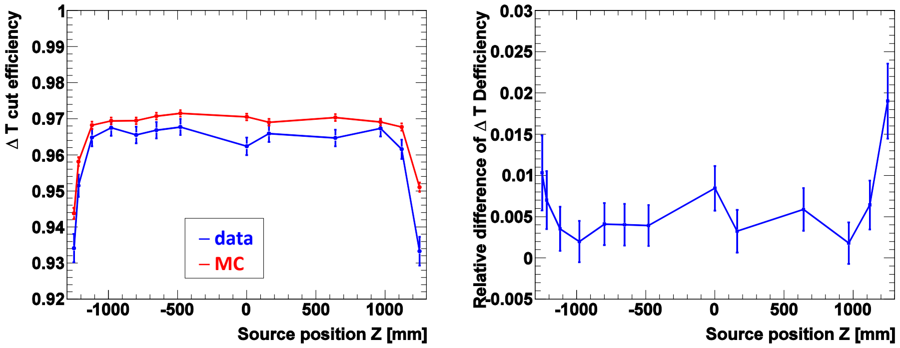

Figure 4.19: Δt cut efficiency (left) and data/MC discrepancy (right) as a function of the ^{252}Cf source position along the z-axis.

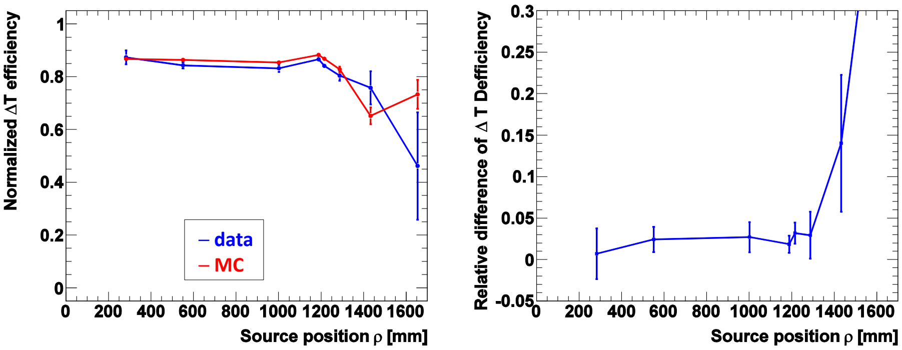

Figure 4.20: Δt cut efficiency (left) and data/MC discrepancy (right) as a function of the ^{252}Cf source radial position along guide tube.

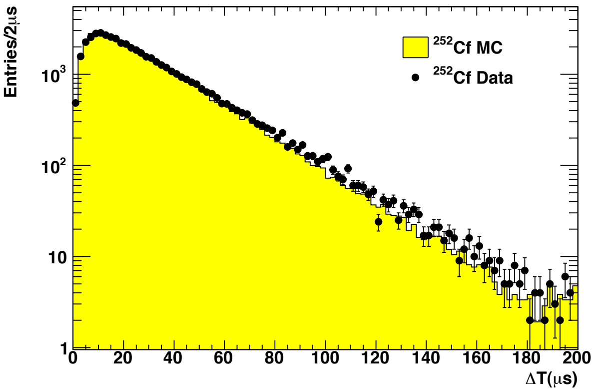

Figure 4.21: Δt cut efficiency extrapolation from the detector center to the edges.

Energy containment efficiency: $\epsilon_{\Delta E}$

The lower bound of the delayed energy selection introduces some inefficiency if a gamma from the Gd capture escapes from the detector active volume. The efficiency due to the energy containment is evaluated to be 94.1 % by the ratio between the events selected in $[6, 12]$ MeV and the events in $[4, 12]$ MeV, with ^{252}Cf data deployed along the z-axis and guide tube. The energy containment efficiency as a function of the source position in the detector is shown in Fig. 4.22 and 4.23 (left) for z-axis and guide tube respectively.

The systematic uncertainty is estimated by the data/MC discrepancy to be 0.7 % [54]. Data/MC discrepancies are shown in Fig. 4.22 and 4.23 (right) as a function of the source position.

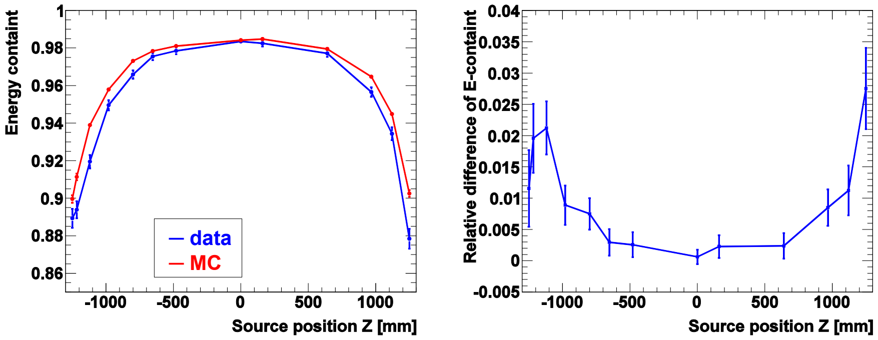

Figure 4.22: ΔE cut efficiency (left) and data/MC discrepancy (right) as a function of the ^{252}Cf source radial position along z-axis.

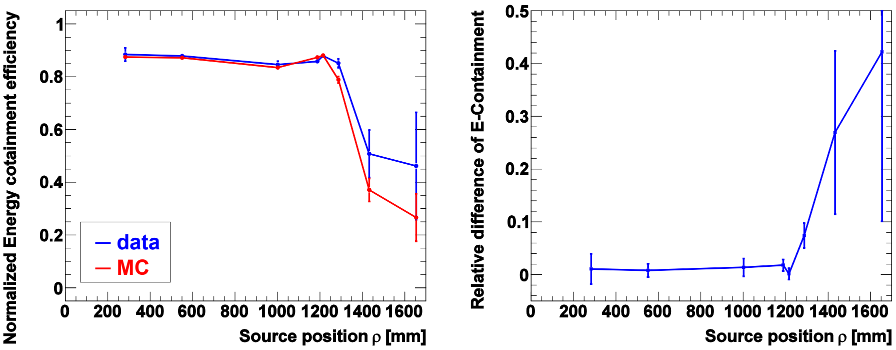

Figure 4.23: ΔE cut efficiency (left) and data/MC discrepancy (right) as a function of the ^{252}Cf source radial position along guide tube.

4.4.3 Spill-in/out

Neutrons are captured on Gd once their energy become thermal. The thermalization process happen through multiple elastic scattering between the neutron and the nuclei of the atoms of the scintillator, the characteristic time is of about 30 μs. During the thermalisation process, the neutron is diffused in the scintillator. A neutron from $\bar{\nu}_e$ IBD in the target could reach the γ-catcher volume and be captured on H. On the other hand, the neutrino could interact in the γ-catcher and the neutron be captured on Gd in the target volume. Such effects are called *spill-out* and *spill-in* respectively. Such effects have to be taken into account since they do not compensate precisely, resulting in a net spill-in current which impacts on the normalisation of the MC simulation [74].

Due to the presence of Gd in the target liquid, the mean live time of a neutron in the target volume is shorter ($\tau_{Gd} \sim 30$ μs) than the one in the γ-catcher ($\tau_H \sim 100$ μs). So the *spill-in* probability is expected to be larger than the *spill-out*. The *spill-in/out* effect is studied with $\bar{\nu}_e$ MC sample and the systematics effect due to the MC model (~ 0.22 %), the concentration of Gd in the target (~ 0.10 wt. %) and the concentration of H in the γ-catcher (negligible effect) are taken into account. Spill-in/out correction is found to be 1.35 ± 0.29(syst) $\pm\, 0.04$(stat) % [62].

4.5 Data analysis summary

Tab. 4.2 report a summary of all the necessary input parameters for the measurement of θ_{13}. The parameters obtained for the first DC publication [19] are also reported for comparison. Beyond the increased statistics due to the longer exposure time (about a factor 2), improvements on the MC modelling of the low energy neutron physics, energy scale calibration, cosmogenic background analysis and correlated background analysis allow to decrease the total systematic uncertainty from ~ 3.7 % to ~ 1.8 %.

4.6 Final fit and measurement of θ_{13}

The measurement of θ_{13} is performed by a combined fit to the $\bar{\nu}_e$ rate and spectral shape, to explicit account the spectral distortion induced by the oscillation, i.e. energy dependence of the oscillation probability.

The observed $\bar{\nu}_e$ spectral shape is compared to the expected one, as obtained by the simulation of the reactor $\bar{\nu}_e$ flux, and the spectral shape obtained from background studies. The energy interval between 0.7 MeV and 12.2 MeV has been divided in 18 non-constant bin to ensure enough statistics per bin. The expected number of signal and background events is obtained for each

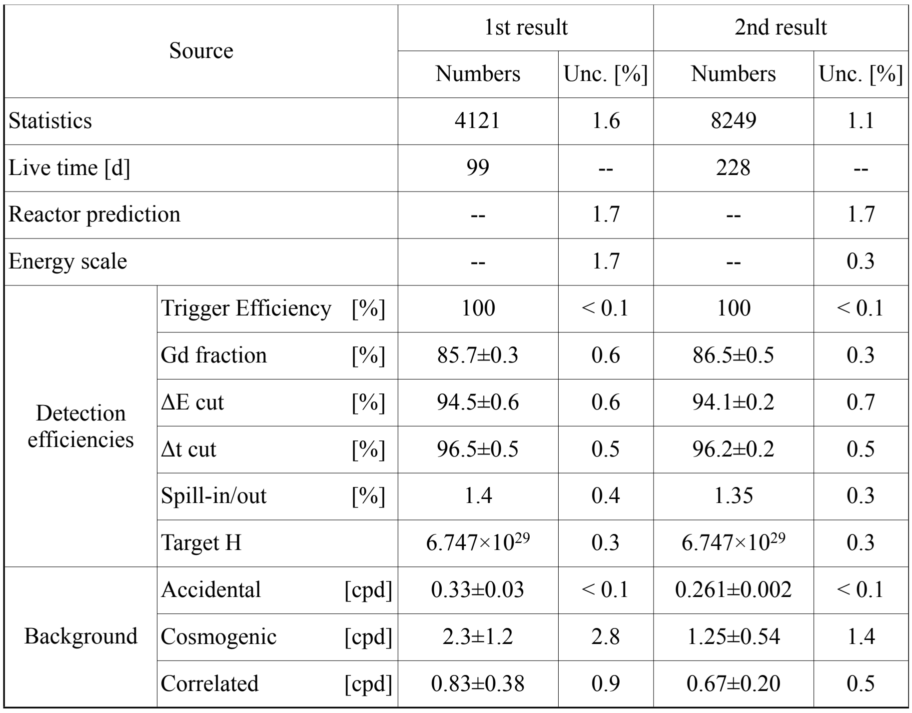

Source		1st result		2nd result	
		Numbers	Unc. [%]	Numbers	Unc. [%]
Statistics		4121	1.6	8249	1.1
Live time [d]		99	--	228	--
Reactor prediction		--	1.7	--	1.7
Energy scale		--	1.7	--	0.3
Detection efficiencies	Trigger Efficiency [%]	100	< 0.1	100	< 0.1
	Gd fraction [%]	85.7±0.3	0.6	86.5±0.5	0.3
	ΔE cut [%]	94.5±0.6	0.6	94.1±0.2	0.7
	Δt cut [%]	96.5±0.5	0.5	96.2±0.2	0.5
	Spill-in/out [%]	1.4	0.4	1.35	0.3
	Target H	6.747×10^{29}	0.3	6.747×10^{29}	0.3
Background	Accidental [cpd]	0.33±0.03	< 0.1	0.261±0.002	< 0.1
	Cosmogenic [cpd]	2.3±1.2	2.8	1.25±0.54	1.4
	Correlated [cpd]	0.83±0.38	0.9	0.67±0.20	0.5

Table 4.2: Summary table of the parameters for the measurement of θ_{13}. The parameters obtained for the first DC publication [19] are also reported for comparison.

energy bin as:

$$N_i^{exp.} = \sum_R^{\text{rxt.}} N_i^{\nu,R} + \sum_b^{\text{bkg.}} N_i^b \tag{4.3}$$

where the i runs over the 18 bins, b represents the three background contributions and R the two reactors. The oscillation hypothesis is taken into account on the expected number of $\bar{\nu}_e$ events $N_i^{\nu,R}$, by the survival probability, as a function of θ_{13}:

$$\begin{aligned} P(E,\theta_{13}) &= P_{\bar{\nu}_e\to\bar{\nu}_e}(\theta_{13},E) \\ &= \left\{1-\sin^2(2\theta_{13})\sin^2\left(\frac{1.27\times\Delta m^2_{31}\times L[m]}{E[MeV]}\right)\right\} \end{aligned}$$

Due to reactor thermal power fluctuations, the $\bar{\nu}_e$ rate changes as function of the time as show in Fig. 4.9. While the $\bar{\nu}_e$ signal changes, the background rate remains constant over the time, so the background to signal ratio (B/S) changes. The data are divided in two integration periods based on thermal power of the two reactors [59]. During the first period both reactors were above 20 % of thermal power, while during the second period the thermal power of one of the two reactors was below 20 %.

The background populations are obtained in agreement with measured rates and live time of the detector during each integration period. The B/S ratio change from ~ 4.99 % of the first period to ~ 8.95 % of the second period. The fit is performed simultaneously over the combined 36 bins of both integration period. Such technique take advantage of the different B/S ratios in each period and add information about background behaviour to the fit. Tab. 4.3 summarise observed signal, expected signal and background expectation for the two integration periods.

The statistical uncertainty and systematic effects inducing uncertainties on the expected energy spectrum are taken into account in a mixed approach. Statistical fluctuation and systematic uncertainties on the reactor simulations, the detector response and background spectral shape are directly taken into account in the χ^2 function through a covariance matrix:

$$M_{i,j} = M_{i,j}^{stat.} + M_{i,j}^{rxt.} + M_{i,j}^{det.} + \sum_b^{\text{bkg.}} M_{i,j}^{bkg.} \tag{4.4}$$

Each term represents the covariance between i-bin and j-bin due to a given uncertainty source. The normalisation uncertainty associated with each matrix is summarised in Tab. 4.2. The reactor covariance matrix account the knowledge about the predicted neutrino spectra. The cosmogenic background matrix contains contribution due to the spectral shape uncertainty, estimated with different MC event generation parameters. The correlated background matrix account for the spectral shape slope, which is allowed

	Period 1	Period 2	Total
Livetime [d]	139.27	88.66	227.93
Observed $\bar{\nu}_e$	6088	2161	8249
Expected $\bar{\nu}_e$ (R1)	2910.93	774.64	3685.57
Expected $\bar{\nu}_e$ (R2)	3422.39	1331.74	4754.13
Expected $\bar{\nu}_e$ (Total)	6333.32	2106.38	8439.7
Correlated bkg.	93.32	59.40	152.72
^9Li bkg.	174.09	110.82	284.91
Accidental bkg.	36.35	23.14	59.49
Total bkg.	303.76	193.36	497.12

Table 4.3: Summary of observed $\bar{\nu}_e$ events with corresponding expected and background prediction for the two integration periods, before the oscillation fit.

to vary from a nearly-flat spectrum, as described in Ch. 5. The accidental background matrix is included as a diagonal covariance matrix since accidental background is measured with high precision by many off-time windows. A graphical view of the covariance matrixes is shown if Fig. 4.24 where x and y axis represent energy bins and the colour scale is proportional to the matrix element.

The uncertainty on the calibration of the energy scale, the background rate and the error on the mass-split are instead accounted as pull parameters in theχ^2 function.

The pull terms related to the background are allowed to vary as a part of the fit, to scale the background rate. The accidental background rate is not allowed to vary because its initial uncertainty is precisely determined. The energy scale is allowed to vary linearly with an uncertainty of 1.13 %, obtained as systematic uncertainty on the energy scale. Since the value of the mass splitting parameter is not fitted, the related pull term places constraint on Δm^2_{13} compared with MINOS measurement $\Delta m^2_{13} = (2.32 \pm 0.12) \times 10^{-3}$ eV^2 [25]. Such pull term includes the uncertainty introduced by relating the effective mass splitting observed in a ν_μ disappearance experiment to the one relevant for reactor experiments, and the ambiguity due to the neutrino mass hierarchy.

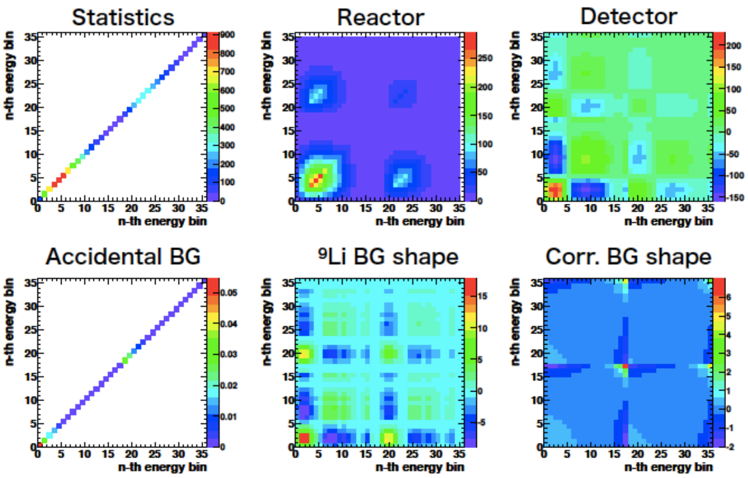
Statistics
Reactor
Detector
Accidental BG
^{9}Li BG shape
Corr. BG shape

Figure 4.24: Covariance matrixes due to statistical fluctuation and systematic uncertainties on the reactor simulations, the detector response and background spectral shape. The matrixes are drown from MC simulation.

The fit of the binned signal and background data to a two-neutrino oscillation hypothesis is performed minimising the χ^2 function:

$$\begin{aligned}\chi^2 &= \sum_{i,j}(N_i - N_i^{exp.}) \times (M_{i,j})^{-1} \times (N_j - N_i^{exp.})^T \\ &+ \frac{(\epsilon_{corr.}-1)^2}{\sigma^2_{corr.}} + \frac{(\epsilon_{cosmo.}-1)^2}{\sigma^2_{cosmo.}} \\ &+ \frac{(\epsilon_E - 1)^2}{\sigma^2_{\epsilon_E}} + \frac{\Delta m^2_{31} - (\Delta m^2_{31})_{MINOS}}{\sigma_{MINOS}} \end{aligned} \tag{4.5}$$

The best fit gives $\sin^2(2\theta_{13}) = 0.109 \pm 0.030(\text{stat.}) \pm 0.025(\text{syst.})$ at $\Delta m^2_{31} = 2.32 \times 10^{-3}$ eV^2, with $\chi^2/ndf = 42.1/35$ [20]. Fitted parameters and their uncertainties are compared with the initial values in Tab. 4.4. The background rate and related uncertainties are further constrained in the fit, as well as the energy scale.

Fit parameter	Initial value	Best fit value
Correlated bkg. $\epsilon_{corr.}$	0.62 ± 0.20 cpd	0.64 ± 0.13 cpd
Cosmogenic bkg. ϵ_{Li}	1.25 ± 0.54 cpd	1.00 ± 0.29 cpd
Energy scale ϵ_E	1.000 ± 0.011	0.986 ± 0.007
Δm^2_{31} (10^{-3} eV^2)	2.32 ± 0.12	2.32 ± 0.12

Table 4.4: Fit parameters, initial values and best fit values are compared.

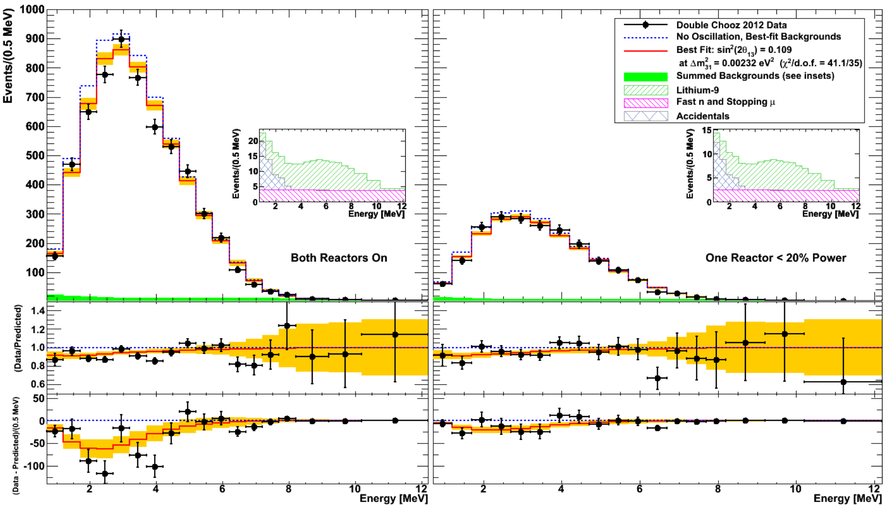

Figure 4.25: Measured prompt energy spectrum for each integration periods (black points) superimposed on the expected prompt energy spectrum, including backgrounds (green region), for the non-oscillation hypothesis (blue dotted histogram) and best fit (red solid histogram) at $\sin^2(2\theta_{13}) = 0.109 \pm 0.030(\text{stat.}) \pm 0.025(\text{syst.})$ at $\Delta m^2_{31} = 2.32 \times 10^{-3}$ eV^2, with $\chi^2/ndf = 42.1/35$ [20]. The insert shown the backgrounds in stacked histograms. The bottom part of the figure shows both the difference and the ratio between data and non-oscillation hypothesis (black points), and between best fit prediction and non-oscillation hypothesis (red solid histogram).

The measured prompt energy spectrum for the two integration periods are shown in Fig. 4.25 with the expected spectrum for the null-oscillation hypothesis, including backgrounds, and the best fit of θ_{13}.

An analysis comparing only the total observed numbers of candidate in each integration period to the expectation gives a best-fit of $\sin^2(2\theta_{13}) = 0.170 \pm 0.052$ with $\chi^2/ndf = 0.5/1$. The compatibility probability for rate+shape and rate-only analysis results is about 30 %.

The data set used for the first publication [19] has been re-processed using the current analysis techniques. The fit using a single integration period yield a best-fit value of $\sin^2(2\theta_{13}) = 0.0744 \pm 0.046$ with $\chi^2/ndf = 18.3/17$. The analysis of the data taken since the first publication yield a best-fit of $\sin^2(2\theta_{13}) = 0.143 \pm 0.042$ with $\chi^2/ndf = 9.54/17$.

A standard frequentist study, based on the Feldman and Cousin approach [57], is performed to determine the confidence intervals. This take into account the fact that the true χ^2 distributions may not be Gaussian, and is useful for calculating the probability of the null oscillation hypothesis. Frequentist study compared the data to $10,000$ simulations generated in 21 test points in the interval $0 \leqslant \sin^2(2\theta_{13}) \leqslant 0.25$. The $\Delta\chi^2$ statistics, generated from the difference between the χ^2 at the test point and the best-fit χ^2, is used to determine the $\sin^2(2\theta_{13})$ region where the $\Delta\chi^2$ is within a given confidence probability. The allowed region at 68 % (90 %) CL is $0.068(0.044) \leqslant \sin^2(2\theta_{13}) \leqslant 0.15(0.17)$. The data excludes the null oscillation hypothesis at 99.8 % corresponding to 2.9σ.

4.7 Summary and Conclusions

In this chapter the DC analysis as published in [20] has been described in full detail. With respect to the previous result [19] the data sample statistics is increased by a factor two, reducing the statistical uncertainty of about 30 %. Major improvements in the background estimations, the detector energy calibration and on the MC simulation reduced the systematic uncertainty of about 50 %. The best fit to the oscillation hypotheses performed with a rate+shape analysis, gives a value of $\sin^2(2\theta_{13}) = 0.109 \pm 0.030(\text{stat.}) \pm 0.025(\text{syst.})$ at $\Delta m^2_{31} = 2.32 \times 10^{-3}$ eV^2, with $\chi^2/ndf = 42.1/35$ and a shape consistent with θ_{13} related oscillation. The null value of θ_{13} is excluded at 99.8 % corresponding to 2.9σ. The rate+shape and the rate only analysis are found in agreement within about 30 % accuracy.

The DC results are also in agreement with recently published results from T2K [15], Daya Bay [33], RENO [31] and MINOS [23] as shown in Fig. 2.11. It should be noted the DC results is the first to incorporate the energy dependence of the neutrino oscillation.

In the next chapter the analysis performed to estimate the correlated background affecting $\bar{\nu}_e$ searches is discussed in full detail.

Chapter 5

Correlated background

With the term *correlated* is meant the background produced by muons interacting in the detector or in its surrounding, whose prompt and delayed come from the same physical process. Such background produces a prompt-like and a delayed-like events which shows similar time and spatial correlations as $\bar{\nu}_e$ signal, i.e time correlation within 100 μs and spatial correlation within few tens of cm. In addition, the time correlation with the parent muon is short, of the order of few hundreds of μs.

The correlations between prompt-like and delayed-like events distinguish the correlated background from the accidental one, due to random coincidences. The short time correlation with the parent muon differentiate the correlated background from the one produced by cosmogenic isotopes, which present longer time correlation, due to the isotopes live time of the order of few hundreds of ms.

Since muons interacting in the active volumes of the detector are tagged with high efficiency (> 99.999 %) by the IV ($Q_{IV} > 10^4$ DUQ) and the ID ($E_{ID} > 30$ MeV), correlated background produced by tagged muons is reduced < 0.2 % by applying a veto time of 1000 μs, as described in Sec. 4.1.3. However, remaining correlated background arises from muons which either missed the detector or deposit an energy low enough to escape the muon tagging. For such reason, a dedicated analysis is necessary to estimate the contribution of this remaining correlated background.

Two contributions to the correlated background have been identified so far, fast neutron (FN) and stopping muon (SM). Any indications of further contributions have not been found within the sensibility provided by the current data, but are not excluded a priori.

5.0.1 Fast Neutrons

The FN component is generated by muon spallation in the inactive regions surrounding the detector. Their large interaction length allow them to cross the detector and capture in the ID, causing a prompt event by proton recoil and a delayed event by neutron capture on Gd. Time and spatial correlations between prompt and delayed events are settle by the neutron thermalization process, therefore they are indistinguishable from those of $\bar{\nu}_e$ events. The spatial distribution is expected to be rather uniform within the target volume. The proton recoil is expected to show a rather flat spectrum, extending beyond the reactor $\bar{\nu}_e$ spectrum > 12 MeV. Scintillator quenching and acceptance effects are expected to introduce a slope, either positive or negative depending from which effect dominates. The delayed energy spectrum is due to neutron capture on Gd, therefore it is expected to be indistinguishable from the one produced by $\bar{\nu}_e$ events. In addition, a muon crossing the detector surrounding generates FN with high multiplicity along its track, then more than one FN could reach the detector and generate a trigger.

5.0.2 Stopping Muon

The SM component arise from muons entering through the detector chimney, stopping in the top of the ID and decaying. The ionization energy deposited by the muon before stopping mimics the prompt event and the decay Michel electron mimics the delayed event. The time correlation between prompt and delayed events is expected to be of the order of the muon live time, $\tau_\mu \simeq 2.2$ μs, since the Michel electron deposit quickly its energy in the scintillator. For the same reason, the spatial distance between the two events is expected to be less than few cm and to be dominated by the resolution of the vertex reconstruction algorithm (~ 15 cm). In order to escape the ID muon tagging, the muon track length in the chimney is expected to be $\lesssim 15$ cm for a minimum ionising muon, depositing ~ 2 MeV/cm. Since the muon is stopping, its ionization energy increase quadratically as the muon velocity decrease and the muon track length is expected to be shorter than a minimum ionising muon. For this reason, prompt and delayed events are then expected to be concentrated in a small region within the detector chimney. Given such acceptance conditions, the amount of SM entering through the chimney and generating correlated background is expected to be small with respect to the total amount of muons interacting in the ID. Due to the complicated acceptance condition, the prompt spectral shape is not known and must be measured experimentally. Michel electrons has a well know β energy spectrum, extending up to ~ 60 MeV. The delayed events are due to those Michel electrons depositing energy in $[6, 12]$ MeV, with a different spectral shape with respect to the Gd capture peak.

5.1 Measuring correlated background

Since both FN and SM components shows a prompt energy spectrum extending at high energy, a pure sample of correlated background can be selected requiring the prompt energy to be above ~ 12 MeV, where the $\bar{\nu}_e$ contamination is negligible, and below 30 MeV, ID muon tagging threshold. The background rate and spectral shape in the $\bar{\nu}_e$ energy region, $[0.7, 12.2]$ MeV, can be inferred by fitting the high energy sample assuming a flat spectrum and extrapolating the shape to low energy. However, the accuracy of such estimation depends on the validity of the extrapolation of the spectral shape. The selection performed at high energy allow also to study FN/SM separation based on the different correlation time distribution shown by the two background components, estimating separation efficiencies and purities. Such separation allow to study FN and SM independently.

The analysis of the high energy tail of the prompt spectrum do not allow to infer directly the shape of the correlated background at low energy. However, the low energy shape is a key ingredient for the rate and shape analysis performed to measure θ_{13}, thus precise measurements are required. Techniques based on MC simulation of the background and tagging strategy exploiting the capabilities of the DC detector are considered and discussed in the following.

5.1.1 MC technique

Dedicated MC simulation, could be performed to obtain the spectral shape at low energy. The total background rate is then obtained by scaling the MC spectrum to the data, by normalise the spectrum to the high energy tail $[12, 30]$ MeV. However, the accuracy of MC simulation are mainly limited by the modeling of scintillator quenching and acceptance effects.
The simulation of the FN prompt spectra is, in fact, sensible to the scintillator quenching affecting protons, created via elastic scattering by the neutron during its thermalization.
The accurate modeling of the chimney, which is actually a very complicated part of the detector from both geometrical and mechanical point of view, is instead required to accurately simulate acceptance effect for incoming muons generating correlated background.
Due to such complications, MC simulations of correlated background have not been considered so far. Accurate MC models are under development within the DC collaboration and will be used in future to crosscheck the current estimations.

5.1.2 Tagging techniques

Tagging techniques based on the IV and the OV are exploited to infer spectral shape for FN and SM, using a rather pure sub-sample of correlated background. The tagging efficiencies must be estimated in order to rescale the tagged shapes and obtain the total background rate. Such efficiencies can be estimated comparing tagged and un-tagged sample in the high energy tail of the prompt spectrum, assuming they would remain unchanged at low energy < 12 MeV. The estimation of the tagging efficiencies represent the main limitation of these techniques. However, IV and OV are independent detectors based on different technologies. They would provide independent estimation of correlated background which, if in agreement, would validate the assumption made on the tagging efficiency.

IV tagging

Since FN are generated with high multiplicity, some of them are expected to deposit energy in both the ID and IV. The DAQ system is designed in such a way that both ID and IV detectors are read-out whatever detector causes the trigger. In case of ID trigger, the IV detection threshold is then lowered to ~ 1 MeV, making the IV sensitive to FNs via proton recoil or captures on H. Defining a tagging condition in the IV would then allow to select a sample of FN which would provide the spectral shape in $[0.7, 12.2]$ MeV energy region.

Given the small angular acceptance by which the SM enter the ID through the chimney, IV is expected to tag SM with smaller efficiency. A different technique to infer the SM spectral shape is to take advantage of the Michel electron spectra, which extend up to ~ 60 MeV, and it is uncorrelated from the energy deposited by its parent muon. A pure sample of SM could then be obtained selecting the delayed Michel electron at high energy, > 20 MeV. In this energy region, $\bar{\nu}_e$ and FN contaminations are expected to be negligible, since their delayed events deposit energy by Gd capture between 6 MeV and 12 MeV.

OV tagging

The OV is a suitable detector to identify correlated background by tagging the parent muon. The tagging is performed by time coincidences between an OV hit and the prompt-like energy deposition in the ID.

The SM component is expected to be tagged with high efficiency since the muon enter in the detector through the chimney which is surrounded by OV scintillator strips. A smaller tagging efficiency is expected for FN since the parent muon could interact far from the detector and miss the OV.

Pulse shape discrimination

A pulse shape discrimination (PSD) technique is also been investigated to perform event tagging. PSD is expected to tag FNs via the different scintillation shape produced by the recoil protons, with respect to electrons and positrons. The distribution of the time of each pulse in each event is compared to a reference distribution, obtained with ^{137}Cs calibration source, in a likelihood approach. Despite the DC liquid scintillator has not been optimised for PSD, preliminary results are promising [73]. More studies are expected in the future.

Analysis based on the extrapolation of high energy tail and both IV and OV tagging have been performed for the second DC publication. Those different approaches are found to provide compatible results and will be described in the following sections.

5.2 High energy analysis

Correlated background sample is performed using the $\bar{\nu}_e$ selection cut summarised in Sec. 4.2.1, extending prompt energy cut from 12 MeV to 30 MeV. Since reactor $\bar{\nu}_e$ spectrum ends at about 12 MeV, above such energy a pure sample of correlated background is obtained.
The prompt and delayed vertex distributions are shown in Fig. 5.1. The black points represent events in $[0.7, 30]$ MeV, including $\bar{\nu}_e$ candidates, while red points shown the vertex distribution of the correlated background sample, with prompt energy in $[12, 30]$ MeV. The events uniformly distributed among the detector are expected to be dominated by FN while the excess of events below the detector chimney are expected to be more likely due to SM. Since the reconstruction algorithm has been designed to reconstruct events within the buffer volume, interaction vertices in the chimney are artificially pushed down toward the detector center. The true SM vertex distribution is then expected to be slightly above the observed one. The definition of a fiducial volume to separate FN from SM would then introduce systematic uncertainty related to the vertex reconstruction algorithm. In order to avoid such systematic uncertainty no fiducial volume is defined.
The prompt spectrum in $[0.7, 30]$ MeV is shown in Fig. 5.2. The correlated background spectrum shows a rather flat distribution for energies > 12 MeV, while its spectral shape in the low energy region could not be inferred since the $\bar{\nu}_e$ are dominant. A linear fit in the high energy region, $[12, 30]$ MeV, provides a rather flat spectrum with small negative slope of $(-0.08 \pm 0.04)/(0.25\ \text{MeV})^2$. The extrapolation of the linear fit to the low energy region provide a first estimation of the correlated background rate of (0.75 ± 0.12) cpd.
The same method has been adopted by Daya Bay [33] and RENO [31], but as already mentioned, the accuracy of this estimation depends on the validity of the extrapolation of the spectral shape.
In order to evaluate FN and SM background independently with dedicated analysis, the two component have to be separated. Since FN and SM present different time correlation between prompt and delayed events, a pure and unbiased sample of each component is obtained by a cut on the Δt between

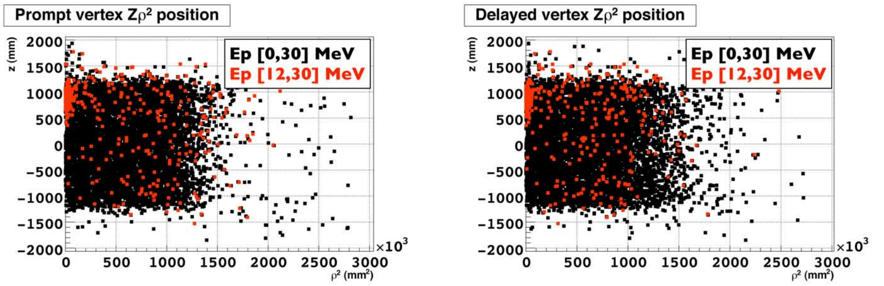

Figure 5.1: Vertex distribution for prompt events (left) and delayed events (right) selected in $[0, 30]$ MeV. A pure sample of correlated background selected in $[12, 30]$ MeV is shown with red points. The events uniformly distributed among the detector are expected to be dominated by FN while the excess of events below the detector chimney are expected to be more likely due to SM.

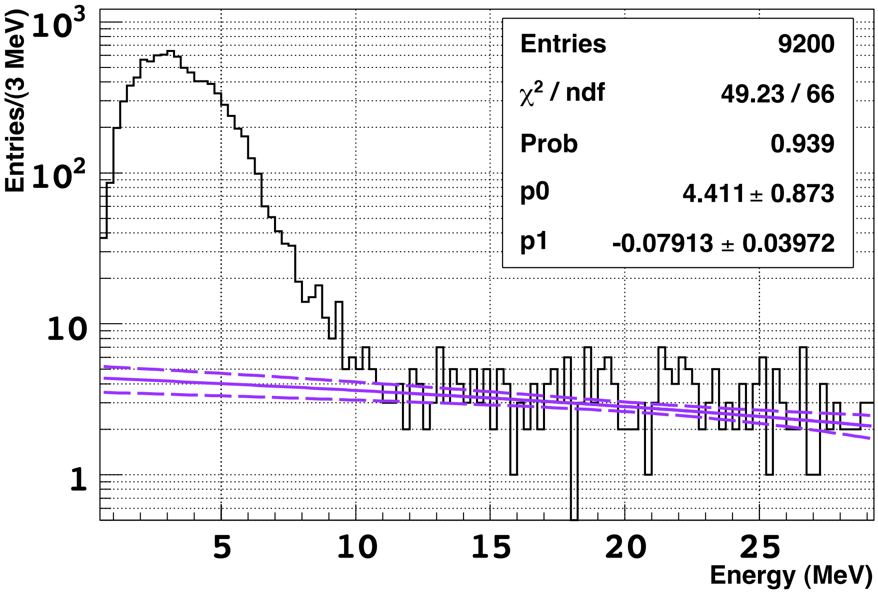

Figure 5.2: Prompt energy spectrum in $[0, 30]$ MeV (black histogram) and correlated background spectral shape with 1σ uncertainty (violet solid and dashed lines). The spectral shape is obtained by a linear fit in the high energy region. A rather flat spectrum, with small negative slope of $(-0.08 \pm 0.04)/(0.25\ \text{MeV})$ is found. The extrapolation of the linear fit to the low energy region provide a first estimation of the correlated background rate of (0.75 ± 0.12) cpd.

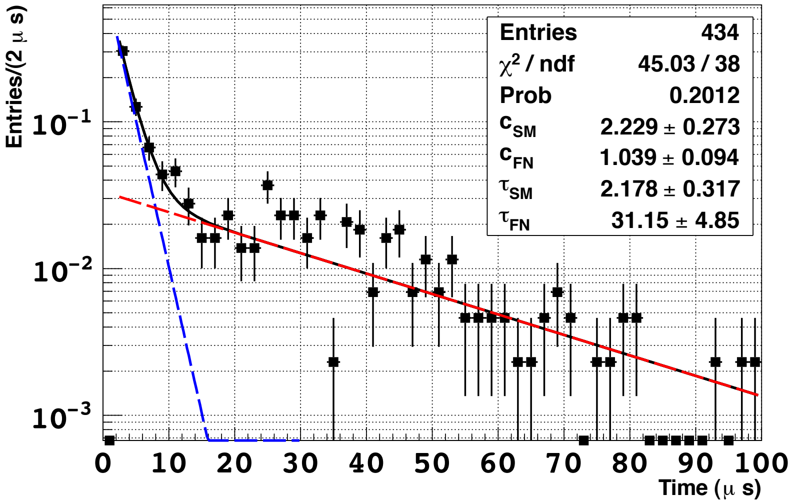

Figure 5.3: Time correlation between prompt and delayed events with prompt in [12, 30] MeV. The histogram is fitted by a two exponential model in order to describe the short time correlation, $\tau \sim 2.2$ μs, due to SM (blue dashed line) and the longer time correlation, $\tau \sim 30$ μs, due to FN (red dashed line). FN and SM components are separated by imposing a cut on the time correlation. The cut efficiency and purity for each component are estimated using the exponential model.

prompt and delayed. The time correlation obtained from the pure sample of correlated background selected in $[12, 30]$ MeV is shown in Fig. 5.3, where the expected fast and slow components, respectively due to SM and FN, appear evident. The SM time correlation has an exponential distribution, proportional to the muon live time of $\tau_\mu \simeq 2.2$ μs. The FN time correlation is driven by the neutron capture on Gd, exactly like the prompt-delayed time correlation of $\bar{\nu}_e$ candidates shown in Fig. 4.6 (left), with an increasing components at short Δt, due to the neutron thermalization process, and a decreasing component with a time constant $\tau_{Gd} \simeq 30$ μs, due to the neutron capture on Gd. The increasing component of the FN distribution is not evident since the lower part of the Δt distribution is dominated by SM.
The efficiency and the purity of the FN/SM separation by the Δt cut are estimated by approximating the time distribution with two exponential terms, as shown in Eq. 5.1:

$$f(t) = f_{SM}(t) + f_{FN}(t) = c_{SM}\left(\frac{e^{-t/\tau_{SM}}}{\tau_{SM}}\right) + c_{FN}\left(\frac{e^{-t/\tau_{FN}}}{\tau_{FN}}\right) \tag{5.1}$$

Such approximation neglect the neutron thermalization process at short Δt, which require a third positive exponential as shown in [64]. This approximation is necessary since the low statistics of the pure correlated background sample do not allow to obtain good fit result with a third exponential term in Eq. 5.1. Since the shape of the time distribution of neutron capture on Gd is well known from MC, $\bar{\nu}_e$ candidates and ^{252}Cf source, it is possible to correct for such approximation. The model fitted to the data is shown by the black curve in Fig. 5.3, while the red and the blue dashed curves represent the FN and the SM component respectively. Defining t_{cut} as the cut value, the FN sample is defined such as $t > t_{cut}$ while the SM sample is defined such as $t < t_{cut}$. Efficiency (ϵ) and purity (ρ) for both samples are computed using Eq. 5.1:

$$\epsilon_{FN}(t > t_{cut}) = \frac{\int_{t_{cut}}^{\infty} f_{FN}(t)dt}{\int_0^{\infty} f_{FN}(t)dt} \tag{5.2}$$

$$\rho_{FN}(t > t_{cut}) = \frac{\int_{t_{cut}}^{\infty} f_{SM}(t)dt}{\int_{t_{cut}}^{\infty} f_{SM} + f_{FN}(t)dt} \tag{5.3}$$

$$\epsilon_{SM}(t < t_{cut}) = \frac{\int_0^{t_{cut}} f_{SM}(t)dt}{\int_0^{\infty} f_{SM}(t)dt} \tag{5.4}$$

$$\rho_{SM}(t < t_{cut}) = \frac{\int_0^{t_{cut}} f_{SM}(t)dt}{\int_0^{t_{cut}} f_{SM} + f_{FN}(t)dt} \tag{5.5}$$

The t_{cut} value is chosen to be 10 μs ($\sim 4.5 \times \tau_{SM}$) as to obtain $\rho(t_{cut}) \gtrsim 90$ % for both samples. The quantities affected by the approximation performed in Eq. 5.1 are the FN efficiency and the SM purity, since resulting from the integral of Eq. 5.1 at short Δt. Using the $\bar{\nu}_e$ sample to estimate the fraction of neutrons captured at $\Delta t < 10$ μs, the FN efficiency and the SM purity results underestimated by approximately 4 %. Such correction is neglected for the SM, since its value results within the statistical uncertainty on the SM purity. Since $\bar{\nu}_e$ and FN present the same Δt distributions, the fraction of $\bar{\nu}_e$ events with $t > t_{cut}$ is assumed as FN efficiency. In this way, the FN efficiency is known with better statistical uncertainty, since $\bar{\nu}_e$ sample statistics is bigger than the FN one, and do not suffer from the approximation performed in Eq. 5.1. Final values of efficiency and purity are summarised in Tab. 5.1.

Sample	ϵ_t	ρ_t
Stopping Muon	$0.99^{+0.01}_{-0.17}$	0.88 ± 0.07
Fast Neutron	0.78 ± 0.01	$0.97^{+0.03}_{-0.08}$

Table 5.1: FN an SM separation efficiency (ϵ_t) and purity (ρ_t) for the chosen cut $t_{cut} = 10$ μs.

5.3 OV Tag analysis

The correlated background could be estimated by tagging its parent muons crossing the OV (OVT). Since the OV veto (OVV) applied in the signal selection, such tagged sample represent the events excluded from the signal selection. For this reason, this method do not help to measure the total correlated background rate, but is useful to infer its spectral shape in $[0.7, 12]$ MeV. The OVT is then performed by selecting those events rejected by the OVV, i.e. time coincidences between the prompt candidate and an OV hit in a time window of 224 ns.

In Fig. 5.4 the prompt energy spectrum in $[0.7, 30]$ MeV is shown with (red points) and without (blue point) OVT, a rather flat spectrum is observed. The OVT efficiency is estimated by comparing the high energy tail > 12 MeV with and without OVT. Assuming a flat distribution, the total OVT efficiency is estimated to be 55 ± 6 % [45].

The FN and the SM components are then separated by the Δt cut between prompt and delayed events and evaluated separately. The OVT efficiency is estimated to be (38 ± 7) % for FN and (74 ± 12) % for SM, in agreement with the total OVT efficiency. As expected, the OVT efficiency for SM is

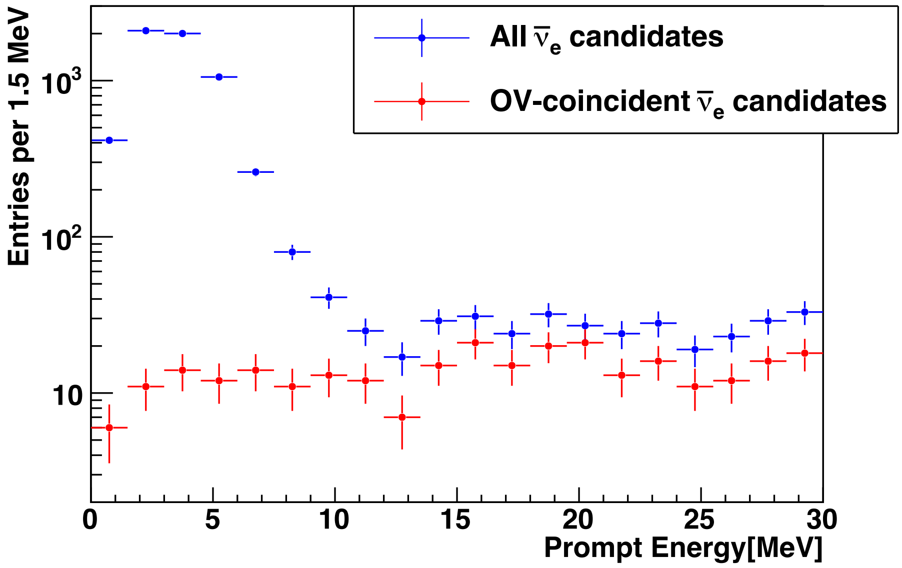

Figure 5.4: Prompt energy spectrum for candidate selected in $[0, 30]$ MeV (blue) and OVT spectrum (red). The correlated background shown a rather flat spectrum in the entire energy range. The OVT efficiency of 55 ± 6 % is estimated at high energy, $E > 12$ MeV, by comparing the number of events with and without OVT.

bigger than FN, since the muon could produce FN far away from the detector, i.e. outside the region covered by the OV, while it must pass very close to the chimney to produce SM background. Given the measured OV trigger rate of 2.7 kHz and the 224 ns time window, for the coincidence between prompt candidate and OV hit, the expected contamination from random coincidence is estimated to be < 0.6 %. The high efficiency by which the correlated background is tagged by the OV and the low contamination from accidental coincidences, i.e. high purity, are the main reason the OVV is applied to the signal selection to reduce the correlated background contamination.

The SM and FN spectral shapes in $[0.7, 30]$ MeV are shown in Fig. 5.5. The spectra are found in agreement with linear models, a negative slope is found for SM while a positive slope is found for FN. Background rate

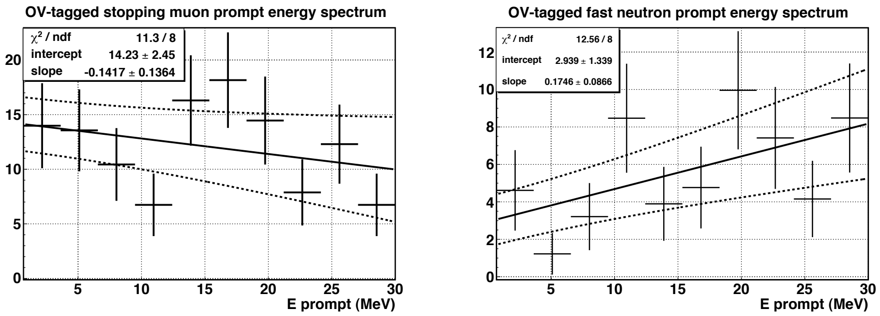

Figure 5.5: SM (left) and FN (right) samples as obtained from the OVT sample, separating the two component by a Δt cut. The spectral shape of the two components are found in agreement with linear models, a negative slope is found for SM while a positive slope is found for FN. Background rate of (0.48 ± 0.11) cpd and of (0.44 ± 0.14) cpd are obtained for SM and FN respectively, by integrating the fitted spectral shapes and rescaling by the OVT efficiencies.

of (0.48 ± 0.11) cpd and of (0.44 ± 0.14) cpd are obtained for SM and FN respectively, by integrating the fitted spectral shapes and rescaling by the OVT efficiencies [46]. The total correlated background rate obtained with OVT amount to (0.92 ± 0.18) cpd. It should be noted the correlated background rate is expected to be lower by applying the OVV, as will be discussed in the following sections.

5.4 Fast Neutrons analysis

The FN are generated with high multiplicity and some of them are expected to deposit energy in both the ID and IV, as schematised in Fig. 5.6. Upon

ID trigger both ID and IV are read-out, thus the IV detection threshold is lowered below its self-trigger threshold (~ 10 MeV). The IV is then sensible to FNs which deposit energy through proton recoil or by H capture.
The FN analysis is performed on the $\bar{\nu}_e$ candidate selected by requiring the prompt energy in $[0.7, 30]$ MeV and applying the FN/SM separation cut $\Delta t > 10$ μs. The OVV is omitted in order to increase the statistics of the IVT sample and to allow the comparison with the results obtained with the OVT. The OVV will be applied later.

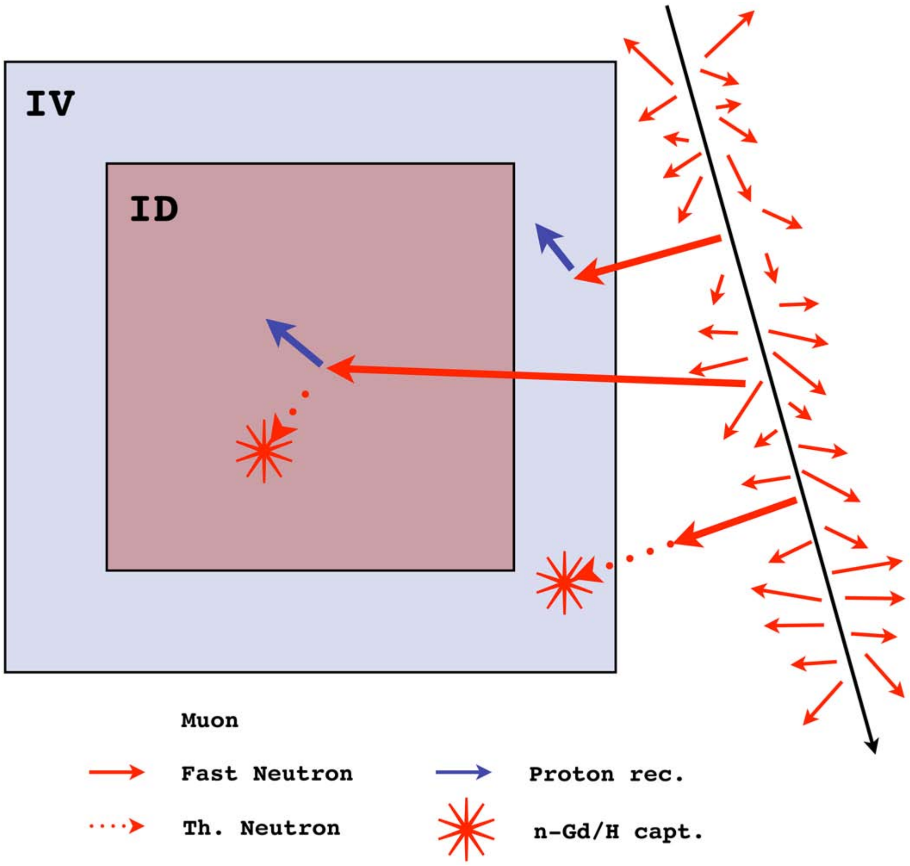

Figure 5.6: Fast neutron event topology as generated by muons creating neutron with high multiplicity. The FN interacting in the ID mimic the $\bar{\nu}_e$ signature. The IV is sensitive to FN via proton recoil or neutron capture on H, which allow the FN to be tagged.

5.4.1 IV Tagging

Since the IV is a scintillator detector, nearly all energy deposited by a FN, or any other particle, is visible without any detection threshold.
The tagging condition between the ID and the IV implicitly define a time coincidence within the read-out time window of 256 ns. The IV PMT dark noise, with a rate of $\sim$ 10 kHz, is expected to produce accidental tagging with a negligible rate of $\sim 2 \times 10^{-4}$ Hz by requiring a time coincidences in such short time window. However, coincidences between ID energy deposition and natural radioactivity in the IV contaminates the low energy part of the IV spectrum, $\lesssim$ 1 MeV, as shown in Fig. 5.7. A tagging threshold $>$ 1 MeV would select a rather clean sample of FN but would reduce the sample statistics, while a threshold $<$ 1 MeV would not easily allow to distinguish physics events from natural radioactivity gamma.

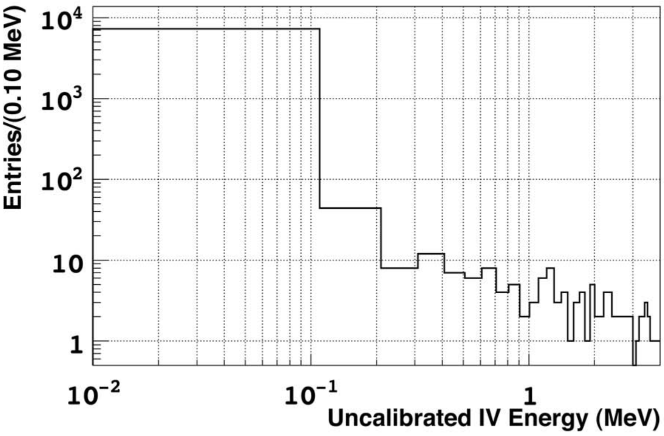

Figure 5.7: The IV energy spectrum in coincidence with a prompt energy deposition in the ID. The lower part of the spectrum, $\lesssim$ 1 MeV, is dominated by natural radioactivity gamma and PMT dark noise.

An alternative tagging condition based on the number of IV PMT hits has been proposed in [43] and used in this analysis. The multiplicity condition implicitly define a charge threshold, independent from the absolute energy scale of the IV. A rather large energy deposition within the field of view of at least 2 IV PMTs, in coincidence with a prompt-like event in the ID, is more likely caused by correlated physics. Therefore, tagging events with 2 or more PMT hits allow to reduce accidental coincidences with natural radioactivity, since low energy events are expected to hit only one PMT.
Fig. 5.8 shows the IV energy spectrum obtained for different values of hit multiplicity. Requiring the PMT multiplicity to be bigger than 2 rejects

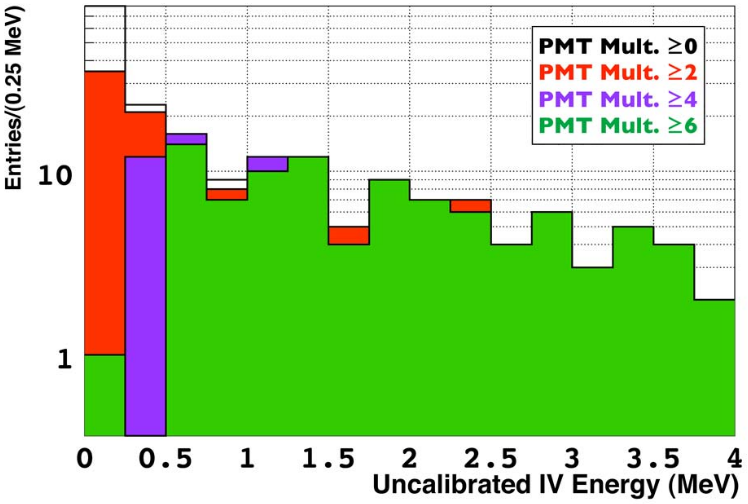

Figure 5.8: The IV energy spectrum obtained for different multiplicity condition. Requiring the PMT multiplicity to be bigger than 2 rejects most of the low energy events (< 0.25 MeV), likely due to PMT radioactivity, while allows to tag physics events from very low energy (> 1.00 MeV).

most of the low energy events, < 0.25 MeV, and allows to tag physics events with energy > 1.00 MeV. Fig. 5.9 show the vertex distribution of the IVT sample. As expected for FN events, no correlations are observed for both prompt and delayed events. Fig. 5.10 shows there is no correlation between the ID and the IV energy depositions. Since the IVT rely on the high multiplicity the FNs are created by their parent muon, the tagged FN is a separated event from the one interacting in the ID.

Num. PMT hit	evt. [0.5;30] MeV	evt. [12;30] MeV	ϵ_{IVT} [%]
0	7447	199	–
2	156	65	33 ± 5
4	110	50	25 ± 4
6	94	45	23 ± 4

Table 5.2: Number of IVT events and tagging efficiency (ϵ_{IVT}), for different PMT multiplicity.

Tab. 5.2 summarise the number of events passing IVT, between $[0.5, 30]$ MeV and $[12, 30]$ MeV, where a pure sample of FN is obtained. The ratio of events in $[12, 30]$ MeV between the events passing the IVT over the total, give an

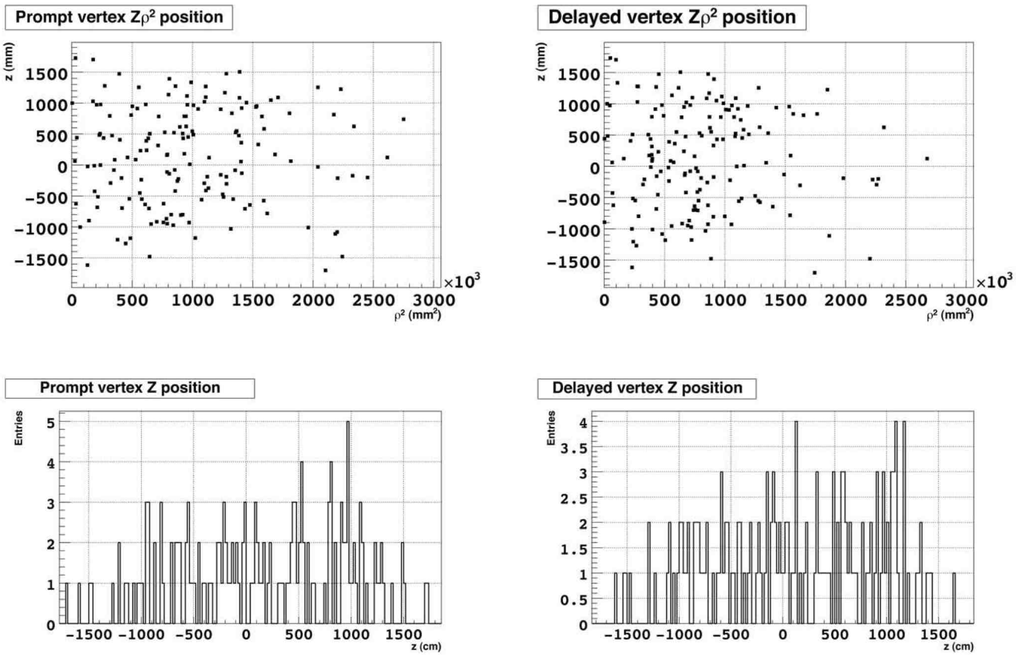

2

Figure 5.9: Vertex distribution for IVT prompt (left) and delayed (right) event, with PMT multiplicity ≥ 2. An uniform distribution for both prompt and delayed is observed, as expected from FN events.

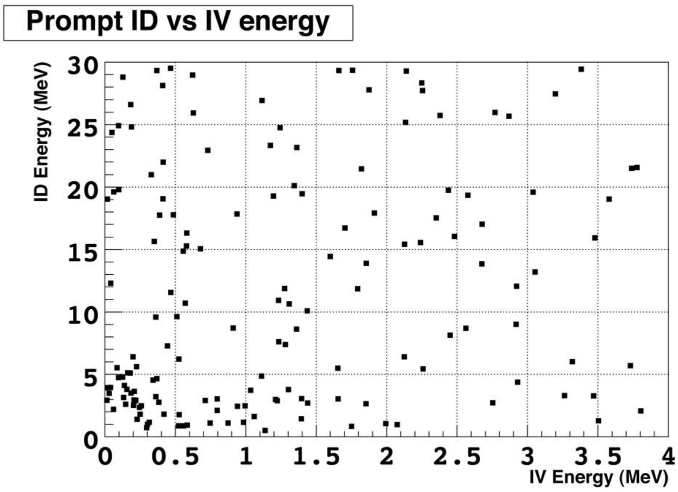

Figure 5.10: ID energy as a function of the IV energy for IVT events. Since the IVT rely on the high multiplicity the FNs are created by their parent muon, the tagged FN is a separated event from the one interacting in the ID. An excess of events in $E_{ID} \lesssim 5$ MeV and $E_{IV} \lesssim 1$ MeV suggest some background contaminate the IVT sample.

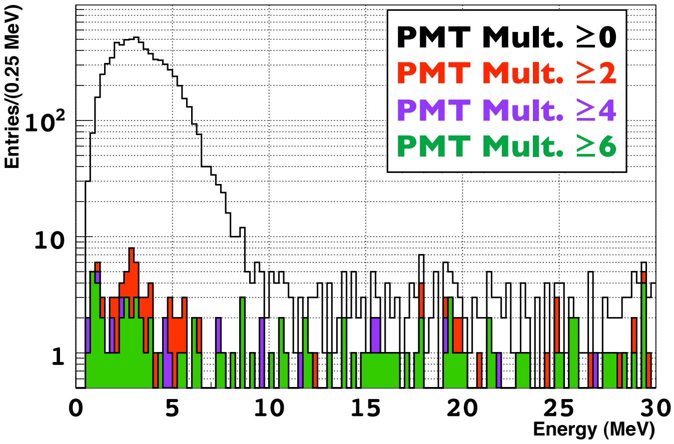

Figure 5.11: Prompt energy spectrum for different IVT multiplicity condition. The IVT based on the number of IV PMT hit allows then to tag FN events produced with high multiplicity by a muon interacting outside the detector. The tagging efficiency is measured between 33 % and 23 %, depending on the multiplicity condition. An excess of events in $E_{ID} \lesssim 5$ MeV suggest some background contaminate the IVT sample.

estimation of how many FN are in coincidence with an energy deposition in the IV, i.e. the IVT efficiency ϵ_{IVT}. The tagging efficiency is measured between 33 % and 23 %, depending on the multiplicity condition. The prompt energy spectrum for the different IVT multiplicity condition is shown in Fig. 5.11.
The minimal condition of 2 PMT hit is assumed as IVT condition in the following analysis. The systematic uncertainties introduced by such condition are discussed in Sec. 5.4.5.

5.4.2 IVT background

The correlation between ID and IV energy shown in Fig. 5.10 presents an excess of events $\lesssim$ 5 MeV in the ID and $\lesssim$ 1 MeV in the IV. Such excess, also visible in the prompt energy spectrum of Fig. 5.11, is understood in term of backgrounds contaminating the IVT sample. Given the topology of the IVT events, which require a three-fold coincidence between IV energy deposition, ID prompt event and the following ID delayed, two categories of background, with similar topologies, have been identified:

$\gamma\gamma$-events: generated by low energy γ from natural radioactivity. The γ undergoes Compton scattering in the IV and in the ID where, in accidental coincidence with a thermal neutron, it mimics the FN signature. As the accidental background discussed in Sec. 4.3.1, the $\gamma\gamma$ energy distribution is expected to contaminate the IVT sample up to ~3 MeV in the ID. Due to the rather poor light collection efficiency and energy resolution of the IV, such background deposit energies $\lesssim$ 1 MeV in the IV. The expected event topology is schematised in box 2 of Fig. 5.12.

$\bar{\nu}_e$ + IVT from γ/n: generated by an accidental coincidence between an $\bar{\nu}_e$ interacting in the ID and an IV γ from natural radioactivity or thermal neutron capture on H. Since the ID energy deposition is produced by a true $\bar{\nu}_e$ events, the ID energy distribution shown its spectrum, with a peak around ~3 MeV. As observed for the $\gamma\gamma$-background, the energy distribution in the IV is limited $\lesssim$ 1 MeV. The expected event topology is schematised in box 3 of Fig. 5.12.

As summarised in Tab. 5.3, tagged FN events are expected to show two kind of correlations, between prompt and delayed event in the ID but also between the ID and the IV energy deposition. The time and the spatial correlations between prompt and delayed events in the ID are the results of a single particle generating both prompt and delayed events, in a similar way as $\bar{\nu}_e$ events. The correlation between IV and ID take place since both signals are generated by the same parent muon. The time correlation between ID and IV signals is expected in a short time window of few tens ns, dominated by the particles time of flight between IV and ID.

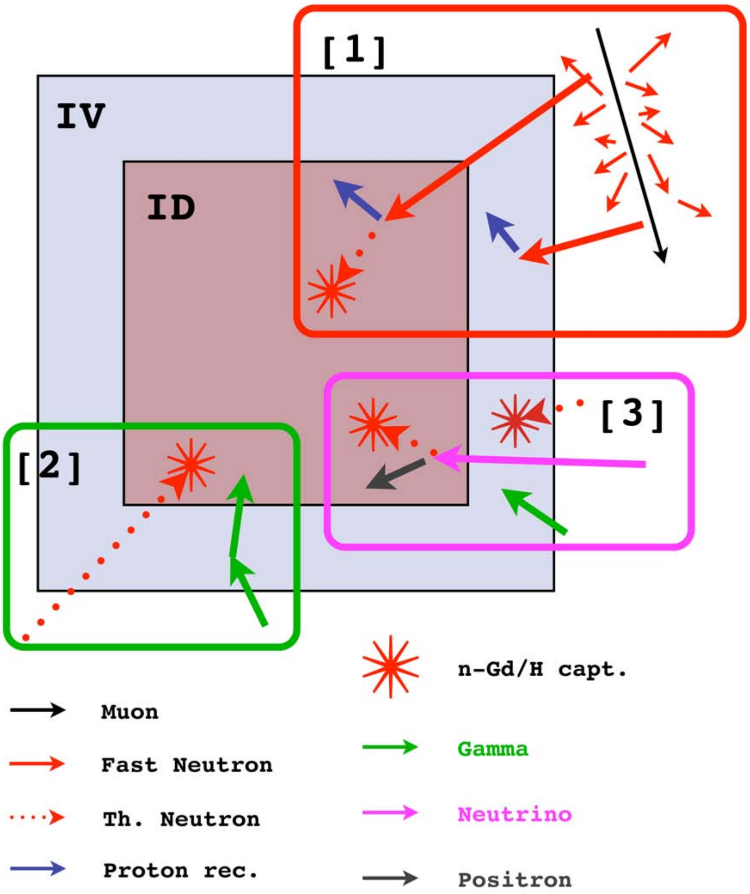

Figure 5.12: Fast Neutron and Background event topology. Box 1 schematises IV Taggable FN event. Box 2 schematises $\gamma\gamma$ background generated by low energy γ from natural radioactivity. The γ undergoes Compton scattering in the IV and in the ID where, in accidental coincidence with a thermal neutron, it mimics the FN signature. Box 3 schematises $\bar{\nu}_e$ + IV γ/n background generated by an accidental coincidence between an $\bar{\nu}_e$ interacting in the ID and an IV γ from natural radioactivity or thermal neutron capture on H.

Correlation	Fast Neutron Box 1	$\gamma\gamma$-events Box 2	$\bar{\nu}_e$ + IV γ/n Box 3
ID only time & space	✓	✗	✓
ID - IV time & space	✓	✓	✗

Table 5.3: Space and time correlation for IVT fast neutron and its backgrounds

On the other hand, $\gamma\gamma$-events and $\bar{\nu}_e$ + IV γ/n events do not present both kind of correlations. The $\gamma\gamma$-events shown correlation between the ID prompt-like event and the IV event, because both are generated by the same particle, but it lacks correlation between the prompt-like and the delayed-like event in the ID. The $\bar{\nu}_e$ + IV γ/n show correlation between prompt and delayed events, since they are generated by a true $\bar{\nu}_e$, but it lacks the correlation between the ID event and the IV event, since due to an accidental coincidence.
Such different correlations are exploited in the following two sections to quantify and reject the background contaminating the IVT sample.

$\gamma\gamma$ background

In Fig. 5.13 the distance between prompt and delayed events for $\bar{\nu}_e$ candidates is shown together with the expected distribution from $\bar{\nu}_e$ MC and the contribution from accidental background. The $\bar{\nu}_e$ candidates are correlated up to $\sim$ 1.5 m, while above such distance the distribution is dominated by the accidental background. The FNs are expected to have prompt/delayed spatial correlation similar to the $\bar{\nu}_e$ events, while $\gamma\gamma$ background are expected to have the same distribution as the accidental background.
A comparison between the IVT sample and the contamination from $\gamma\gamma$ background is shown in Fig 5.14. The $\gamma\gamma$ sample is obtained by performing off-time window coincidence between $[1010, 1100]$ μs. A total of 19 events are found, corresponding to $\sim$ 12 % of the IVT sample. The $\gamma\gamma$ background contaminates, as expected, the low energy part of the energy spectrum, up to $\sim$ 2 MeV on the ID and up to $\sim$ 1 MeV on the IV. The FN sample shows spatial correlation up to $\sim$ 1 m while $\gamma\gamma$ background extends beyond 1 m. The vertex distribution from $\gamma\gamma$ background shows a distribution close to the outer most region of the ID, as expected from γ originating from outside the ID.
A cut on the distance between prompt and delayed candidate is applied to reduce $\gamma\gamma$ background contamination to the IV Tagged sample. The cut value is set at 1.5 m, where the accidental component become dominant, as shown in Fig. 5.13. Of the 19 events selected with the off-time search, 16 events

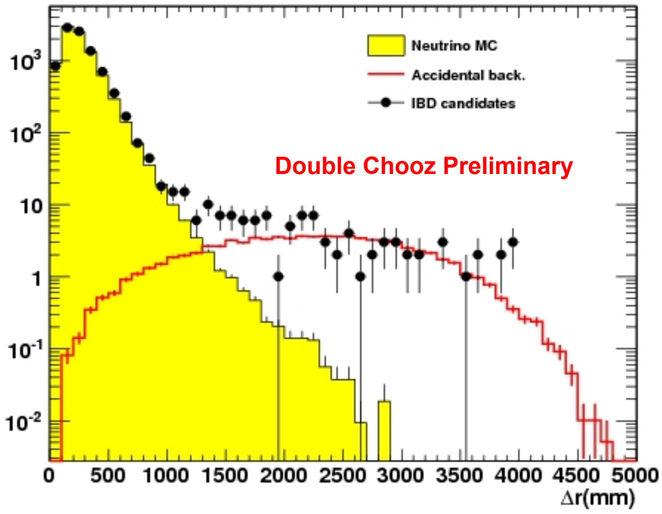

Figure 5.13: Prompt/Delayed spatial correlation for neutrino candidates (black points), $\bar{\nu}_e$ MC (yellow histogram) and for accidental background from off-time window selection. The $\bar{\nu}_e$ candidates are correlated up to ~ 1.5 m, while above such distance the distribution is dominated by the accidental background. The FNs are expected to have prompt/delayed spatial correlation similar to the $\bar{\nu}_e$ events, while $\gamma\gamma$ background are expected to have the same distribution as the accidental background.

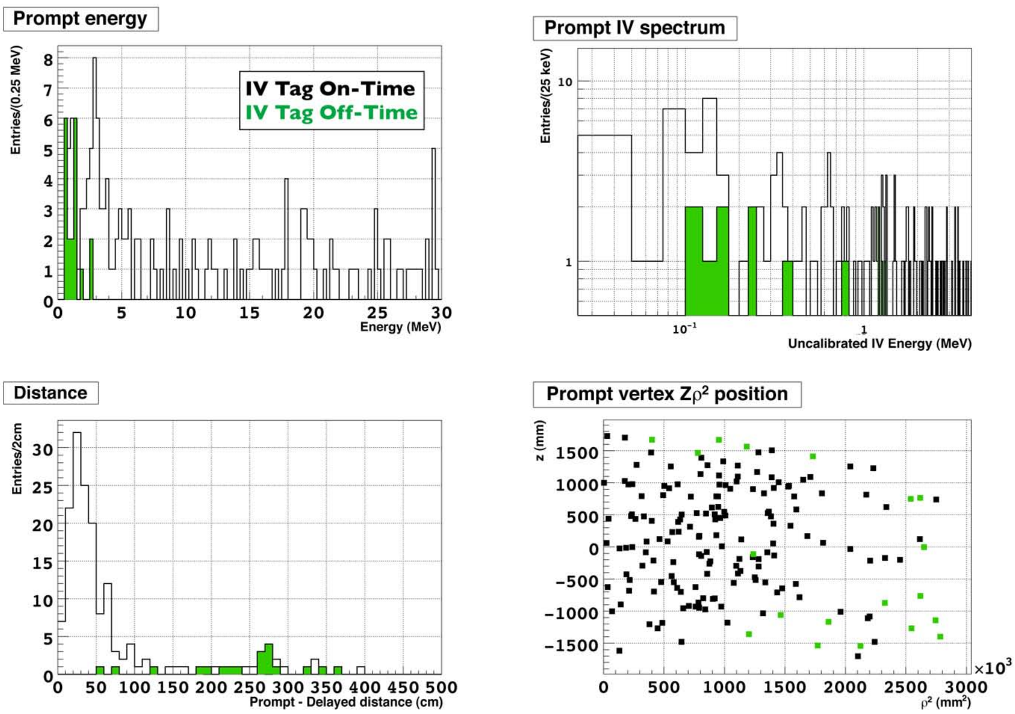

Figure 5.14: Comparison between IVT sample (black histogram) and $\gamma\gamma$ background (green histogram). The ID prompt energy spectrum (top left) shows the $\gamma\gamma$ background contaminates, as expected, the low energy part of the energy spectrum, up to ~ 2 MeV. The IV prompt energy spectrum (top right) shows the $\gamma\gamma$ background contaminates, as expected, the low energy part of the IV energy spectrum, up to ~ 1 MeV. The IVT sample shows spatial correlation up to ~ 1 m while $\gamma\gamma$ background extends beyond 1 m (bottom left). The vertex distribution (bottom right) from $\gamma\gamma$ background shows a distribution close to the outer most region of the ID, as expected from γ originating from outside the ID.

Tag thr.	evt. $d_{P/D} < 1.5$ m	evt. $d_{P/D} > 1.5$ m	ϵ_d [%]
Mult. ≥ 2	3	16	84 ± 8
Mult. ≥ 4	2	10	84 ± 11
Mult. ≥ 6	1	9	90 ± 9

Table 5.4: Expected number of $\gamma\gamma$ background events and background rejection efficiency (ϵ_d) with prompt/delayed distance cut, for different IVT multiplicity condition. The background rejection efficiency is independent from the IVT multiplicity condition, suggesting the systematic related to the background rejection is negligible.

shown a distance between prompt and delayed bigger than 1.5 m and are thus rejected by the distance cut. The remaining background amount to 3 events, corresponding to ~ 2 % of the IVT sample. The rejection efficiency (ϵ_d) is estimated to be 84 ± 20 %, the rather big statistical uncertainty is due to the low statistics available by selecting $\gamma\gamma$ events with only one off time window.
The number of IVT events selected off-time and the $\gamma\gamma$ background rejection efficiency are summarised in Tab. 5.4, for different IVT multiplicity condition. The rejection efficiency is found constant within statistical uncertainty, suggesting the systematic related to $\gamma\gamma$ background rejection, introduced by the choice of the IVT multiplicity, is negligible.

$\bar{\nu}_e$ + IV γ/n background

The $\bar{\nu}_e$ + IV γ/n background does not present time nor spatial correlation between prompt and IV energy depositions, as summarised in Tab. 5.3. The spatial and the time distributions between prompt and IV energy depositions could then be used as discriminants in order to separate such background from the IVT FN. The spatial correlation has not been evaluated yet, since it requires an IV vertex reconstruction algorithm, which is currently under development. However, the design of the IV has been optimised for tagging high energy deposition from muons and not to detect point-like energy deposition, as the ID. The IV vertex reconstruction algorithm is then not expected to show good vertex resolution and consequently an high background discrimination efficiency is not expected. On the other hand, the pulse start time is available for both ID and IV waveforms. The time distribution is expected to show better discrimination efficiency than the spatial distribution, since the time is measured with an uncertainty of the order of <2 ns (FADC sampling time).
Fig. 5.15 shows the difference between the pulse start time in the IV and

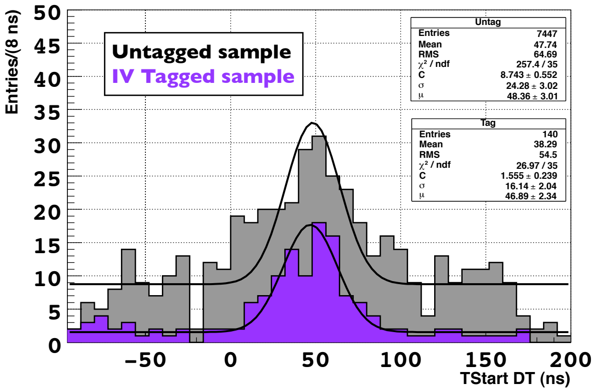

Figure 5.15: Difference between IV and ID pulse start time for untagged (grey) and IVT (violet) sample. The pulse start time distribution shows a correlated component within a rather narrow peak and a flat uncorrelated component off-peak. The pulse start time distribution is fitted (black line) with a constant function, to account for the uncorrelated component, and a gaussian function, to account for the correlated one. The background contamination is estimated integrating the flat component to be 58 ± 8 events. The background is then reduced by applying a cut in the pulse start time. Requiring events on-peak, within $[-2, 95]$ ns (i.e., 3σ), allows to select ~ 99.7 % of the FNs while rejecting ~ 67 % of the background.

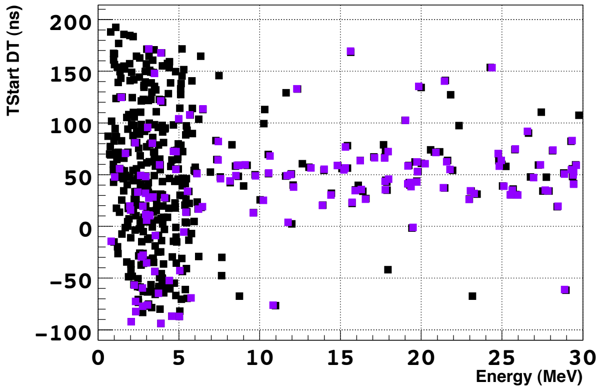

Figure 5.16: Difference between IV and ID pulse start time as a function of the prompt energy for untagged (grey) and IVT (violet) sample. The correlation with energy suggests the events on-peak (energy up to 30 MeV) to be most likely FN while the off-peak flat component (energy up to 12 MeV) to be most likely $\bar{\nu}_e$ + IV γ/n background.

ID, while Fig. 5.16 shows its correlation with the ID prompt energy. The untagged sample, if found in coincidence with and IV energy deposition, is also shown in the plots for comparison. The pulse start time distribution shows a correlated component within a rather narrow peak and a flat uncorrelated component off-peak. The correlation with energy suggests the events on-peak (energy up to 30 MeV) to be most likely FN while the off-peak flat component (energy up to 12 MeV) to be most likely $\bar{\nu}_e$ + IV γ/n background. The peak of the distribution is centred at $\sim$ 50 ns because an intrinsic delay between IV and ID waveforms (different cable length, software delay, etc.), while the peak width is expected to be dominated by the trigger jitter time, of about 16 ns. The IVT and the untagged sample show a slightly different peak position due to trigger time walk effect, i.e. the trigger release time depend from the deposited energy.
The pulse start time distribution is fitted with a constant function, to account for the uncorrelated component, and a gaussian function, to account for the correlated one. The fit results are shown in Fig. 5.15. Integrating the flat distribution, a total background contamination of 58 ± 8 events is estimated, corresponding to $\sim$ 37 % of the IVT sample.
The background is then reduced by applying a cut in the pulse start time. According to the performed fit, requiring events on-peak, within $[-2, 95]$ ns (i.e., 3σ), allows to select $\sim$ 99.7 % of the FNs while rejecting $\sim$ 67 % of the background. The remaining $\bar{\nu}_e$ + IV γ/n background is estimated assuming a flat pulse start time distribution to be 19 events, corresponding to $\sim$ 12 % of the IVT sample.
As summarised in Tab. 5.5, the rejection efficiency (ϵ_{TS}) of the $\bar{\nu}_e$ + IV γ/n background is independent from the IVT multiplicity condition, suggesting the systematic related to the background rejection is negligible.

Tag thr.	evt. on-time $[-2, 95]$ ns	evt. off-time $[-256, -2]$ & $[95, 256]$ ns	ϵ_{TS} [%]
Mult. ≥ 2	19 ± 4	39 ± 6	67 ± 6
Mult. ≥ 4	8 ± 3	16 ± 5	67 ± 9
Mult. ≥ 6	6 ± 2	13 ± 4	68 ± 11

Table 5.5: Expected number of $\bar{\nu}_e$ + IV γ/n background and rejection efficiencies (ϵ_{TS}) with a cut on the difference of the pulse start time between ID and IV, for different IVT multiplicity condition. The background rejection efficiency is independent from the IVT multiplicity condition, suggesting the systematic related to the background rejection is negligible.

Fig. 5.17 shows comparison between IVT sample and $\bar{\nu}_e$ + IV γ/n sample, selected with an off-peak window (pulse start time in $[-256, -2]$ & $[95, 256]$ ns). The prompt energy distribution in the ID (top left) is peaked at ~ 3 MeV, the spatial correlation between prompt and delayed events (bottom left) shows correlation up to ~ 1 m and the prompt vertex distribution (bottom right) is uniform in the ID, as expected from $\bar{\nu}_e$ in the ID. The IV energy distribution (top right) shows a low energy exponential-like component, as expected by γ radioactivity depositing some energy in the IV, and a peak in $[1, 2]$ MeV, as expected by neutron capture on H or by the Tl line from natural radioactivity. The distribution in Fig. 5.17 confirm then the topology generating such background is due to an $\bar{\nu}_e$ interacting in the ID in random coincidence with a γ from natural radioactivity or a thermal neutron interacting in the IV.

5.4.3 IVT summary

The FNs have been separated by the SM component by requiring the time correlation between the prompt and the delayed events to be > 10 μs. At high energy, $[12, 30]$ MeV, a FN sample is obtained with an efficiency of 78 ± 1 % and a purity of 97^{+3}_{-8} %. A low energy FN sample, $[0.7, 12]$ MeV, has been selected with an efficiency of 33 ± 5 % by a tag strategy based on the number of PMT hit in the IV. FN are IVT if the ID prompt candidate is found in coincidence with an IV energy deposition presenting PMT multiplicity $\geqslant 2$.

Two background components contaminating the IVT sample in the low energy part of the prompt spectrum, $\lesssim 5$ MeV, have been identified though their three-fold coincidence patterns among the IV energy deposition, ID prompt event and the following ID delayed. The backgrounds have been reduced to ~ 14 % by dedicated cuts using time and spatial variables.

Since the IVT efficiency is evaluated at high energy, it is immune to any background contamination.

The cuts performed to obtain the IVT FN sample and to reject the background are summarised in Tab. 5.6 with the total number of events selected at each step. A purity of the IVT FN sample of 86 % is obtained.

	evt.
IVT (PTM multiplicity ≥ 2)	156
Prompt-delayed dist. $<$ 150 cm	140
Pulse start time $\in$ [-2,95] ns	110

Table 5.6: Summary of the cuts defining the IVT samples together with the number of tagged events at each stage.

The spectral shape of the remaining $\gamma\gamma$ background contamination has been obtained considering the off-time sample passing the IVT cuts sum-

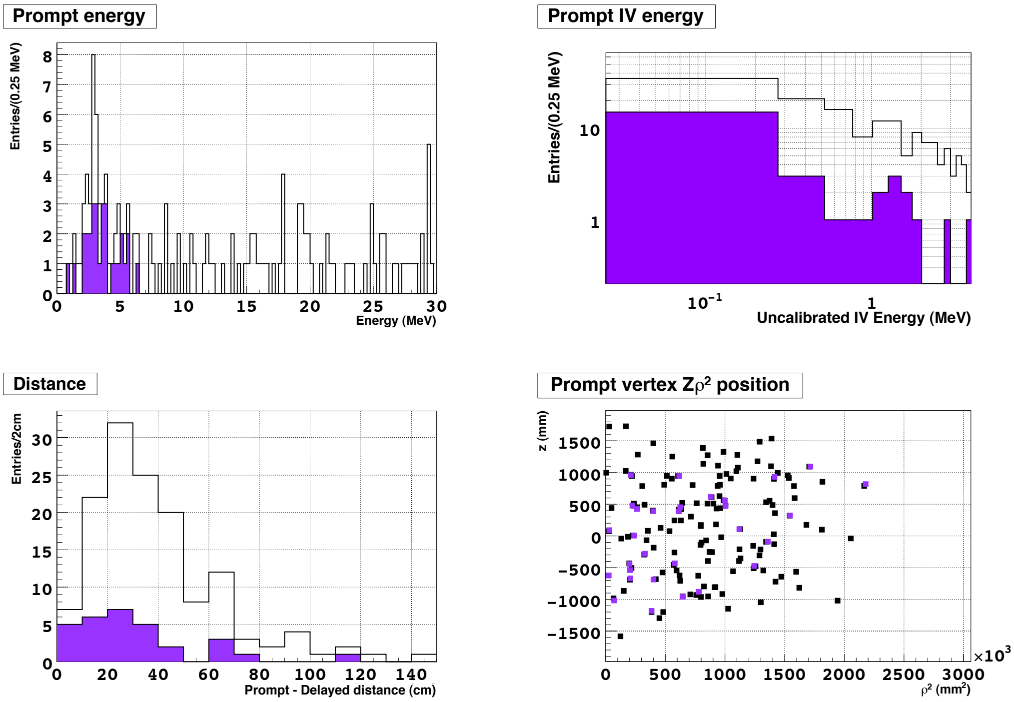

Figure 5.17: Comparison between IVT sample (black histogram) and $\bar{\nu}_e$ + IV γ/n background (violet histogram). The ID prompt energy spectrum (top left) shows the background contaminates the low energy part of the spectrum in $[2, 4]$ MeV, with a peak at ~ 3 MeV, as expected by $\bar{\nu}_e$. The IV energy distribution (top right) shows a low energy exponential-like component, as expected by γ radioactivity depositing some energy in the IV, and a peak in $[1, 2]$ MeV, as expected by neutron capture on H or by the Tl line from natural radioactivity. The correlation between prompt and delayed events (bottom left) shows correlation up to ~ 1 m while the prompt vertex distribution (bottom right) is uniform in the ID, as expected from $\bar{\nu}_e$ in the ID.

marised in Tab. 5.6 (3 events remaining). The spectral shape of the remaining $\bar{\nu}_e$ + IV γ/n background contamination has been obtained by selecting events with an off-peak pulse start time window (pulse start time $\in [-256, -2]$ & $[95, 256]$ ns, 30 events remaining) and rescaling by the number of expected background events on-peak (pulse start time $\in [-2, 95]$ ns, 19 events expected). The Fig. 5.18 shows the IVT prompt spectrum (black histogram) and the stacked expected background contamination (green and violet histograms). The number of IVT events and the expected backgrounds are summarised in Tab. 5.7. In order to minimise distortion on the IVT FN spectral shape, the remaining background contamination has been subtracted. The black points in Fig. 5.18 shown IVT FN sample upon background subtraction.

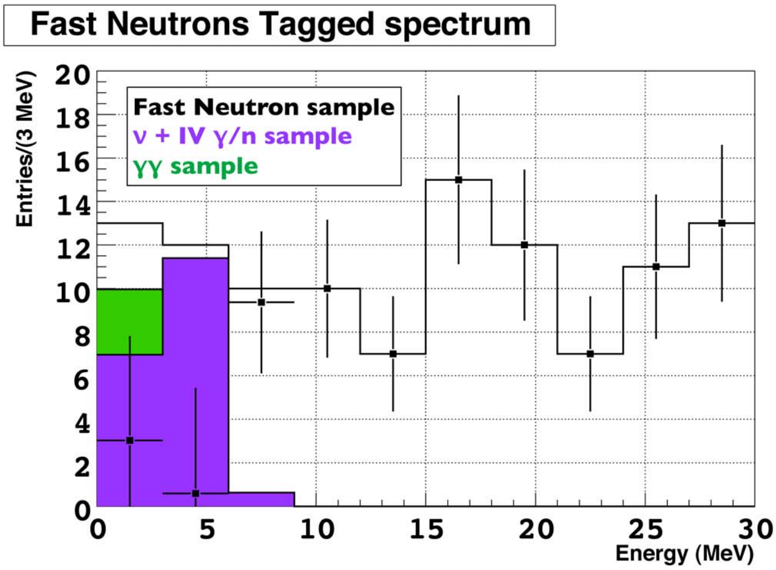

Figure 5.18: IVT FN prompt spectrum (black histogram) and the stacked expected background contamination from $\gamma\gamma$ events (green) and $\bar{\nu}_e$ + IV γ/n events (violet). Black points shows the FN spectrum upon background subtraction. In order to minimise distortion on the IVT FN spectral shape, the remaining background contamination has been subtracted (black points). The error bars account for statistical uncertainties.

	evt.
IVT	110
$\gamma\gamma$	3
$\bar{\nu}_e$ + IV γ/n	19
IVT bkg. subtracted	89

Table 5.7: Summary of the number of IVT events, background events and the total number of events upon background subtraction.

5.4.4 Fast Neutron shape and rate

The FN spectral shape $S_{FN}(E)$ is obtained by fitting the background subtracted IVT spectrum shown in Fig. 5.18. Since the IVT spectrum appear to be rather flat, a linear model is fitted. The total untagged FN rate (R_{FN}) is obtained by Eq. 5.6:

$$R_{FN} = \frac{\rho_t}{\epsilon_t \times \epsilon_{IVT}} \times \frac{1}{t_{live}} \times \int_{0.7\text{ MeV}}^{12.2\text{ MeV}} S_{FN}(E)dE \tag{5.6}$$

where the IVT rate is corrected for the FN/SM separation efficiency (ϵ_t) and purity (ρ_t) and scaled for the IVT efficiency (ϵ_{IVT}), summarised in Tab. 5.8.

ϵ_{IVT}	ϵ_t	ρ_t	t_{live} [d]
0.33 ± 0.05	0.78 ± 0.01	0.97 ± 0.08	240.17

Table 5.8: Scaling factors to obtain the untagged amount of FN events and total detector live time for rate computation.

Tab. 5.9 summarise the total statistical uncertainty, the uncertainty coming from the backgrounds subtraction and the systematic uncertainties induced by the scaling factors. The most important contribution to the total uncertainty comes from the backgrounds subtraction, which is limited by the low statistic of the background sample as summarised in Tab. 5.7. While the uncertainty on the $\bar{\nu}_e$ + IV γ/n background is expected to improve only with a bigger data sample, the uncertainty on the $\gamma\gamma$ background is expected to improve by selecting the background with multiple off-time window, in order to increase the statics of the sample. Systematic uncertainties are propagated to the IVT spectrum bin by bin.
The linear fit to the IVT spectrum and its 1σ uncertainty are shown in Fig. 5.19 . Both a flat and a sloped linear model are tested and the results are

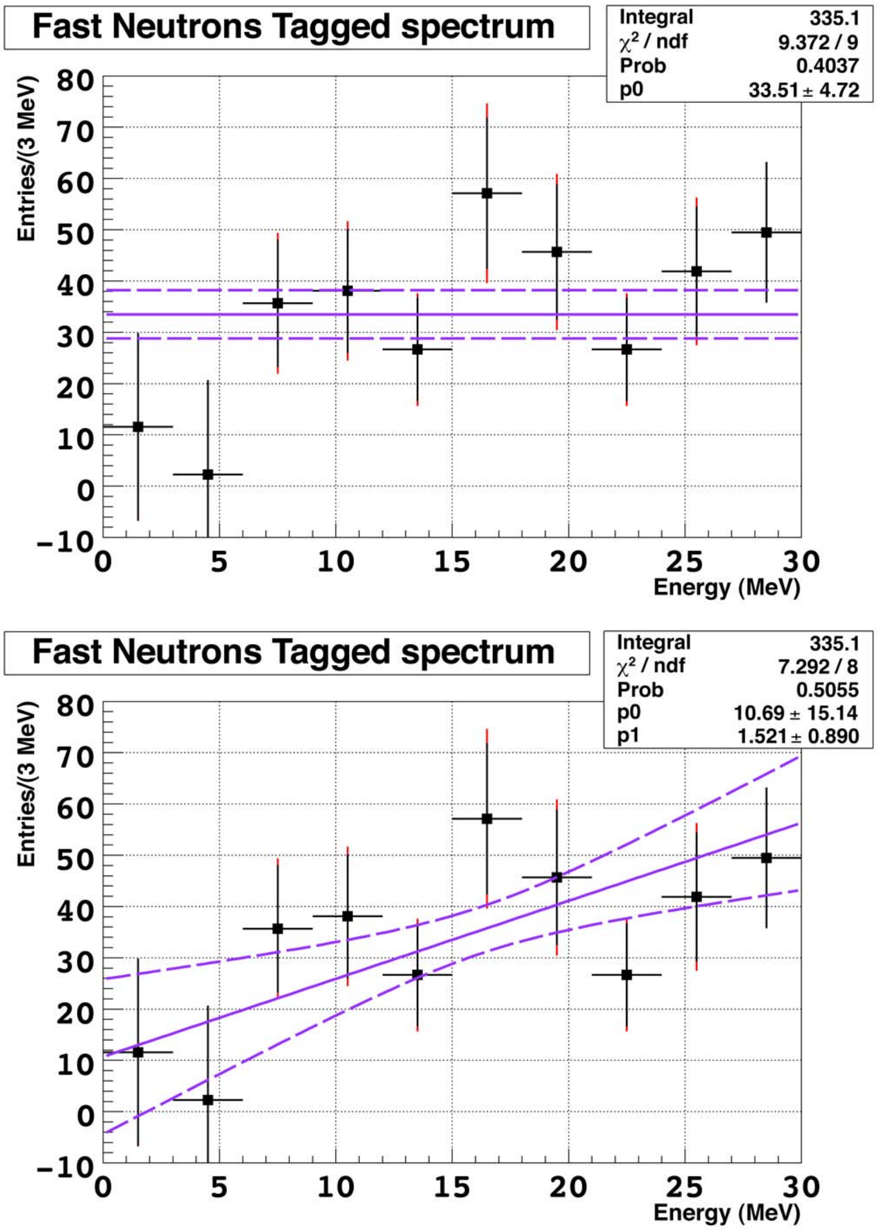

Figure 5.19: IVT FN spectrum fit with flat model (top) and sloped linear model (bottom). The flat linear model gives $\chi^2/ndf = 9.4/9$ and a fit probability of ∼ 40 %, while the sloped linear model gives $\chi^2/ndf = 7.3/8$ and a fit probability of ∼ 50 %. Since the sloped linear model shows a better agreement with the data, it is assumed as FN spectral shape. A total rate of (0.33 ± 0.16) cpd is found.

Source	stat. [%]	bkg. [%]	ϵ_{IVT} [%]	ϵ_t [%]	ρ_t [%]	total [%]
Uncertainty	9.5	62.1	15.1	1.3	8.2	65.1

Table 5.9: Break down of statistical and systematic uncertainties.

Fit model	const. [1/(3 MeV)]	slope [1/(3 MeV)^2]	χ^2/dof	R_{FN} [cpd]	$\delta(R_{FN})/R_{FN}$ [%]
Flat	33.5 ± 4.7	–	9.4/9	0.54 ± 0.07	14
Slope	10.7 ± 15.1	1.5 ± 0.9	7.3/8	0.33 ± 0.16	48

Table 5.10: Summary of FN spectral parameter and FN background rate for the flat and the sloped linear model.

summarised in Tab. 5.10. The flat linear model gives $\chi^2/ndf = 9.4/9$ and a fit probability of ~ 40 %, while the sloped linear model gives $\chi^2/ndf = 7.3/8$ and a fit probability of ~ 50 %. Since the sloped linear model shown a better agreement with the data, it is assumed as FN spectral shape. A total rate of (0.33 ± 0.16) cpd is found. The rate relative uncertainty of ~ 50 % is in agreement with the expected total error estimated in Tab. 5.9.

5.4.5 Systematics uncertainty on the IVT threshold

The IVT sample and its related background have been obtained by moving the multiplicity condition from 2 PMT hits to 4 and 6 PMT hits. The results obtained with 4 and 6 PMT hits are shown in Fig. 5.20 and summarised in Tab. 5.11. Increasing the multiplicity threshold the tagging efficiency decrease, then the number of tagged events and the expected background decrease. The spectral shape does not change by changing the IVT condition. The FN rate change up to 25 %, however, such increase is within uncertainty.

The choice of the tag multiplicity threshold do not change FN rate and shape results, suggesting the systematical uncertainties related to the IVT strategy are negligible.

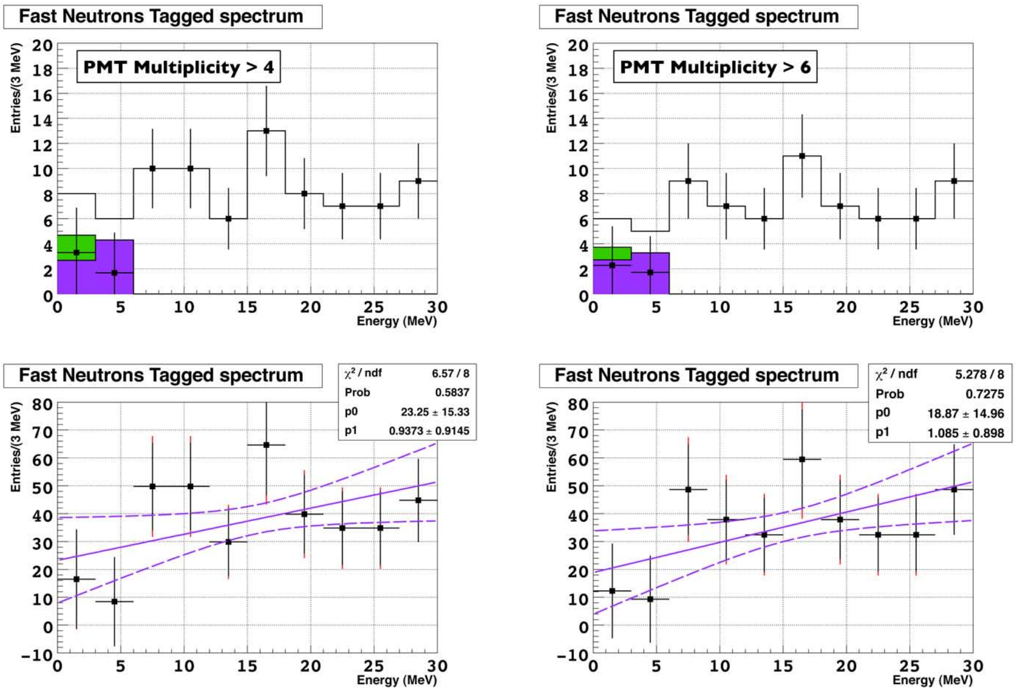

Figure 5.20: IVT spectrum and related background for for different IVT multiplicity condition. Increasing the multiplicity threshold the tagging efficiency decrease, then the number of tagged events and the expected background decrease. The IVT spectra upon background subtraction are fitted with a sloped linear models. The spectral shape does not change by changing the IVT condition. The FN rate change up to 25 %, however, such increase is within uncertainty.

Tag thr.	evt.	$\gamma\gamma$ evt.	$\bar{\nu}_e$ + IV γ/n evt.	ϵ_{IVT}	rate
Mult. ≥ 2	110	3	19	33 ± 5 %	0.33 ± 0.16 d^{-1}
Mult. ≥ 4	84	2	8	25 ± 4 %	0.44 ± 0.17 d^{-1}
Mult. ≥ 6	72	1	6	23 ± 4 %	0.41 ± 0.16 d^{-1}

Table 5.11: Number of IVT events, background events, IVT efficiency (ϵ_{IVT}) and FN rate for different IVT multiplicity condition.

5.5 Stopping Muon analysis

Stopping muon background is due to muons entering in the ID through the chimney, stopping and then decaying. The ionization energy deposited by the muon before stopping and the delayed Michel electron emitted upon muon decay mimic, respectively, the prompt and the delayed events generated by an $\bar{\nu}_e$. The time correlation between prompt and delayed events is expected to be of the order of the muon live time, $\tau_\mu \simeq 2.2$ μs, since the Michel electron deposit quickly its energy in the scintillator.
The acceptance conditions which allow a muon to enter the chimney and to deposit energy without being identified by the muon tagging are very strict, as already discussed above. For this reason, the IVT strategy developed to tag FN with high efficiency is not expected to have the same performance with SM, then a different strategy has been adopted.
The energy spectrum of the Michel electron emitted in the muon decay extends from 0 MeV up to $\sim$ 60 MeV, but only $\sim$ 1 %[1] of the total is emitted with an energy of $[6, 12]$ MeV and is expected to generate correlated background. Since the ionization energy lost by the muon before stopping is not expected to be correlated with the energy by which the Michel electron is emitted, a different delayed energy window is adopted.
The SM are separated from the FN by requiring the time correlation between prompt and delayed events to be $\Delta t < 10$ μs, with a separation efficiency of 99^{+1}_{-17} % and a sample purity of 88 ± 7 %. A pure sample of SM is then obtained by selecting the delayed event at high energy $[20, 60]$ MeV as to eliminate contamination from $\bar{\nu}_e$ and FN.
Moving the delayed energy window to high energy, an important contribution of high energy light noise (HELN) has been found. Such HELN contaminated the SM sample by making accidental coincidence with a prompt like energy deposition, due to natural radioactivity gamma or ^{12}B decay products. Since such noise shows different features with respect to the light noise contaminating the $\bar{\nu}_e$ sample, discussed in Sec. 4.1.2, it needs to be characterised and reduced by dedicated studies.
As described in Sec. 5.3 the OVT analysis could not be used to measure the rate of the correlated background since the events in coincidence with an OV hit are vetoed in the signal selection. However, the OVT analysis is useful to compare the SM background rate before apply the OVV and to validate the SM spectral shape.

---

[1] Obtained considering the standard parametrization of the Michel electron energy spectrum: $d\Gamma/dx \simeq (3x^2 - 2x^3)$, where $x = E/E_{max}$ [2]

5.5.1 High energy light noise

The light noise cut applied for the $\bar{\nu}_e$ searches ($Q_{max}/Q_{tot} < 0.09$ and $RMS(Tstart) < 40$ ns) are optimised for low energy events and do not reject HELN in an efficient way. However, LN shows negligible time correlation between prompt and delayed events and a pure sample is then selected by performing off-time selection in $[1000, 1100]$ μs time window, rescaling the sample to $[0, 10]$ μs time window used for on-time selection.

Fig. 5.21, 5.22 and 5.22 show comparison between on-time (black) and off-time (violet) selection.

The Fig. 5.21 (top left) shows the prompt energy spectrum. The low energy part of the on-time selection, < 3 MeV, shows a spectral shape similar to the one produced by natural radioactivity gamma, while it appear to be rather flat > 3 MeV. The low energy spectrum is well reproduced by the off-time HELN selection, suggesting the HELN is due to accidental coincidence from a natural radioactivity gamma and a high energy light noise emitted from some PMT. Off-time coincidence with an higher energy prompt candidate, > 12 MeV, are also observed, suggesting some accidental coincidence between two HELN events or between ^{12}B decay products and HELN.

The Fig. 5.21 (top right) shows the delayed energy spectrum. There is less HELN contamination in the low energy part of delayed spectrum, < 40 MeV, while the off-time selection reproduce well the higher part of the spectrum, suggesting more contamination.

The time distributions are shown in Fig. 5.21 (bottom). The off-time selection shows a flat distribution as expected for uncorrelated random coincidences, while the on-time sample shows the correlated distribution from SM, with a time constant of 1.9 ± 0.2 μs, defined by the muon life time.

The vertex distributions for prompt and delayed events are shown in Fig. 5.22. The on-time prompt distributions (top left and right) shows clear excess of events below the detector chimney, as expected by SM, while the off-time distribution shows events distributed more widely in the detector, as expected from natural radioactivity gammas. The delayed vertex distribution (bottom left and right) shows an excess below the chimney and some others peaks at fixed positions. Such peaks are well reproduced by the off-time selection and are due to LN. The packed distribution is an artefact of the vertex reconstruction algorithm, which reconstruct the LN vertex close to the PMT responsible of the light emission.

Finally plots in Fig. 5.23 show the Q_{max}/Q_{tot} variable as a function of the prompt (left) and delayed (right) energy. The Q_{max}/Q_{tot} variable is used together with the $RMS(Tstart)$ as low energy light noise discriminant for the signal selection. Physical events are selected by requiring $Q_{max}/Q_{tot} < 0.09$ for the prompt and $Q_{max}/Q_{tot} < 0.06$ for the delayed candidate. The Q_{max}/Q_{tot} ratio is expected to have a $1/E$ behaviour since the total deposited charge is proportional to the energy. However, such $1/E$ behaviour

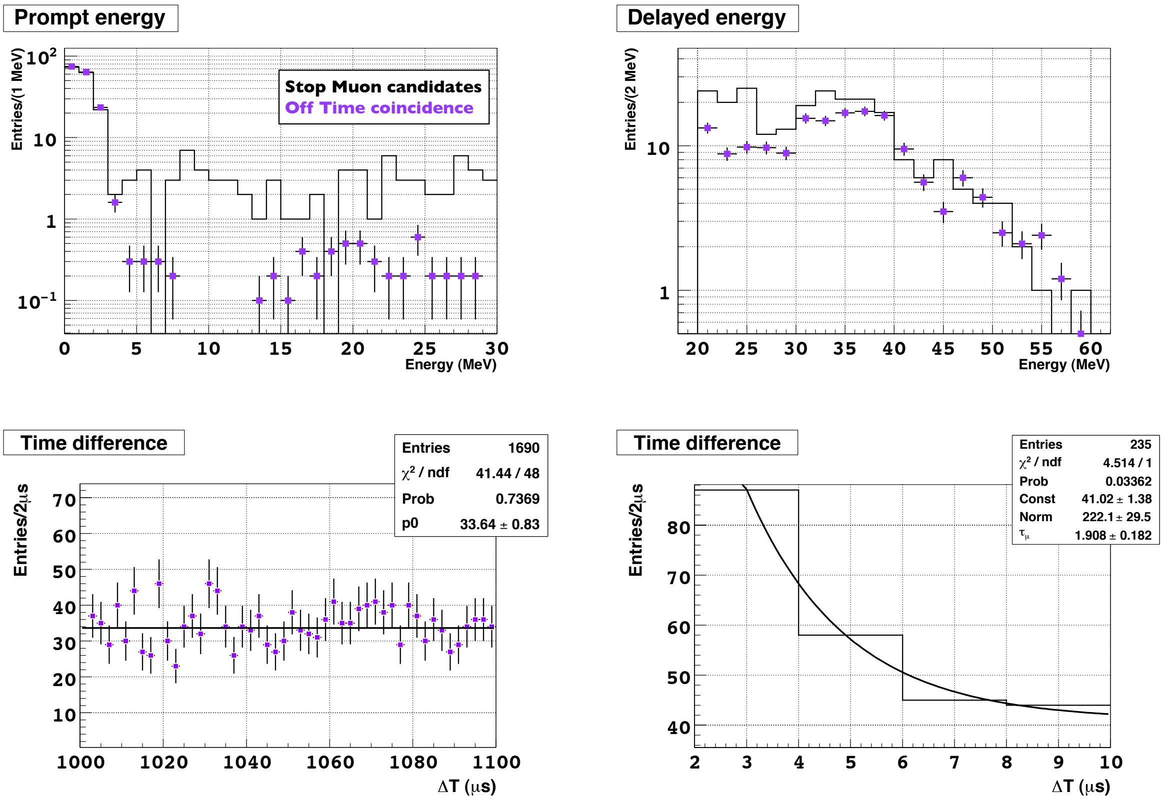

Figure 5.21: Comparison between SM candidates (black histograms) and HELN sample obtained by performing off-time selection (violet points). The low energy part of the prompt spectrum (top left) shows the characteristic shape of natural radioactivity gamma and is well reproduced by the off-time sample. Off-time coincidence with higher energy prompt candidate are also observed. The delayed energy spectrum (top right) shows less HELN contamination in the low energy part of delayed spectrum, < 40 MeV, while the off-time selection reproduce well the higher part of the spectrum, suggesting more contamination. The prompt delayed time distribution shows a flat distribution for the off-time selection (bottom left) while the on-time sample (bottom right) shows the correlated distribution from SM, with a time constant of 1.9 ± 0.2 μs.

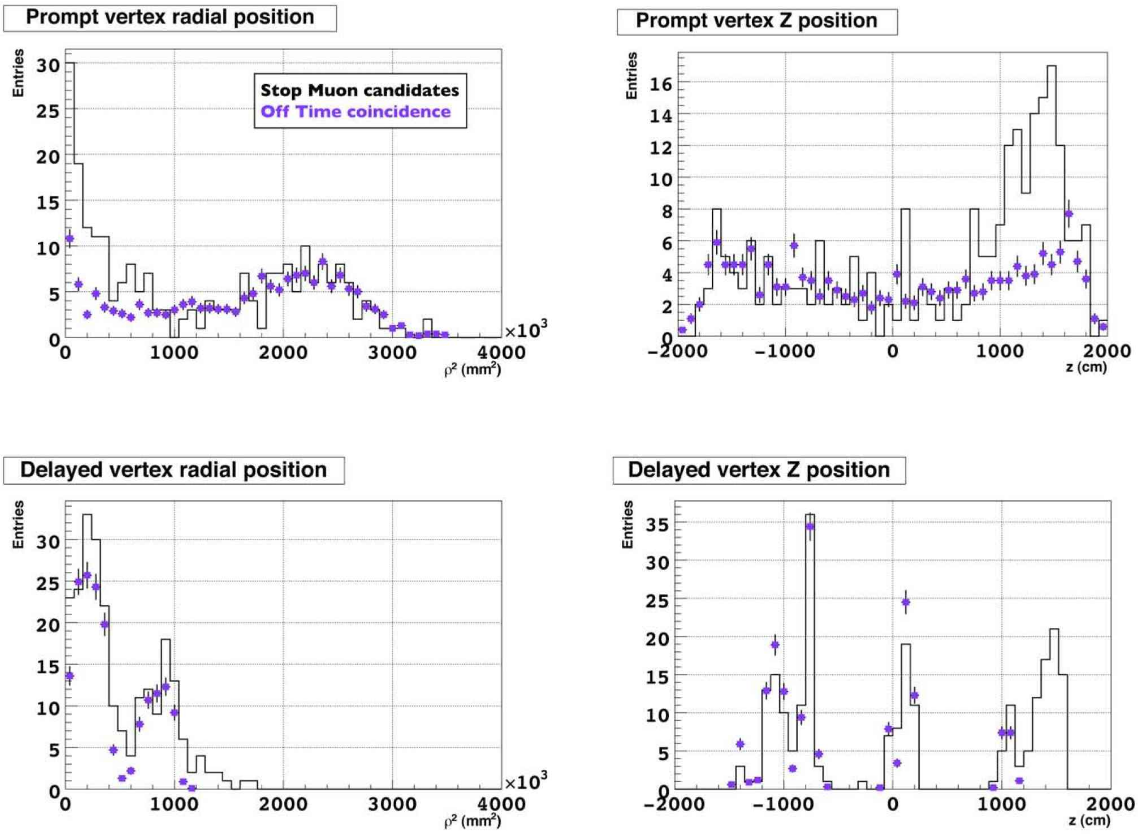

Figure 5.22: Comparison between the spatial distributions of SM candidates (black histograms) and HELN sample obtained by performing off-time selection (violet points). The on-time prompt distributions (top left and right) shows clear excess of events below the detector chimney, as expected by SM, while the off-time distribution shows events distributed more widely in the detector, as expected from natural radioactivity gammas. The delayed vertex distribution (bottom left and right) shows an excess below the chimney and some others peaks at fixed positions. Such peaks are well reproduced by the off-time selection and are due to LN. The packed distribution is an artefact of the vertex reconstruction algorithm, which reconstruct the LN vertex close to the PMT responsible of the light emission.

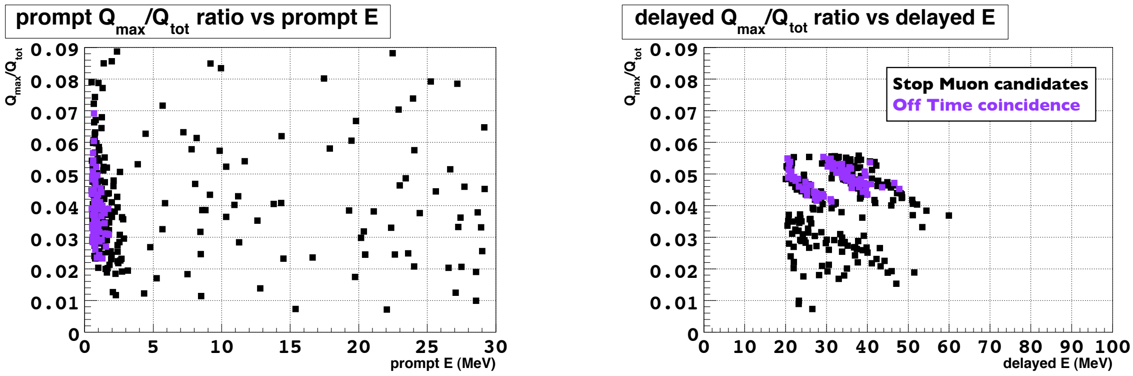

Figure 5.23: Q_{max}/Q_{tot} variable as a function of the prompt (left) and delayed (right) energy for SM candidates (black histograms) and HELN sample obtained by performing off-time selection (violet points). The SM prompt candidates shown Q_{max}/Q_{tot} distribution typical for physics events, while the delayed events show an excess of event between $[0.04, 0.06]$ with $1/E$ behaviour.

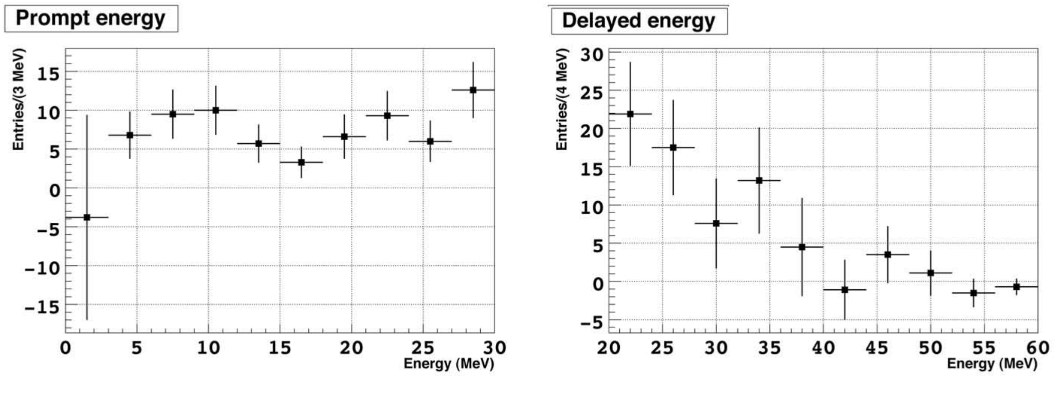

Figure 5.24: Prompt (left) and delayed (right) SM spectrum upon subtraction of HELN contamination. The error bars account for the statistical uncertainty of the data sample and the systematic uncertainty induced by the spectral subtraction.

is lost for physics events since their homogenous vertex distribution in the ID. On the other hands, the LN events are expected to be localised close to the PMT responsible of the light emission and the Q_{max}/Q_{tot} ratio shown a rather sharp $1/E$ behaviour. The SM prompt candidates shown Q_{max}/Q_{tot} distribution typical for physics events, while the delayed events show an excess of event between $[0.04, 0.06]$ with $1/E$ behaviour. The low energy LN tagging with the Q_{max}/Q_{tot} ratio is less efficient at high energy since the HELN emission is well spread over all the PMTs, producing a low Q_{max}/Q_{tot} ratio.
Since the HELN is well reproduced by the off-time window selection, the contamination found in the SM selection is reduced by subtracting the off-time contribution from the on-time prompt spectrum. The resulting prompt and delayed spectrum are show in Fig. 5.24. The error bars account for the statistical uncertainty of the data sample and the systematic uncertainty induced by the spectral subtraction.

5.5.2 Stopping Muon shape and rate

The SM spectral shape $S_{SM}(E)$ is obtained by fitting the prompt spectrum shown in Fig. 5.24. The SM spectrum appear to be rather flat, then a linear model is fitted. Since the HELN contamination affects mainly the low energy part of the prompt spectrum, the low energy bin are the most affected by the systematic uncertainty introduced by the off-time window subtraction. For this reason the fit of the spectral shape is performed above 3 MeV. The total SM rate (R_{SM}) is obtained by Eq. 5.7:

$$R_{SM} = \frac{\rho_t}{\epsilon_t} \times s_{H/L} \times \frac{1}{t_{live}} \times \int_{0.7\ \mathrm{MeV}}^{12.2\ \mathrm{MeV}} S_{SM}(E)dE \qquad (5.7)$$

where the SM rate obtained by selecting the delayed event at high energy, $[20, 60]$ MeV, is corrected for the FN/SM separation efficiency (ϵ_t) and purity (ρ_t) and scaled by to the number of events expected in the delayed energy region $[6, 12]$ MeV ($s_{L/H}$), used for signal selection. The scaling factors are summarised in Tab. 5.12.

$s_{H/L}$	ϵ_t	ρ_t	$t_{live}[d]$
5 ± 2	0.99 ± 0.17	0.88 ± 0.07	240.17 d

Table 5.12: Scaling factors to obtain the total amount of SM events and total detector live time for rate computation.

Tab. 5.13 summarise statistical uncertainty and systematic uncertainties

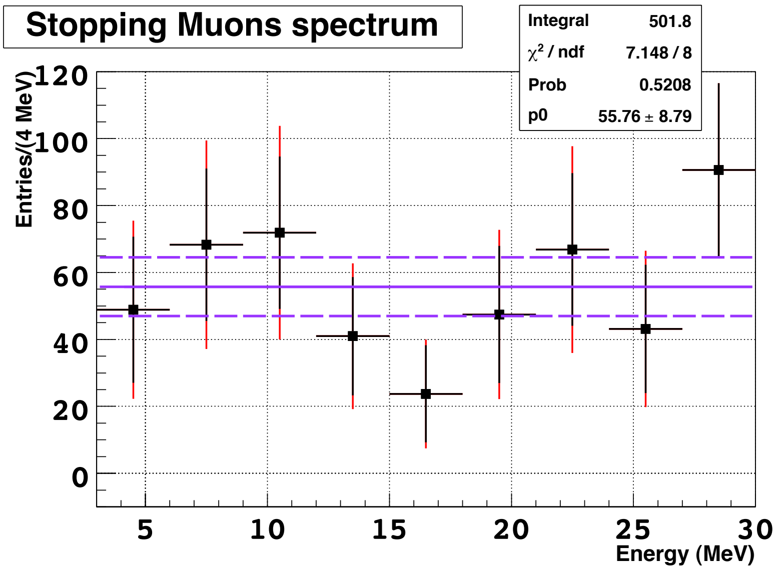

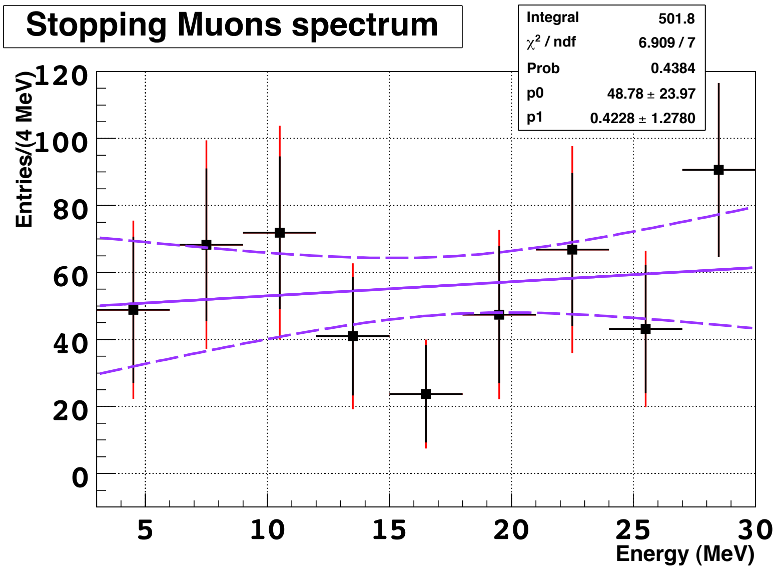

Figure 5.25: SM spectrum fit with flat model (top) and sloped linear model (bottom). The flat linear model gives a $\chi^2/ndf = 7.1/8$ and a fit probability of ~ 52 % while the sloped linear model gives a $\chi^2/ndf = 6.9/7$ and a fit probability of ~ 44 %. Both models shown compatible results however the more generic sloped shape is used as spectral shape for SM background, since there is no physical reason for a flat SM spectrum. A total rate of (0.62 ± 0.20) cpd is found.

Source	stat. [%]	$s_{H/L}$ [%]	ϵ_t [%]	ρ_t [%]	total [%]
Uncertainty	15.1	40	17.2	7.9	46.8

Table 5.13: Break down of statistical and systematic uncertainties.

induced by the scaling factors. The systematic uncertainties are propagated to the SM spectrum bin by bin.

The linear fit to the tagged spectrum and its 1σ uncertainty are shown in Fig. 5.25. Both flat and sloped linear model are tested and the results are summarised in Tab. 5.14. The flat linear model gives a $\chi^2/ndf = 7.1/8$ and a fit probability of ~ 52 %. Assuming the fitted flat spectrum, a SM rate of (0.67 ± 0.10) cpd is obtained. The sloped linear model gives a $\chi^2/ndf = 6.9/7$ and a fit probability of ~ 44 %. Assuming the fitted sloped spectrum, a SM rate of (0.62 ± 0.20) cpd is obtained. Both models shown compatible results however the more generic sloped shape is used as spectral shape for SM background, since there is no physical reason for a flat SM spectrum.

Fit model	const. [1/(3 MeV)]	slope [1/(3 MeV)^2]	χ^2/dof	R_{SM} [cpd]	$\delta(R_{SM})/R_{SM}$ [%]
Flat	55.8 ± 8.9	–	7.1/8	0.67 ± 0.10	16
Slope	48.8 ± 24.0	0.4 ± 1.3	6.9/7	0.62 ± 0.20	32

Table 5.14: Summary of SM spectra parameters and SM background rate for the flat and the sloped linear model.

5.5.3 Validating high energy light noise rejection

As discussed in the previous section, the LN rejection cuts applied for the $\bar{\nu}_e$ searches are not enough to reject efficiently the HELN affecting the SM searches. In [44], the so called *Digital* Q_{max}/Q_{tot}, defined as the Q_{max} divided by the number of ID PMT hits, has been proposed as new variable for HELN reduction. Such cut is considered and even optimised in this section to validate the LN reduction method described in 5.5.1.

Fig. 5.26 shows distributions of *Digital* Q_{max}/Q_{tot} vs prompt and delayed energy for HELN events and SM candidates. Delayed events are clearly distributed above *Digital* Q_{max}/Q_{tot} of about 40 while prompt events appear

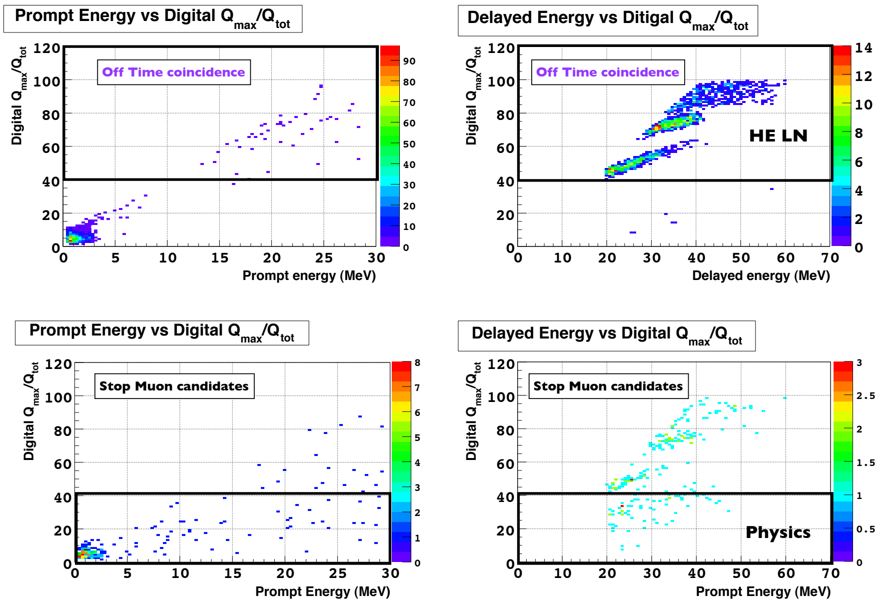

Figure 5.26: *Digital* Q_{max}/Q_{tot} vs energy for prompt (left column) and delayed (right column) for HELN events (top row) and SM candidates (bottom row). Delayed events are clearly distributed above *Digital* Q_{max}/Q_{tot} of about 40 while prompt events appear to be below such value. As discussed previously, the *Digital* Q_{max}/Q_{tot} distributions confirm that the delayed candidates at high energy are the most affected by HELN contamination.

below. As discussed previously, the *Digital* Q_{max}/Q_{tot} distributions confirm that the delayed candidates at high energy are the most affected by HELN contamination.

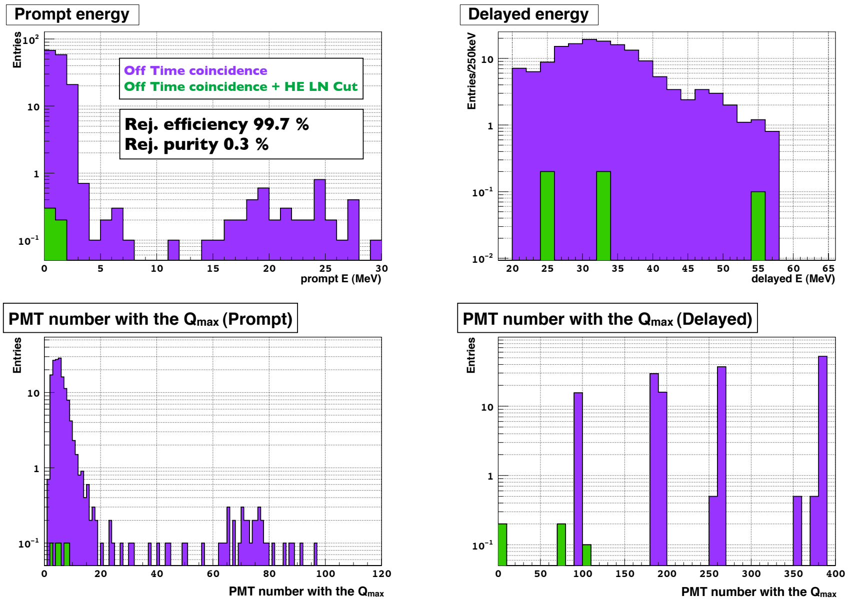

Figure 5.27: LN selection with (green) and without (violet) *Digital* Q_{max}/Q_{tot} cut. Prompt (top left) and delayed (top right) show the LN is rejected with 99.7 % efficiency requiring physics events to have *Digital* $Q_{max}/Q_{tot} < 40$. The distribution of PMT number with the Q_{max} for the delayed events (bottom right) shows a peaked distribution. Such peaks are produced by few hot PMT responsible of HELN emission, i.e. the hot PMT contains the maximum deposited charge for a given LN event. Upon *Digital* Q_{max}/Q_{tot} cut, such events disappear.

Defining *Digital* $Q_{max}/Q_{tot} < 40$ as physics events, the cut rejection efficiency is studied using the HELN sample obtained by off-time window selection. Fig. 5.27 shows LN distribution respectively with (green) and without (violet) *Digital* Q_{max}/Q_{tot} cut. Prompt and delayed energy distributions are shown in the top part of Fig. 5.27. The distribution of the PMT number[2] with the maximum charge, for prompt and delayed events, are shown in the bottom part of Fig. 5.27. The distribution of PMT number with the Q_{max} for the delayed events shows a peaked distribution. Such peaks are produced by few hot PMT responsible of HELN emission, i.e. the hot PMT contains the maximum deposited charge for a given LN event.

---

[2] Each PMT is associated to a PMT identification number.

Upon *Digital* Q_{max}/Q_{tot} cut, such events disappear. The HELN rejection efficiency (ϵ_{HELN}) is estimated to be of 99.7 % by the fraction of events rejected by the cut.

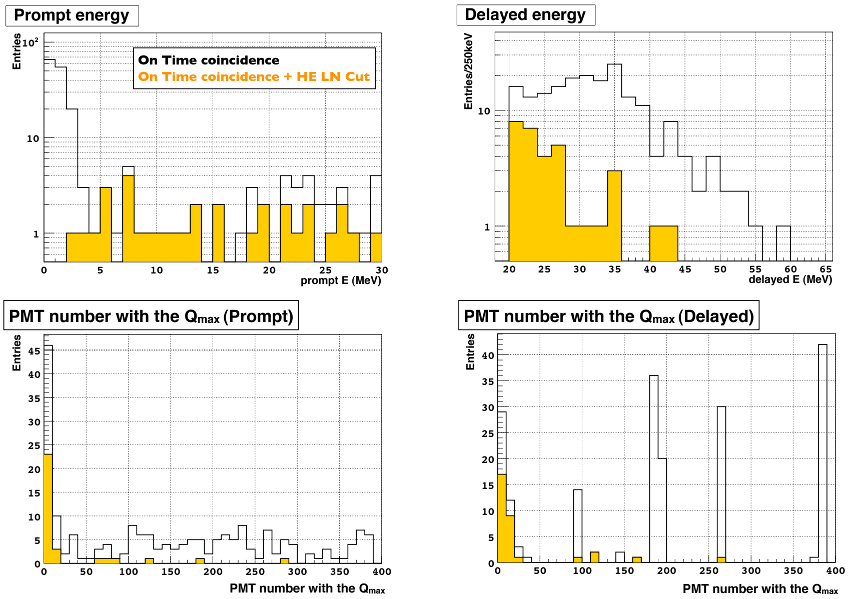

Figure 5.28: SM selection with (yellow) and without (withe) *Digital* Q_{max}/Q_{tot} cut. SM events are expected below the detector chimney, so the PMT with Q_{max} is expected at the top of the detector (PMT number $<$ 50). After the *Digital* Q_{max}/Q_{tot} cut a reduction of such events is observed for the prompt event (bottom left), suggesting the rejection of some physics events. Assuming the events depositing the maximum charge on the PMTs whose number is < 50 are pure SM events, the physics selection efficiency is estimated to be 61.7 ± 12.1 %.

Fig. 5.28 shows on-time selection with (yellow) and without (withe) *Digital* Q_{max}/Q_{tot} cut. SM events are expected below the detector chimney, so the PMT with Q_{max} is expected at the top of the detector (PMT number $<$ 50). After the *Digital* Q_{max}/Q_{tot} cut a reduction of such events is observed in Fig. 5.28 (bottom left), suggesting the rejection of some physics events. Assuming the events depositing the maximum charge on the PMTs whose number is < 50 are pure SM events, the physics selection efficiency is estimated to be 61.7 ± 12.1 %. The SM spectrum of Fig. 5.28 (top left) is then fitted with a flat and a sloped linear models. The SM rate is computed in agreement with Eq. 5.7, correcting for the *Digital* Q_{max}/Q_{tot} cut efficiency. Results are shown in Fig. 5.29 and summarised in Tab. 5.15.

The shapes and the rates obtained by rejecting the HELN events with dedicated cut based on the *Digital* Q_{max}/Q_{tot} are well in agreement with the results of Sec. 5.5.2, obtained subtracting the HELN contribution selected off-time. Such results validate the off-time sample subtraction as valid LN reduction method.

Fit model	const. [1/(3 MeV)]	slope [1/(3 MeV)^2]	χ^2/dof	R_{SM} [cpd]	$\delta(R_{SM})/R_{SM}$ [%]
Flat	35.9 ± 7.7	–	7.9/9	0.57 ± 0.12	21
Slope	39.0 ± 20.1	-0.2 ± 1.1	8.4/8	0.60 ± 0.22	37

Table 5.15: Summary of SM spectral parameters and SM background rate for the flat and the sloped linear model.

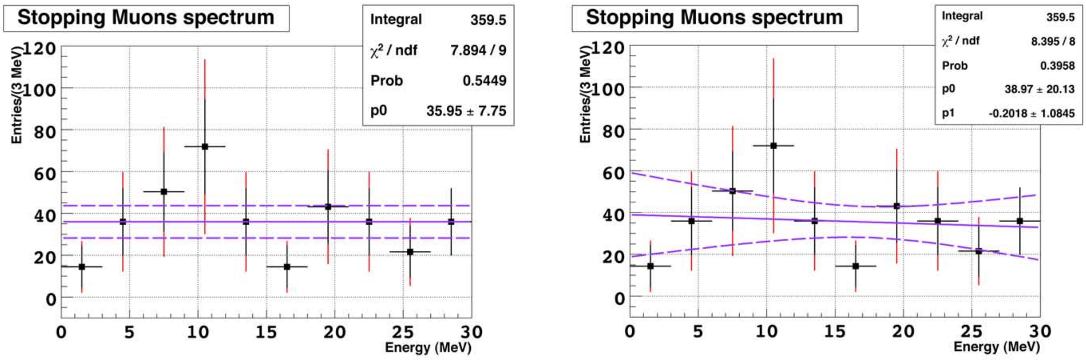

Figure 5.29: SM spectrum fit with flat model (left) and sloped linear model (right) upon *Digital* Q_{max}/Q_{tot} cut. The shapes and the rates are well in agreement with the results of Sec. 5.5.2.

5.5.4 Validating high energy delayed window

The delayed event produced by the SM originates from the Michel electron, created by the muon decay ~ 2.2 μs after the muon has stopped, loosing all its energy by ionization. Since the muon energy losses and the muon decay are two independent processes, the prompt energy spectrum and the Michel electron spectrum are expected to be independent. The SM prompt spectrum obtained selecting the delayed events at high energy, $[20, 60]$ MeV, is then expected to be equivalent to the spectrum one would obtain selecting the delayed events at low energy, in $[6, 12]$ MeV.

In order to validate such assumption, the prompt spectrum obtained selecting the delayed event at high energy is compared to the one obtained from a new SM selection, performed by requiring the delayed candidates at low energy. A contamination from $\bar{\nu}_e$ and FN is expected since the delayed neutrons from these events are selected in the same energy window. In order to reduce such contaminations, the prompt energy is selected > 15 MeV, to minimise the $\bar{\nu}_e$ contamination, and the correlation time between the prompt and the delayed candidate is set to $[2, 4]$ μs , to minimise the FN contamination. The SM selection cuts for both low and high delayed energy are summarised in Tab. 5.16.

Selection	Prompt MeV	Delayed MeV	ΔT μs
High delayed energy	$[0.5, 60]$	$[20, 60]$	$[2, 4]$
Low delayed energy	$[15, 30]$	$[6, 12]$	$[2, 4]$

Table 5.16: High and low delayed energy selection cut.

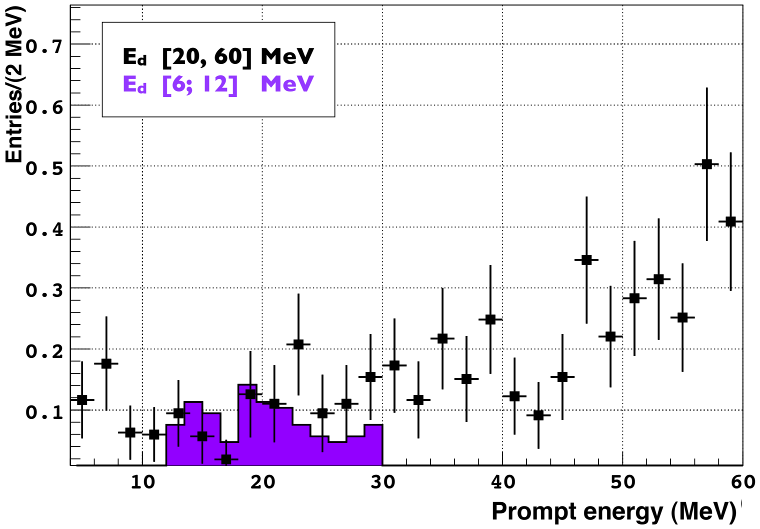

Figure 5.30: Comparison between SM prompt spectrum obtained by selecting the delayed candidate at high energy, $[20, 60]$ MeV, and low energy, $[6, 12]$ MeV. The prompt spectra are in agreement within uncertainty.

The comparison between the prompt energy spectrum obtained from the two SM selections is shown in Fig. 5.30. The spectra are normalised to the same number of events in $[15, 30]$ MeV. Within the statistical uncertainty of the SM sample selected with the low delayed energy (~ 10 %), the two SM prompt spectra are found in agreement. The SM spectrum obtained by selecting the delayed events at high energy is then equivalent to the one obtained from the low energy delayed.

5.6 Estimation of correlated background for θ_{13} measurement

The FN spectral shape obtained implementing a tagging strategy based on the IV has been found in agreement with a linear model. The linear fit to the prompt energy spectrum provides a positive slope of $(1.5 \pm 0.9)/(3\ \text{MeV})^2$, with a $\chi^2/dof = 7.3/8$. The integral of the fitted spectral shape provides a FN rate of (0.33 ± 0.16) cpd with a relative uncertainty of 48 %.

The SM spectral shape is obtained taking advantage from the delayed Michel electron spectrum, selecting the delayed events at high energy in order to reduce contamination from $\bar{\nu}_e$ and FN. The prompt spectrum is found independent from the choice of the energy window used to select the delayed event. The SM spectrum is found in agreement with a linear model. A linear fit to the spectrum provides a positive slope of $(0.4 \pm 1.3)/(3\ \text{MeV})^2$, with a $\chi^2/dof = 6.9/7$. The SM rate is found to be (0.62 ± 0.20) cpd with a relative uncertainty of 37 %.

Since the FN and the SM spectral shapes are well described by a linear model, the two components could be combined in order to reduce the statistical uncertainty on the total correlated background rate. The combined spectra is shown with the fitted linear model and its 1σ uncertainty in Fig. 5.31. The linear fit provides a positive slope of $(1.3 \pm 1.4)/(3\ \text{MeV})^2$ and a $\chi^2/dof = 4.9/8$. The total correlated background rate is found to be (0.93 ± 0.26) cpd with a relative uncertainty of 28 %.

The total correlated background shape have also been obtained by analysing the high energy tail of the prompt spectrum in Sec. 5.2. The high energy analysis does not separate FN and SM components providing an estimation of the total correlated background rate and shape. Such analysis has been repeated without applying the OVV, in order to compare the results with the combined FN and SM analysis. A linear fit to the high energy tail of the prompt spectrum provides a negative slope of $(-0.6 \pm 0.5)/(3\ \text{MeV})^2$ and a $\chi^2/dof = 72/66$. Assuming the shape does not change at low energy, the total correlated background rate of (1.17 ± 0.15) cpd is obtained extrapolating the fitted shape at low energy.

Even if shape and rate obtained from the high energy analysis are compatible with the results obtained by combining FN and SM shapes, the extrapola-

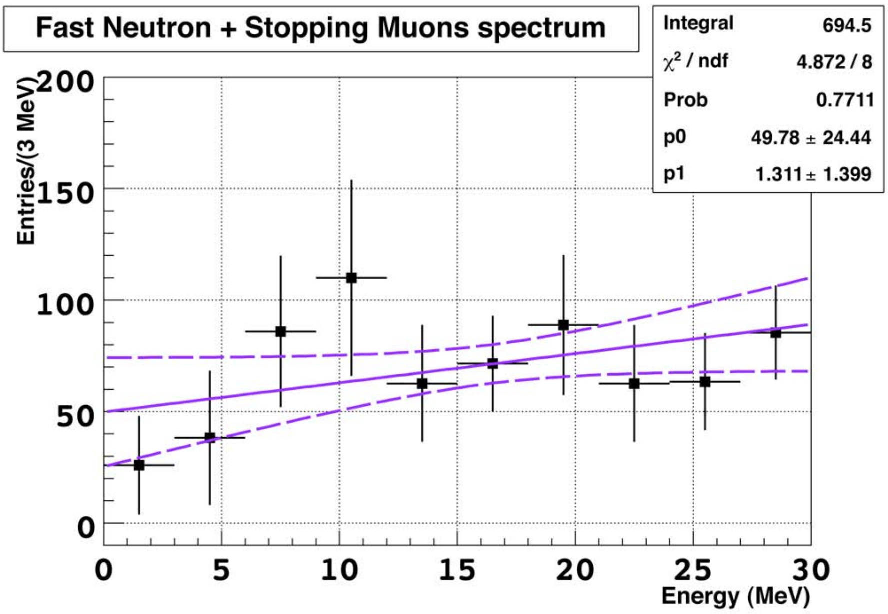

Figure 5.31: Correlated background spectrum obtained by combing FN and SM spectra. The linear fit provides a positive slope of $(1.3 \pm 1.4)/(3 \text{ MeV})^2$ and a $\chi^2/dof = 4.9/8$. The total correlated background rate is found to be (0.93 ± 0.26) cpd.

tion of the high energy spectral shape to the low energy introduce a bias. With the analysis developed in this chapter, the obtained pure sample of correlated background allow to infer directly the FN and the SM spectral shape at low energy, without any assumption.

An independent analysis has been performed taking advantage from the muon tagging capability of the OV in Sec. 5.3. The tagged spectra for both FN and SM are well described by a linear model. The linear fit to the FN spectra provides a positive slope of $(0.17 \pm 0.08)/(3 \text{ MeV})^2$ with $\chi^2/dof = 12.6/8$, while the linear fit to the SM spectra provides a negative slope of $(-0.14 \pm 0.14)/(3 \text{ MeV})^2$ with $\chi^2/dof = 11.3/8$. Background rates of (0.44 ± 0.14) cpd and (0.48 ± 0.11) cpd are found for FN and SM respectively. The OVT results are found in agreement with the independent results obtained from the IVT and the SM analysis developed in this chapter. The background rates obtained so far with three different analysis, performed without the OVV, are summarised in Tab. 5.17.

Analysis	Fast Neutron [cpd (%)]	Stopping Muon [cpd (%)]	Total [cpd (%)]
High energy analysis	–	–	1.17 ± 0.15 (16)
OV Tag	0.44 ± 0.14 (32)	0.48 ± 0.11 (23)	0.92 ± 0.18 (19)
This work	0.33 ± 0.16 (48)	0.60 ± 0.20 (37)	0.93 ± 0.26 (28)

Table 5.17: Summary of the correlated background rate obtained from three different and independent analysis.

5.6.1 Reducing the correlated background with the OV veto

Since the OV is observed to tag the correlated background with high purity, the $\bar{\nu}_e$ selection is performed by rejecting the events found in coincidence with an OV hit, in order to reduce the background contamination.

The background spectral shapes obtained from the OVT analysis are linear, with small slopes compatible with flat shapes, then the OVV is expected to reduce the correlated background of about the same factor the FN and the SM are tagged.

The OV information is available for $\sim 2/3$ of the total detector live time of 240.17 d, then the averaged background reduction over the full data set is expected to be of (25 ± 5) % for FN and (49 ± 8) % for SM. Weighting the FN and SM reductions by the respective rate obtained from the OVT analysis, a total background reduction of ~ 37 % is expected.

The analysis of the high energy tail of the prompt spectrum, provides total correlated background rate of (0.75 ± 0.12) cpd and (1.17 ± 0.15) cpd respectively with and without OVV. An averaged correlated background reduction of (36 ± 7) % is obtained and is consistent with the expected reduction.

The FN and the SM background have been re-evaluated as described in Sec. 5.4 and Sec. 5.5, adding the OVV. The purities of the FN and the SM separation, defined as the fraction of FN (SM) contaminating the sample of SM (FN), change of 5 % and 10 % respectively since the two components are scaled by the OVV with different rejection efficiencies. The analysis efficiencies do not scale by applying the OVV efficiency.

The total correlated background spectral shape upon OVV is shown in Fig. 5.32. The linear fit provides a slope of $(-0.2 \pm 0.9)/(3\ \text{MeV})^2$ with $\chi^2/dof = 8.7/8$. The spectral shape is consistent with the one obtained without OVV, shown in Fig. 5.31, but a small decrease of the slope is observed. Such change suggest the OV tagging efficiency, obtained by comparing the ratio between the tagged and the untagged number of events at high energy, is not constant but slightly decrease at low energy. For this

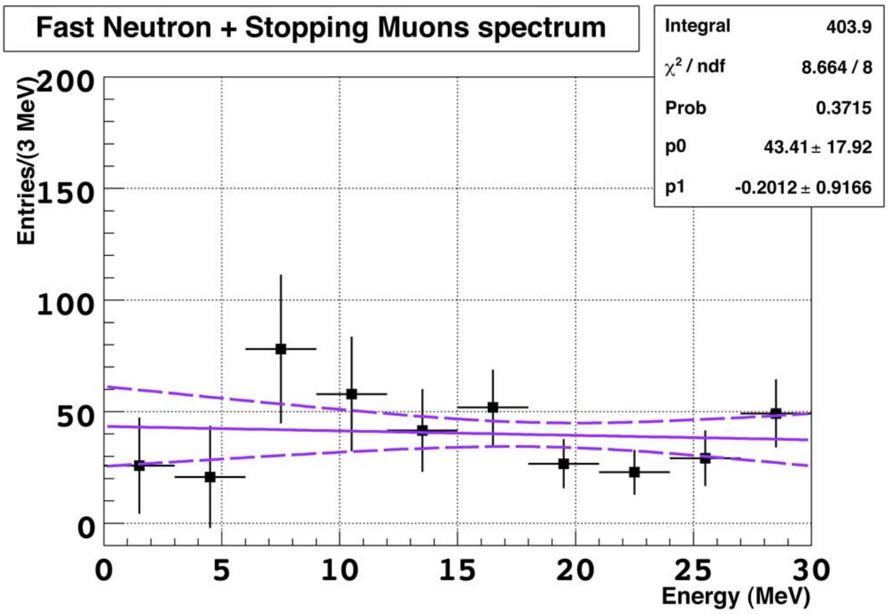

Figure 5.32: Correlated background spectrum obtained by combing FN and SM spectra, upon OVV. The linear fit provides a slope of $(-0.2 \pm 0.9)/(3\ \ \mathrm{MeV})^2$ with $\chi^2/dof = 8.7/8$.

reason the observed background reduction is smaller than expected. The background rates, with and without OVV, are summarised in Tab. 5.18.

Analysis	Without OVV [cpd]	With OVV [cpd]	Reduction [%]	Expected reduction [%]
Fast Neutron	0.33 ± 0.16	0.30 ± 0.14	9 ± 6	25 ± 5
Stopping Muon	0.60 ± 0.22	0.34 ± 0.18	43 ± 28	49 ± 8
Total	0.93 ± 0.26	0.67 ± 0.20	28 ± 11	∼ 37

Table 5.18: Summary of the background rate upon OVV.

5.6.2 Correlated background shape and uncertainty for the final fit

The final correlated background shape obtained upon OVV is shown in Fig. 5.33. The signal selection performed in $[0.7, 30]$ MeV is shown by the white histogram and compared to the tagged correlated background shown by the grey histogram. The solid red line represents the linear model adopted for the correlated background shape, while the dashed red line represents the shape normalisation uncertainty.

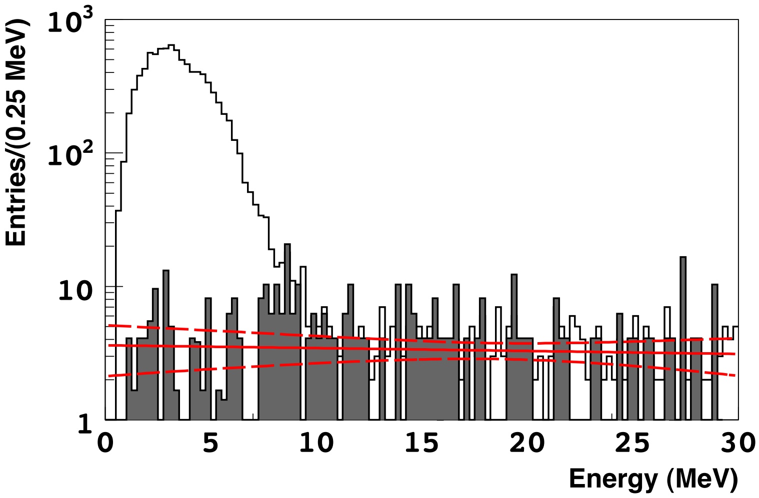

Figure 5.33: The final correlated background shape obtained upon OVV. The signal selection performed in $[0.7, 30]$ MeV is shown by the white histogram and compared to the tagged correlated background shown by the grey histogram. The solid red line represents the linear model adopted for the correlated background shape, while the dashed red line represents the shape normalisation uncertainty.

Since the OVV introduces a small change in the shape obtained without OVV, a spectral shape uncertainty is introduced to account for such variation. The spectral shape uncertainty is shown by the blue solid area in Fig. 5.34 in $[0.7, 12]$ MeV.

Spectral shape and its uncertainty parameters are summarised in Tab. 5.19. The spectral shape parameters have been rescaled to the 0.25 MeV binning used in the final fit. The uncertainties are propagated to the final fit in a mixed approach. The normalisation uncertainty is accounted with a pull parameter added to the χ^2 function of Eq. 4.5, in order to vary the spectrum normalisation as a part of the fit. The shape uncertainty, which do not affect the spectra normalisation, is taken into account by a covariance matrix.

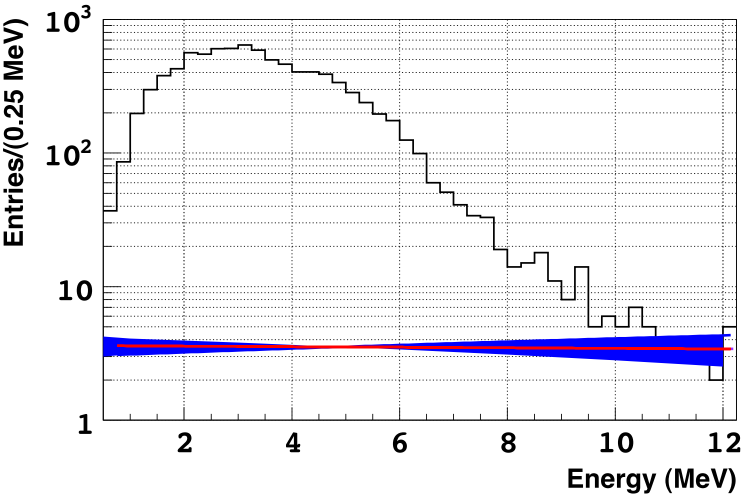

Figure 5.34: The spectral shape (red solid line) and shape uncertainty (blue solid region), added to account for the shape variation introduced by the OVV. The shape uncertainty, which do not affect the spectra normalisation, is propagated to the final fit trough a covariance matrix.

	constant [1/(0.25 MeV)]	slope [1/(0.25 MeV)^2]
Shape	3.62 ± 1.49	-0.016 ± 0.076
Shape Uncertainty	2.99 ± 2.03	0.11 ± 0.16

Table 5.19: Final correlated background shape and shape uncertainty parameters

5.7 Conclusion

In this chapter the correlated background affecting the $\bar{\nu}_e$ search in DC has been discussed. The correlated background is produced by muons interacting in the detector or in its surrounding, whose prompt and delayed come from the same physical process. Such background produces a prompt-like and a delayed-like events which show similar time and spatial correlations as $\bar{\nu}_e$ signal, i.e time correlation within 100 μs and spatial correlation within few tens of cm.

Most of the correlated background is reduced < 0.2 % by applying a 1000 μs veto time upon an identified muon interacting in the ID or in the IV. The remaining background is estimated by dedicated analysis.

Two contributions to the remaining correlated background have been identified, FN and SM. Any indications of further contributions have not been found within the sensibility provided by the current data, but are not excluded a priori.

The FN component have been separated by the SM by requiring the time correlation between the prompt and the delayed events to be > 10 μs. A low energy sample has been selected with an efficiency of 33 ± 5 % by a tag strategy based on the number of PMT hit in the IV. FN are IVT if the ID prompt candidate is found in coincidence with an IV energy deposition presenting PMT multiplicity $\geqslant 2$. Two sources of background on the tagged FN sample has been identified and reduced to ~ 14 %, obtaining a ~ 86 % pure IVT FN sample. The remaining background has been measured in an off-time window and subtracted in order to minimise the distortions on the energy spectrum.

The SM component is obtained by requiring the time correlation between the prompt and delayed events to be < 10 μs. The spectral shape at low energy is obtained taking advantage from the delayed Michel electron spectrum, selecting the delayed events at high energy in order to reduce contamination from $\bar{\nu}_e$ and FN. The prompt spectrum is found independent from the choice of the energy window used to select the delayed event.

The total correlated background rate has been obtained by combining the FN and the SM components, in order to reduce the statistical uncertainty. The total correlated background rate is found to be (0.93 ± 0.26) cpd.

Consistent results have been obtained from an independent analysis based on the OVT and also by analysing the high energy tail of the prompt spectrum.

Since the OV is observed to tag the correlated background with high purity, the $\bar{\nu}_e$ selection is performed by rejecting the events found in coincidence with an OV hit, in order to reduce the background contamination.

A reduction of the correlated background of ~ 30 % is observed and a total rate of (0.67 ± 0.20) cpd is obtained.

Chapter 6

Conclusions

The main focus of this thesis has been the study of the correlated background contaminating the $\bar{\nu}_e$ selection in the Double Chooz (DC) reactor experiment. The correlated background is produced by muons interacting in the detector or in its surrounding, whose prompt and delayed show similar time and spatial correlations as $\bar{\nu}_e$ signal.
A total of 323 days of data taken with the DC far detector, from 13th April 2011 to 30th March 2012, has been used to perform the analysis developed in this work. The same data set has been adopted for the measurement of θ_{13} in [20].

The results obtained in this work are summarised in the follow.

- The correlated background has been reduced < 0.2 % by tagging muons crossing the detector with efficiency > 99.999 % and applying a veto time of 1000 μs upon a tagged muon.
- The remaining correlated background, arising from muons which either missed the detector or deposit an energy low enough to escape the muon tagging, has been identified to be due to fast neutrons (FN) and stopping muons (SM).
- FN and SM have been evaluated separately with dedicated analysis developed in this thesis.
- The FN component have been separated by the SM by requiring the time correlation between the prompt and the delayed events to be > 10 μs. A low energy sample has been selected with an efficiency of 33 ± 5 % by a tag strategy based on the number of PMT hit in the IV.
- The FN spectral shape has been found in agreement with a linear model with a positive slope. The integral of the fitted spectral shape provides a rate of (0.33 ± 0.16) cpd with a relative uncertainty of 48 %.

- The SM component is obtained by requiring the time correlation between the prompt and delayed events to be $< 10\ \mu$s. The spectral shape at low energy is obtained taking advantage from the delayed Michel electron spectrum, selecting the delayed events at high energy.
- The SM spectral shape has been found in agreement with a linear model with a positive slope. The integral of the fitted spectral shape provides a rate of (0.62 ± 0.20) cpd with a relative uncertainty of 37 %.
- Since the FN and the SM spectral shapes are well represented by linear models, the two components are combined in order to reduce the statistical uncertainty on the total correlated background rate. The fit to the combined spectra provides a total correlated background of (0.93 ± 0.26) cpd with a relative uncertainty of 28 %.
- The total correlated background shape have also been obtained by analysing the high energy tail of the prompt spectrum. A linear fit to the high energy tail of the spectrum provides a negative slope. Assuming the shape does not change at low energy, the total correlated background rate of (1.17 ± 0.15) cpd is obtained extrapolating the fitted shape at low energy. A bias of ~ 25 % is found with respect to the results obtained from the IVT and the SM analysis, however, rate and shape are compatible within uncertainties.
- An independent analysis has been performed taking advantage from the muon tagging capability of the OV. The tagged spectra for FN and SM are well described by linear models and provide background rates of (0.44 ± 0.14) cpd and (0.48 ± 0.11) cpd for FN and SM respectively. The OVT results are found in agreement with the independent results obtained from the IVT and the SM analysis.
- Since the OV is observed to tag the correlated background with high purity, the $\bar{\nu}_e$ selection is performed by rejecting the events found in coincidence with an OV hit, in order to reduce the background contamination. A reduction of the correlated background of ~ 30 % is observed and a total rate of (0.67 ± 0.20) cpd is obtained.

Some improvements of this analysis could be foreseen for the future:

- The IV tag could be improved by studying the IV vertex distribution. The FNs are expected to present spatial correlation between the ID and the IV events position, while such spatial correlation is not expected for the accidental background, as discussed in Sec. 5.4.2. A purer FN sample is expected by adding to the current IVT a further condition on the IV vertex. Currently, the IV vertex reconstruction algorithm is under development.

- The SM analysis could be improved by reducing the energy window used to select the delayed events. The contamination of high energy light noise found in the SM selection is, as shown in Fig. 5.21, dominant at high energy, > 40 MeV. A smaller energy window, i.e $[20, 40]$ MeV, is expected to provide a purer SM sample.

- More statistics in the future would help to clarify if the linear model adopted for the correlated background shape is the correct one or if a different model is required.

- In a similar way the OV veto reduce the correlated background, the IV tagging could be employed to further reduce FN contamination. A reduction of ~ 33 %, corresponding to the measured tagging efficiency, is expected.

- The upper OV layer has been installed recently. It is expected to tag muons with small zenith angles, capable to enter in the detector through the chimney. In the future, the OV veto is then expected to further reduce the SM background.

- The OV capabilities to tag the correlated background measured at high energy, > 12 MeV, is observed to decrease at low energy, < 12 MeV, causing a background reduction smaller then expected. The upper OV layer could now be used to study the tagging efficiency as a function of the energy < 12 MeV and the observed background reduction could be validated.

- Once the data taking with both detectors will start, more detailed studies will be possible. Since the near detector will be installed at a smaller depth with respect to the far detector, an higher correlated background rate is expected. The measurements performed with the near detector could then be extrapolated to the far detector in order to increase the accuracy of the correlated background estimation.

For the first time, this analysis allow to directly measure the correlated background in the low energy region, where $\bar{\nu}_e$ are observed. Past and present experiments [36, 33, 31], measure the correlated background by extrapolating the high energy tail of the prompt spectrum at low energy. A bias could be introduced by extrapolating the high energy tail, since the shape of the low energy part of the correlated background spectrum is expected to be dominated by scintillator quenching and acceptance effects, which introduce a slope in the correlated background shape. Such a bias is expected to be detector dependent. In this thesis, such method has been found compatible with the results obtained by selecting the background at low energy, but a bias of ~ 25 % has been found.

This analysis has been adopted by the DC collaboration and the results obtained in this thesis have been used to perform the rate and shape analysis to measure θ_{13} in [20]. The best fit value for the neutrino mixing parameter $\sin^2(2\theta_{13})$ has been found to be 0.109 ± 0.030(stat.)± 0.025(syst.). The precision and accuracy of the measurement relies on precise knowledge of the rates and spectral shapes of the backgrounds contaminating the $\bar{\nu}_e$ selection over the neutrino oscillation expected region.

Chapter 7

Contributions to Double Chooz

Over the last three years, many contributions have been provided to the Double Chooz experiment. This chapter meant to highlight and describe the results and the contributions achieved during the development the present thesis.

First year:

- Installation of the detector read out system, described in Sec. 3.2. The installation and the following testing of the read out system lasted about 4 month, from March to June 2010, leading to an indepth understanding of the detector and various subsystems.

- Raw level analysis of the first detector data, acquired with empty detector after the read out system installation. The analysis involved studies of the FADC baseline and single PE charge deposition. Such studies allow a preliminary tuning of the parameters (i.e integration time window, charge threshold, etc.) necessary for the pulse reconstruction, described in Sec. 3.8.1.

- The analysis performed on the first detector data has been found useful in highlight any misbehaviour of the detector and become later part of the monitoring system, described in Sec. 3.3.4.

- The critical online system devoted to the onsite data file handling and transfer, described in Sec. 3.3.3, has been designed as a part of this thesis. The system maintenance and monitoring has been an important responsibility for the rest of the thesis.

Second year:

- Detector commissioning, fine tuning of data acquisition and trigger system. The detector commissioning lasted about 3 month from January to March 2011, leading to an indepth understanding of the detector response, which has proved vitally important to understand data and perform analysis.

- Preliminary validation of vertex reconstruction algorithm described in Sec. 3.8.2. Further and more accurate studies were performed later by using calibration sources deployed at known position in the detector. The spatial information allowed to study and validate the scintillator time response, obtained from the PMT pulse start time, corrected by the time of flight of the light between the interaction vertex and the PMT itself.

- The vertex reconstruction algorithm has been used to characterise the instrumental light noise affecting Double Chooz data. The vertex distribution show clear structure close to the PMT, validating the hypothesis that such noise where produced by the PMT basis. Such studies were useful to define the strategy adopted to reject such noise, as described in Sec. 4.1.2.

- Preliminary $\bar{\nu}_e$ and accidental background studies, based on the experience provided by CHOOZ [36]. Such preliminary studies defined the signal selection strategy adopted by Double Chooz in [19, 20]

- Optimisation of the muon tagging cuts and reduction of correlated background upon identified muon. This has been one of the main topic of this work and is described in detail in Sec. 3.8.3 and Sec. 4.1.3

- Study of the detector energy containment efficiency, in order to evaluate the systematic uncertainty induced by the definition of the delayed energy cuts. Such study has been performed by analysing ^{252}Cf calibration data as a function of the source position in the detector z-axis and guide tube. The results has been adopted in [19], the same method has been used for [20] and described in Sec. 4.4.2.

Third year:

- Comparison between calibration data and two different MC code, a standard Geant4 code and a custom code developed by Double Chooz collaborators in order to properly account for the low energy neutron physics. Standard Geant4 MC code, in fact, assumes neutron capture on free-H, when it is known that the H is in a molecular bound state. The effect is a shorter live time than the observed ones. The results from this study and from [64] found the data in good agreement with the custom MC code. This custom MC code allow to reduce the systematic uncertainty related to the neutron detection by ~ 6 % in [20].

- Fast neutrons and stopping muon analysis for the measurement of the correlated background affecting the Double Chooz $\bar{\nu}_e$ searches, described in Ch. 5.

List of Figures

List of Tables

Bibliography

[1]

[2]

[3] *CAEN*. `http://www.caen.it/`.

[4] *Geant4*. `http://geant4.cern.ch/`.

[5] *Hamamatsu Photonics*. `http://www.hamamatsu.com/`.

[6] *iRODS*. `https://www.irods.org/`.

[7] *ROOT*. `http://root.cern.ch/`.

[8] Light yield and energy transfer in a new gd-loaded liquid scintillator. *Chemical Physics Letters*, 516:257 – 262, 2011.

[9] *"Proceedings of the XXXV International Conference on Neutrino Physics and Astrophysics"*, 2012. to be published.

[10] Precision electroweak measurements on the Z resonance. *Phys.Rept.*, 427:257–454, 2006.

[11] G. Aad et al. Observation of a new particle in the search for the Standard Model Higgs boson with the ATLAS detector at the LHC. 2012.

[12] K.N. Abazajian, , et al. Light Sterile Neutrinos: A White Paper. 2012.

[13] Abdurashitov et al. Measurement of the solar neutrino capture rate with gallium metal. *Phys. Rev. C*, 60(5):055801, November 1999.

[14] J.N. Abdurashitov et al. Measurement of the response of a Ga solar neutrino experiment to neutrinos from an Ar-37 source. *Phys.Rev.*, C73:045805, 2006.

[15] K. Abe et al. Indication of electron neutrino appearance from an accelerator-produced off-axis muon neutrino beam. *Phys. Rev. Lett.*, 107:041801, Jul 2011.

[16] S. Abe et al. Precision Measurement of Neutrino Oscillation Parameters with KamLAND. *Phys.Rev.Lett.*, 100:221803, 2008.

[17] S. Abe et al. Production of radioactive isotopes through cosmic muon spallation in kamland. *Phys. Rev. C*, 81:025807, Feb 2010.

[18] Y. Abe et al. Id calibration constants by idli. Double Chooz private document DocDB 3767-v1, March 2012.

[19] Y. Abe et al. Indication for the disappearance of reactor electron antineutrinos in the Double Chooz experiment. *Phys.Rev.Lett.*, 108:131801, 2012.

[20] Y. Abe et al. Reactor electron antineutrino disappearance in the Double Chooz experiment. 2012.

[21] C. Aberle, C. Buck, B. Gramlich, F. X. Hartmann, M. Lindner, S. Schönert, U. Schwan, S. Wagner, and H. Watanabe. Large scale gd-beta-diketonate based organic liquid scintillator production for antineutrino detection. *Journal of Instrumentation*, 7:6008, June 2012.

[22] I. Abt et al. A New Ge-76 double beta decay experiment at LNGS: Letter of intent. 2004.

[23] P. Adamson et al. Improved search for muon-neutrino to electron-neutrino oscillations in MINOS. *Phys.Rev.Lett.*, 107:181802, 2011.

[24] P. Adamson et al. Measurement of the neutrino mass splitting and flavor mixing by MINOS. *Phys.Rev.Lett.*, 106:181801, 2011.

[25] P. Adamson et al. Measurement of the neutrino mass splitting and flavor mixing by minos. *Phys. Rev. Lett.*, 106:181801, May 2011.

[26] P. Adamson et al. Search for the disappearance of muon antineutrinos in the NuMI neutrino beam. *Phys.Rev.*, D84:071103, 2011.

[27] A. Aguilar-Arevalo et al. Evidence for neutrino oscillations from the observation of anti-neutrino(electron) appearance in a anti-neutrino(muon) beam. *Phys.Rev.*, D64:112007, 2001.

[28] A.A. Aguilar-Arevalo et al. Unexplained Excess of Electron-Like Events From a 1-GeV Neutrino Beam. *Phys.Rev.Lett.*, 102:101802, 2009.

[29] A.A. Aguilar-Arevalo et al. Event Excess in the MiniBooNE Search for $\bar{\nu}_\mu \rightarrow \bar{\nu}_e$ Oscillations. *Phys.Rev.Lett.*, 105:181801, 2010.

[30] B. Aharmim et al. Measurement of the nu(e) and total B-8 solar neutrino fluxes with the Sudbury neutrino observatory phase I data set. *Phys.Rev.*, C75:045502, 2007.

[31] J.K. Ahn et al. Observation of Reactor Electron Antineutrino Disappearance in the RENO Experiment. *Phys.Rev.Lett.*, 108:191802, 2012.

[32] M.H. Ahn et al. Measurement of Neutrino Oscillation by the K2K Experiment. *Phys.Rev.*, D74:072003, 2006.

[33] F.P. An et al. Observation of electron-antineutrino disappearance at Daya Bay. *Phys.Rev.Lett.*, 108:171803, 2012.

[34] EU++ analysis cluster. Eu++ results for second comparison stage. Double Chooz private document DocDB 3199, October 2011.

[35] Japan analysis cluster. A proposal to make the mq/tq (w/o flag) cut as a standard prescription for the light noise rejection at early analysis stage. Double Chooz private document DocDB 2835, July 2011.

[36] M. Apollonio et al. Search for neutrino oscillations on a long baseline at the CHOOZ nuclear power station. *Eur.Phys.J.*, C27:331–374, 2003.

[37] F. Ardellier et al. Double Chooz: A Search for the neutrino mixing angle theta(13). 2006.

[38] C. Arnaboldi et al. Results from a search for the 0 neutrino beta beta-decay of Te-130. *Phys.Rev.*, C78:035502, 2008.

[39] John N. Bahcall, Aldo M. Serenelli, and Sarbani Basu. New solar opacities, abundances, helioseismology, and neutrino fluxes. *Astrophys.J.*, 621:L85–L88, 2005.

[40] P. Barrillon et al. MAROC: Multi-Anode ReadOut Chip for MaPMTs. In *Nuclear Science Symposium Conference Record, 2006. IEEE*, volume 2, pages 809–814. IEEE, 2006. LAL 06-273.

[41] J. Beringer et al. Review of Particle Physics (RPP). *Phys.Rev.*, D86:010001, 2012.

[42] A. Cabreara et al. Dc2ndpub energy scale final. Double Chooz private document DocDB 3960-v1, May 2012.

[43] A. Cabrera. Correlated background analysis for dc1stpub. Double Chooz private document DocDB 3471-v6, December 2011.

[44] A. Cabrera. Digital ln killer. Double Chooz private document DocDB 3676-v1, February 2012.

[45] E. Conover. Vetoing with ov in ibd selection. Double Chooz private document DocDB 3832-v2, April 2012.

[46] K. Crum. Fast neutron and stopping muon update. Double Chooz private document DocDB 3877-v1, April 2012.

[47] A Cucoanes. A toy model for the gamma spectrum generated in n-captures on gd. Double Chooz private document DocDB 3139-v2, October 2011.

[48] G. Danby et al. Observation of high-energy neutrino reactions and the existence of two kinds of neutrinos. *Phys. Rev. Lett.*, 9:36–44, Jul 1962.

[49] Danilov et al. Detection of very small neutrino masses in double beta decay using laser tagging. *Phys.Lett.*, B480:12–18, 2000.

[50] Raymond Davis, Don S. Harmer, and Kenneth C. Hoffman. Search for neutrinos from the sun. *Phys. Rev. Lett.*, 20:1205–1209, May 1968.

[51] Y. Declais et al. Study of reactor antineutrino interaction with proton at bugey nuclear power plant. *Physics Letters, Section B: Nuclear, Elementary Particle and High-Energy Physics*, 338(2-3):383–389, 1994.

[52] D. Dietrich, D. Greiner, J. Jochum, T. Lachenmaier, L. F. F. Stokes, and M. Röhling. Monte Carlo aided design of the inner muon veto detectors for the Double Chooz experiment. *ArXiv e-prints*, July 2012.

[53] B. C. Diven, H. C. Martin, R. F. Taschek, and J. Terrell. Multiplicities of fission neutrons. *Phys. Rev.*, 101:1012–1015, Feb 1956.

[54] Z Djurcic et al. Detection systematics for 2nd oscillation analysis. Double Chooz private document DocDB 4023-v1, May 2012.

[55] DONUT Collaboration. Observation of tau neutrino interactions. *Physics Letters B*, 504:218–224, April 2001.

[56] M. Elnimr. Dcgenspecv2. Double Chooz private document DocDB 4031-v1, May 2012.

[57] Gary J. Feldman and Robert D. Cousins. A Unified approach to the classical statistical analysis of small signals. *Phys.Rev.*, D57:3873–3889, 1998.

[58] E. Fermi. *Nuovo Cimento*, 11(1), 1934.

[59] A. Franke. Multiple integration periods & sorting rules. Double Chooz private document DocDB 3784-v2, March 2012.

[60] W. Hampel et al. Final results of the Cr-51 neutrino source experiments in GALLEX. *Phys.Lett.*, B420:114–126, 1998.

[61] W. Hampel et al. GALLEX solar neutrino observations: Results for GALLEX IV. *Phys.Lett.*, B447:127–133, 1999.

[62] J Haser. Spill in/out systematics for dc2ndpub. Double Chooz private document DocDB 3943-v3, May 2012.

[63] J. Hosaka et al. Solar neutrino measurements in super-Kamiokande-I. *Phys.Rev.*, D73:112001, 2006.

[64] A. Hourlier et al. Neutron thermalization in the neutrino target. Double Chooz private document DocDB 3673-v1, February 2012.

[65] Patrick Huber. Determination of antineutrino spectra from nuclear reactors. *Phys. Rev. C*, 84:024617, Aug 2011.

[66] Stancu I. et al. The performance of recobama in light of the first calibration data. Double Chooz private document DocDB 2918-v1, August 2011.

[67] C.L. Jones et al. Reactor Simulation for Antineutrino Experiments using DRAGON and MURE. 2011.

[68] L Kalousis et al. Eu++ cluster correlated bg. Double Chooz private document DocDB 3264-v1, October 2011.

[69] V. I. Kopeikin, L. A. Mikaelyan, and V. V. Sinev. Reactor as a source of antineutrinos: Thermal fission energy. *Physics of Atomic Nuclei*, 67:1892–1899, October 2004.

[70] G. Marleau et al. *DRAGON Code*. `http://www.polymtl.ca/nucleaire/DRAGON/en/`.

[71] G. Mention et al. The Reactor Antineutrino Anomaly. *Phys.Rev.*, D83:073006, 2011.

[72] O. Mèplan et al. *MCNP Utility for Reactor Evolution*. `http://lpsc.in2p3.fr/MURE/html/MURE/MURE.html`.

[73] A. Meregaglia et al. Fast neutrons tagging using psd. Double Chooz private document DocDB 3786-v1, March 2012.

[74] Th.A. Mueller. Spill-in/out studies and other interesting stuff about neutron physics. Double Chooz private document DocDB 3031-v1, September 2011.

[75] Th.A. Mueller et al. Improved Predictions of Reactor Antineutrino Spectra. *Phys.Rev.*, C83:054615, 2011.

[76] K Nakamura and Particle Data Group. Review of particle physics. *Journal of Physics G: Nuclear and Particle Physics*, 37(7A):075021, 2010.

[77] P. Novella. Neutrino candidates for dc2ndpub. Double Chooz private document DocDB 4018-v2, May 2012.

[78] P. Novella et al. Dcrecopulse. Double Chooz private document DocDB 649-v2, March 2009.

[79] P. Novella et al. Proposal of recopulse configuration for the first double chooz analysis. Double Chooz private document DocDB 2999-v2, August 2011.

[80] I. Ostrovskiy. *Measuring the neutrino mixing angle* θ_{13} *with the Double Chooz Far detector*. PhD thesis, University of Alabama, 2011.

[81] C. Palomares. Dc2ndpub accidental background. Double Chooz private document DocDB 3954-v13, May 2012.

[82] W. Pauli. Letter to the tübingen conference,. 1930.

[83] M. L. Perl et al. Evidence for anomalous lepton production in $e^+ - e^-$ annihilation. *Phys. Rev. Lett.*, 35:1489–1492, Dec 1975.

[84] A. Pichlmaier et al. Neutron lifetime measurement with the UCN trap-in-trap MAMBO II. *Phys. Lett.*, 693:221, 2010.

[85] F. Piquemal. The SuperNEMO project. *Physics of Atomic Nuclei*, 69:2096–2100, December 2006.

[86] B. Pontecorvo. Mesonium and antimesonium. *Sov. Phys. JETP*, 6:429, 1957.

[87] F. Reines and C. L. Cowan. Detection of the free neutrino. *Phys. Rev.*, 92:830–831, Nov 1953.

[88] B. Reinold et al. Construction of detector response maps. Double Chooz private document DocDB 4066-v1, June 2012.

[89] A Remoto. Muon dead time study. Double Chooz private document DocDB XXXX, October 2011.

[90] A. Remoto et al. Preliminary neutron efficiency note. Double Chooz private document DocDB 3364-v3, November 2011.

[91] Thomas Schwetz, M.A. Tortola, and Jose W.F. Valle. Three-flavour neutrino oscillation update. *New J.Phys.*, 10:113011, 2008.

[92] A. Stueken et al. Trigger efficiency task force report. Double Chooz private document DocDB 3261-v3, October 2011.

[93] A. Stueken et al. Trigger efficiency for 2nd pub. Double Chooz private document DocDB 3966-v2, May 2012.

[94] E. et al. Tournu. Edf technical note. Edf technicalnote, 2011.

[95] P. Vogel and J. F. Beacom. Angular distribution of neutron inverse beta decay, $\overline{\nu}_e + \vec{p}\ e^+ + n$. *Phys. Rev. D*, 60:053003, Jul 1999.

[96] R. Wendell et al. Atmospheric neutrino oscillation analysis with sub-leading effects in Super-Kamiokande I, II, and III. *Phys.Rev.*, D81:092004, 2010.

[97] L. Wolfenstein. Neutrino oscillations in matter. *Phys Rev. D*, 17:2369–2374, May 1978.

[98] M. Wurm. Cut parameters for the li-reduced/free analyses. Double Chooz private document DocDB 3883-v2, May 2012.

[99] M. Wurm. Li-9 rate from id analysis. Double Chooz private document DocDB 3893-v2, May 2012.

[100] M. Wurm. Li spectrum. Double Chooz private document DocDB 3937-v1, May 2012.

[101] Maki Ziro, Nakagawa Masami, and Sakata Shoichi. Remarks on the unified model of elementary particles. *Progress of Theoretical Physics*, 28(5):870–880, 1962.